Development of Vertical-Lateral Bimodal Atomic Force Microscopy Utilizing qPlus Sensors for Analysis of Lubricant/Solid Interfaces

Yuya Yamada

2023

Contents

1 Introduction **1**
1.1 Background . . . 1
1.1.1 Tribology . . . 1
1.1.2 Scanning Probe Microscopy . . . 3
1.2 Purpose . . . 4
1.3 Structure of Thesis . . . 5

2 Principles and Instrumentation of Atomic Force Microscopy **9**
2.1 Development of Atomic Force Microscopy . . . 9
2.1.1 Atomic Force Microscopy (AFM) . . . 9
2.1.2 Dynamic AFM . . . 10
2.2 Force Detection with Dynamic AFM . . . 11
2.2.1 Tip-Sample Interations . . . 11
2.2.2 Force Sensor . . . 14
2.2.3 Basic Principles of Dynamic AFM . . . 18
2.2.4 Force Detection with Frequency Modulation AFM (FM-AFM) . . . 21
2.2.5 Vertical and Lateral Force Detection with Bimodal AFM . . . 22
2.2.6 Noise in Dynamic AFM . . . 25

3 Subnanometer-scale Imaging in Polymer Melt **27**
3.1 Introduction . . . 27
3.2 Experimental . . . 28
3.2.1 Materials . . . 28
3.2.2 Experimental Setup . . . 29
3.2.3 Dynamics of the Sensor Immersed in Polymer Melt . . . 30
3.2.4 Sample Preparation . . . 33
3.3 Subnanometer-scale Investigation of PDMS Melt/Mica Interface . . . 34
3.3.1 Atomic Structure Imaging of Mica Surface in PDMS Melt . . . 34
3.3.2 XZ Imaging on PDMS Melt/Mica Interfaces . . . 34
3.4 Summary . . . 37

4 Lateral Tip Oscillation in Higher Modes of qPlus Sensor with Long Probe 39
4.1 Introduction . . . 39
4.2 Eigenmode Analysis with Finite Element Method (FEM) . . . 41
4.2.1 Eigenfrequencies of the qPlus Sensor with Long Probe . . . 41
4.2.2 Eigenmode Analysis with FEM . . . 43
4.3 Experimental Confirmation of Lateral Tip Oscillation . . . 46
4.3.1 Experimental Setup . . . 46
4.3.2 Sample Preparation . . . 47
4.3.3 Results and Discussion . . . 48
4.4 Bimodal AFM with qPlus Sensor with Long Probe . . . 49
4.4.1 Experimental Setup . . . 50
4.4.2 Sample Preparation . . . 50
4.4.3 Results and Discussion . . . 51
4.5 Summary . . . 52

5 Theoretical Analysis of Eigenmodes of qPlus Sensor with Long Probe 55
5.1 Introduction . . . 55
5.2 Theory . . . 56
5.2.1 Mathematical Modeling . . . 56
5.2.2 Equations of Motion . . . 58
5.3 Analysis of Eigenmodes . . . 62
5.3.1 Probe Length Dependence of Sensor Characteristics . . . 62
5.3.2 Discussion . . . 69
5.4 Comparison between Theory and Experimental Results . . . 70
5.4.1 Experimental . . . 70
5.4.2 Results and Discussion . . . 72
5.5 Summary . . . 77

6 Lateral Force Detection with qPlus Sensor with Long Probe 79
6.1 Introduction . . . 79
6.2 Experimental . . . 80
6.2.1 Materials . . . 80
6.2.2 Experimental Setup . . . 81
6.2.3 Sample Preparation . . . 83
6.3 Friction Anisotropy Detection with Bimodal AFM . . . 84
6.3.1 Sensor Characterization . . . 84
6.3.2 Friction Anisotropy Detection on P(VDF-TrFE) Thin Films . . . 85
6.4 Summary . . . 89

7 Effects of Liquid-Solid Interactions on Polymer Melt near Solid Surfaces 91
7.1 Introduction . . . 91
7.2 Experimental . . . 92

7.2.1 Materials 92
7.2.2 Experimental Setup 93
7.2.3 Sample Preparation 93
7.3 PDMS Melt on Mica and Graphite Investigated by Bimodal AFM . . . 95
7.3.1 Mica and Graphite Surfaces Investigated in PDMS Melt 95
7.3.2 XZ Mapping on Mica and Graphite in PDMS Melt 97
7.4 Discussions 101
7.5 Summary 103

8 Conclusion and Future Prospects **105**
8.1 Conclusions 105
8.2 Future Prospects 106

A Details of Theoretical Analysis of Eigenmodes **108**
A.1 Equations of Motion 108
A.2 The Elements of Matrix $\boldsymbol{M}$ 109

Chapter 1

Introduction

1.1 Background

1.1.1 Tribology

"Tribology", which is derived from the Greek word "$\tau\rho\iota\beta\omega$", meaning "rub", is a research field of friction, wear, and lubrication[1]. Reducing energy and resource consumption by reducing friction and wear is one of the most important issues for sustainable development. Reduction of friction and wear by introducing lubricant between surfaces has been tried since ancient times. The principles of friction and lubrication started to be studied intensively in the age of the Industrial Revolution. The curve plotting the coefficient of friction μ against "lubricant viscosity $\times$ sliding velocity/surface pressure ($\eta \cdot V/F_N$)" is called "Stribeck curve"[2] (Fig. 1.1), which indicates the lubrication condition. Lubrication friction can be divided into three main types: Boundary lubrication, Mixed lubrication, and Hydrodynamic lubrication. In hydrodynamic lubrication conditions, the surfaces are completely separated by lubricants, where the friction coefficient is significantly low. The dynamics in hydrodynamic lubrication conditions can be described by Reynolds equation. In boundary lubrication conditions, the two sliding surfaces are separated by several molecular layers or partially in contact (Fig. 1.2). Since the properties of lubricant at the interfaces, which are different from their bulk properties due to interactions between the lubricant and surface, are dominant in boundary conditions, the friction coefficients are difficult to be predicted. The nanoscale investigation of the boundary lubrication layers is important for the understanding of boundary lubrication.

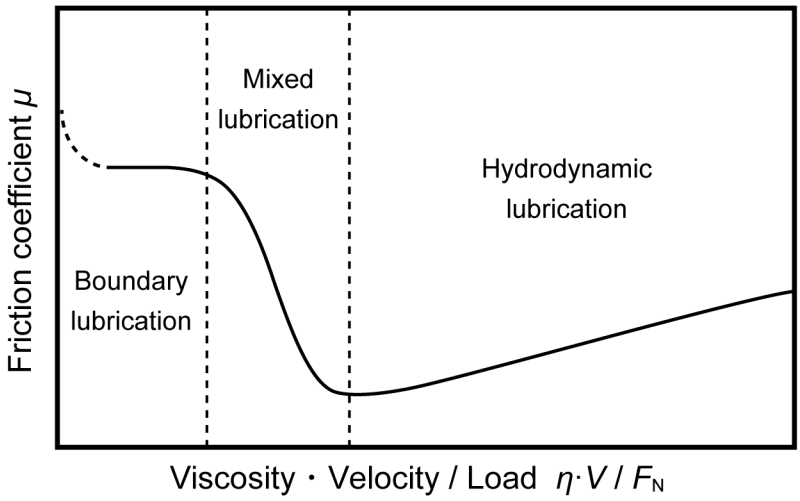

Figure 1.1: A Schematic of Stribeck curve.

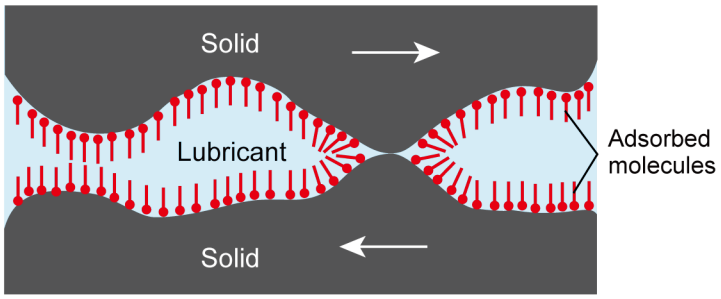

Figure 1.2: A Schematic illustration of boundary lubrication.

In the last 100 years, a lot of scientific tools for nanoscale analysis on solid surfaces have been developed, such as scanning electron microscopy (SEM), X-ray photoelectron spectroscopy (XPS), surface force apparatus (SFA), scanning probe microscopy (SPM), and so on. In particular, SFA and atomic force microscopy (AFM), a kind of SPM, are useful in tribology because the normal and lateral (friction) forces are directly detected by these methods at the nanoscale. In SFA studies of liquids, the liquid is confined by two atomically flat mica surfaces, and the normal and shear forces can be detected simultaneously with the gap distance[3,4]. AFM is capable of imaging the surface topography at the nanoscale[5]. Lateral force microscopy (LFM), which is a relevant technique of AFM, is capable of imaging friction forces at the nanoscale[6]. In addition, molecular dynamic (MD) simulations revealed the molecular dynamics of the liquids confined in nanometer gap[7,8] SFA, AFM, LFM,

and MD simulations have been helpful in understanding tribological phenomena at the atomic and molecular scale. These studies are established as a field of "Nanotribology"[9,10].

1.1.2 Scanning Probe Microscopy

As mentioned above, the invention of the scanning probe microscope (SPM) has brought new insights into tribology.

Scanning tunneling microscopy (STM), invented by Binnig and Rohrer in 1982[11], was the first SPM that detects the tunneling current between the tip and the sample and controls the distance between the tip and the sample to keep the current value constant. Atomic force microscopy (AFM), developed by Binnig, Quate, and Gerber in 1986[5], controls the distance between the tip and sample so that the interaction force between them is kept constant. AFM enables measurements on the surface of insulators at the nanoscale. Lateral force microscopy/friction force microscopy (LFM/FFM) was also developed by Mate *et al.* in 1987[6] to detect lateral forces at the nanoscale.

In the early AFMs, the tip and sample are in contact during imaging (contact mode), which makes analysis at the atomic and molecular level difficult in principle. To overcome this issue, dynamic-mode AFM, in which measurement is performed by oscillating the sensor, was developed. Martin *et al.*[12] developed amplitude-modulated AFM (AM-AFM), in which measurement is performed by detecting changes in the amplitude of the sensor. Albrecht *et al.*[13] developed frequency modulation AFM (FM-AFM), In 1995, Giessibl[14] and Kitamura[15] achieved a true atomic resolution imaging of Si(111) 7x7 surface in UHV using FM-AFM. Dynamic LFM, which detects lateral forces by oscillating the tip horizontally with respect to the surface[16], was also developed. Atomic resolution observation has also been reported by dynamic LFM[17,18].

Bimodal AFM is a method of exciting the sensor at its two different eigenfrequencies[19], which is able to detect mechanical properties of surfaces, such as Young's modulus, simultaneously with topography. In particular, in the case that the tip oscillates vertically and laterally in the independent modes, the vertical and lateral forces can be detected simultaneously separately[20–23]. Dynamic LFM and vertical-lateral bimodal AFM in UHV have provided important knowledge for understanding of friction at the atomic scale.

Since AFM doesn't need UHV environments in principle, it is applied to various environments, including liquid environments. In 2005, Fukuma *et al.*[24] achieved atomic-resolution imaging in water by FM-AFM. Subsequently, FM-AFM was applied to molecular-resolution imaging in various liquids, such as organic liquids[25,26] and ionic liquids[27]. FM-AFM in liquids can visualize not only solid surfaces but also the density distribution of liquid molecules on the surface at the atomic scale[28,29]. Recently, it has been applied to the lubricant/solid interface to visualize the boundary lubricant layer[30–32]. Dynamic LFM has also been applied to analyze the shear response of various liquids near solid surfaces[33–42]. On the other hand, there are few reports of analysis in practical lubricants, and high-resolution imaging has not been achieved. This is because the viscosity of the liquid reduces the Q factor of the sensor, and the force sensitivity of the FM-AFM is seriously suppressed.

The qPlus sensor was developed by Giessibl[43] in 1998 to improve the operating speed of FM-AFM by achieving a higher Q factor than conventional Si cantilevers. Currently, the qPlus sensor is widely used as well as Si cantilevers. By using the qPlus sensor, atomic-resolution observations were achieved in highly viscous ionic liquids[44,45] as well as in UHV[46] and air[47,48]. The qPlus sensor is a good candidate for investigating polymer melt/solid interfaces with high spatial resolution.

The qPlus sensor can also detect lateral forces by attaching the probe parallel to the QTF and mounting it as the tip oscillates along the surface[17]. This method has been used to observe friction in UHV with atomic resolution[17,49] and chemical bonding resolution in combination with the carbon monoxide-modified tip[50]. However, simultaneous detection of vertical and lateral directions by a single qPlus sensor is difficult due to its detection scheme, and it is still being researched[51–56].

1.2 Purpose

The purpose of this study is to develop a bimodal AFM capable of simultaneously detecting vertical and lateral forces with high-spatial resolution in highly viscous liquids, and to apply the developed method to the analysis of the lubricant/solid interface to reveal lubrication mechanisms on the atomic and molecular scale. The objectives of this thesis are as follows.

The first objective is high-resolution imaging in highly viscous environments. In highly viscous liquids, the Q factor of the sensor decreases due to the viscosity of

the liquid, and the force sensitivity of the FM-AFM is seriously suppressed. It has been reported that atomic-resolution imaging is possible in highly viscous liquids by using the qPlus sensor, which consists of a quartz tuning fork and a probe[44,45]. In this thesis, FM-AFM using the qPlus sensor is applied to high-resolution imaging in polymer melts.

The second one is the development of the method of simultaneously detecting vertical and lateral forces by a single qPlus sensor. The qPlus sensor is difficult to detect vertical and lateral forces because of its detection mechanism using the piezoelectric effect. Simultaneous analysis of vertical and lateral forces requires using two modes, one in which the tip oscillates vertically and the other in which it oscillates laterally. It has been reported that the higher flexural mode of the qPlus sensor varies when a long tip is attached[51]. In this study, it is confirmed by simulation and experiment that the tip oscillates laterally in the higher modes of the qPlus sensor with a long probe. A theoretical analysis of the eigenmodes of the qPlus sensor is conducted to optimize the probe length for the detection of vertical and lateral forces. Furthermore, it is experimentally confirmed by friction anisotropy measurement that lateral forces can be detected by the qPlus sensor with a long probe.

The third one is the investigation of the polymer lubricant/solid interface by the developed method. Interactions with solid surfaces affect the physical properties of liquid molecules near the surface. However, there are few reports of molecular-scale analysis of the polymer melt/solid interfaces. In this study, the polymer melt/solid interface is investigated using the developed method, and the density distribution and shear response of the polymer melt near solid surfaces are analyzed.

1.3 Structure of Thesis

This thesis is composed of the following seven chapters. The structure of the thesis is schematically shown in Fig. 1.3.

In chapter 1, the background and the purpose of this study are described. The increasing need for molecular-scale investigation tools in the tribology field is pointed out. The distinctive advantages and challenges of AFM are discussed in terms of its applications to nanotribology.

In chapter 2, the basic principles and the instrumentation of AFM are described. The tip-sample interaction measurement methods used in dynamic-mode AFM are

explained in detail. The instrumentation of vertical and lateral force measurement with bimodal AFM is also described.

In chapter 3, subnanometer-resolution imaging by FM-AFM with a qPlus sensor in polymer lubricants is demonstrated. The atomic structure of the solid surface and the molecular-scale density distribution of polymer melt are successfully visualized.

In chapter 4, the possibility of the application of qPlus sensors to vertical and lateral force detection is demonstrated. The lateral tip oscillation in higher modes of the qPlus sensor with a long probe is experimentally confirmed.

In chapter 5, the probe length dependence of characteristics of qPlus sensors is theoretically analyzed and experimentally examined.

In chapter 6, the vertical and lateral force detection with bimodal AFM utilizing a qPlus sensor with a long probe is experimentally demonstrated on a polymer thin film with friction anisotropy.

In chapter 7, the interfacial structure and viscosity of polymer melt near solid surfaces are experimentally studied in relation to the solid-liquid interactions.

In chapter 8, the conclusions of this study are summarized. Some proposals for future works are also presented.

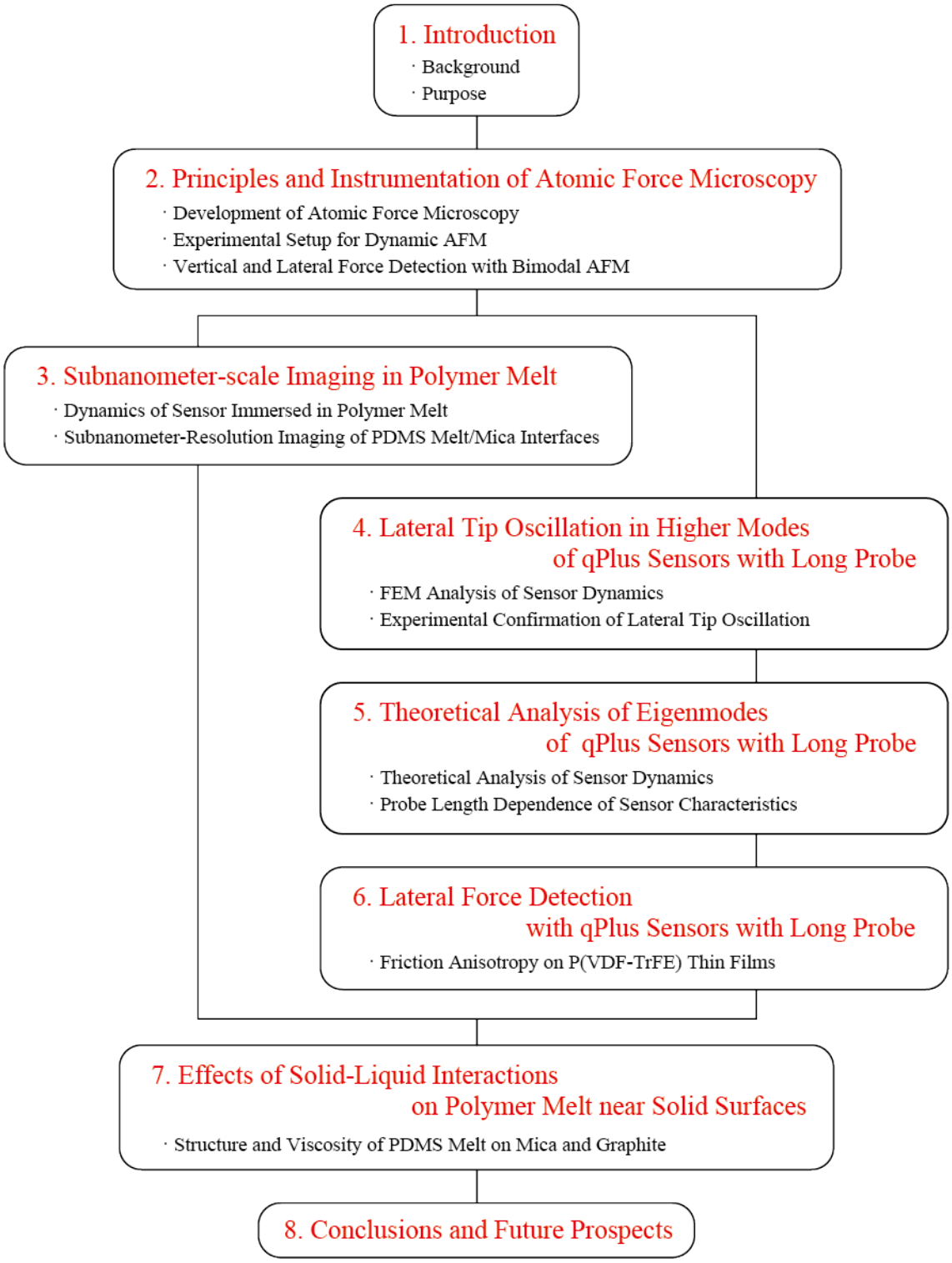

Figure 1.3: Structure of thesis.

Chapter 2

Principles and Instrumentation of Atomic Force Microscopy

In this chapter, features of atomic force microscopy (AFM) and relevant techniques are described. The principles, instrumentation, and noise of dynamic AFM are also described.

2.1 Development of Atomic Force Microscopy

2.1.1 Atomic Force Microscopy (AFM)

Contact-mode AFM

Atomic force microscopy (AFM), which Binnig, Quate, and Gerber developed in 1986[5], is a method to investigate surface morphology by scanning a tip along the surface while keeping the applied force constant. The firstly developed AFM is contact-mode (static-mode) AFM, in which the tip-sample interaction force in vertical direction F_Z is detected as the displacement q of a cantilever beam with spring constant k.

$$q = \frac{F_Z}{k}. \tag{2.1}$$

In contact-mode AFM, atomic-resolution imaging is difficult because frictional forces and uncontrollable "jump-to-contact" cause damage to the sample and tip. Atomic-scale images obtained by contact-mode AFM are interpreted as lattice images.

Lateral Force Microscopy/Friction Force Microscopy (LFM/FFM)

Mate *et al.*[6] reported the atomic-scale friction force detected by the modified AFM, which is called lateral force microscopy (LFM) or friction force microscopy (FFM). In the earlier time, the lateral deflection of the tungsten tip was detected for friction force measurement. Currently, the torsional deflection of silicon cantilevers, detected by a four-segment photodiode[57], is usually used. By detecting the lateral forces F_X between the tip and the sample surface, keeping a constant applied force F_Z, the lateral force image reflects the friction coefficient as $\mu = F_X/F_Z$. Friction force with the period of the lattice constant of solid surfaces is understood as the atomic-scale stick-slip with the large apparent area of contact[6,58].

2.1.2 Dynamic AFM

Dynamic AFM

In dynamic AFM, the force sensor is oscillated at or near its eigenfrequency, and the tip-sample interaction is detected via the changes in its oscillation state. There are two main methods for detecting probe oscillation (Fig. 2.1). One is amplitude modulation AFM (AM-AFM) developed by Martin *et al.*[12] in 1987. In AM-AFM, the cantilever is excited at a constant frequency close to its eigenfrequency. The tip-sample interaction changes the oscillation amplitude, and the tip-sample distance is feedback as keeping the amplitude change constant. The other is frequency modulation AFM (FM-AFM) developed by Albrecht *et al.*[13] in 1991. In FM-AFM, the cantilever is always excited at its eigenfrequency. The tip-sample interaction changes eigenfrequency, and the tip-sample distance is feedback as keeping the frequency shift constant. The details of the principles of these methods are described in the following section.

Dynamic LFM

Dynamic AFM can be applied to lateral force detection by oscillating the tip parallel to the surface[16], which is called dynamic LFM. The force detection is conducted by the same methods as dynamic AFM (AM-mode and FM-mode). Since the lateral force is mainly contributed by the short-range components, the dynamic LFM is sensitive to the short-range interactions. However, it is not suitable for tip-surface distance regulation. Therefore, dynamic LFM is usually performed with scanning

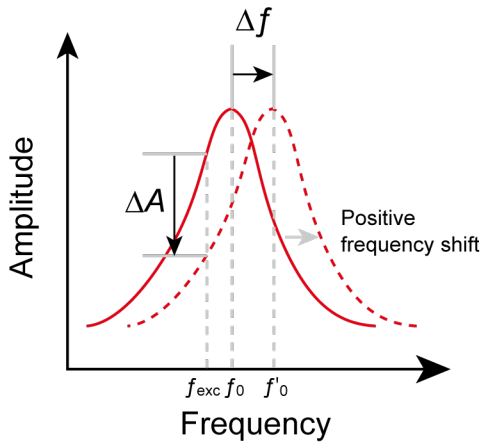

Figure 2.1: A Schematic illustration of the detection methods of dynamic AFM

tunneling microscopy[17,49,59,60] or bimodal AFM[20–23] described below.

Bimodal AFM

Bimodal AFM is a method of exciting the sensor at its two different eigenfrequencies[19], which is able to detect mechanical properties, such as Young's modulus, simultaneously with topography. In particular, in the case that the tip oscillates vertically and laterally in the independent modes, the vertical and lateral forces can be detected simultaneously separately[20–23].

2.2 Force Detection with Dynamic AFM

2.2.1 Tip-Sample Interations

The tip-sample interaction forces originate from chemical bonding force F_{chem}, van der Waals force F_{vdW}, and so on. These interactions can be divided into two categories; one is short-range forces acting between the atom of the tip apex and the sample atom (or molecule), and the other is long-range forces acting on the whole tip. Chemical bonding force F_{chem} is a short-range force, and van der Waals force F_{vdW} is a long-range force.

Chemical Bonding Force

Chemical bonding force F_{chem} is a short-range force acting between the atom of the tip apex and the surface atom (or molecule), which doesn't depend on the shape

of the tip apex. Interatomic (or intermolecular) potentials at distance z are often expressed with the Lennard-Jones potential (Eq. 2.2) and the Morse potential (Eq. 2.3)[61].

$$U_{LJ} = -E_{bond}\left\{2\left(\frac{\sigma}{z}\right)^{6} - \left(\frac{\sigma}{z}\right)^{12}\right\}, \tag{2.2}$$

$$U_{Morse} = -E_{bond}\left\{2e^{-\kappa(z-\sigma)} - e^{-2\kappa(z-\sigma)}\right\}, \tag{2.3}$$

where E_{bond} is bonding energy, σ is equilibrium distance, κ is a decay length. In Eq. 2.2 and Eq. 2.3, the first term on the right side is the attractive component, and the second term is the repulsive component. The repulsive force originates from Pauli repulsion. The chemical bonding force F_{chem} can be expressed as follows, assuming the interatomic potential as the Lennard-Jones potential.

$$F_{chem} = -12E_{bond}\left\{\left(\frac{\sigma}{z}\right)^{7} - \left(\frac{\sigma}{z}\right)^{13}\right\}. \tag{2.4}$$

van der Waals Force

Since van der Waals force is a long-range force, the shape of the tip apex should be taken into account. Interatomic van der Waals potential $U_{vdW,0}$ is expressed in a similar form as the attractive component in Eq. 2.2 as follows,

$$U_{vdW,0} = -\frac{C_H}{z^6}, \tag{2.5}$$

where C_H is a constant of interatomic van der Waals potential. Assuming that the tip apex is a sphere with a radius R_{tip} and the sample is an infinite plane, the van der Waals potential U_{vdW} is obtained by integrating Eq. 2.5.

$$U_{vdW} = -\frac{A_H R_{tip}}{6z}, \tag{2.6}$$

where A_H is the Hamaker constant, which can be derived from the optical properties of the materials of the tip, sample, and intermediate. van der Waals force is obtained by differentiating Eq. 2.6 with respect to distance z,

$$F_{vdW} = -\frac{\partial U_{vdW}}{\partial z} = -\frac{A_H R_{tip}}{6z^2}. \tag{2.7}$$

Solvation Force

Liquid molecules near the solid surface are ordered due to solid surface-liquid molecule interactions, which is called solvation structure (or solvation layers) (Fig. 2.2). Liquid molecules are well ordered nearby the surface and less ordered as more away from the surface. In surface force apparatus (SFA) and AFM experiments, short-range vibrational forces are often detected when two surfaces approach through the solvation layers, which is called solvation forces. The origin of the vibrational force is primarily geometrical, and the vibrating force function is critically dependent on the geometry of the liquid molecules. For example, the solvation force detected in *n*-alkanes oscillates with a period of 0.4-0.5 nm by SFA[62] and ∼0.6 nm by FM-AFM[63], which corresponds to the width of alkyl chains (0.5 nm). In principle, it is impossible to detect the local solvation structure by SFA because the information is averaged in a plane parallel to the solid surface in SFA experiments. In AFM experiments using a sharp tip, on the other hand, it is possible to visualize the local solvation structure. In recent years, it was revealed the density distribution of liquid molecules by comparing the observed solvation structure with molecular dynamics (MD) simulation results[64]. Theoretical calculations using an approximation of the tip as a liquid molecule (Solvent-Tip Approximation[65,66]) have also been proposed to interpret the density distribution of the liquid from the force-distance curves.

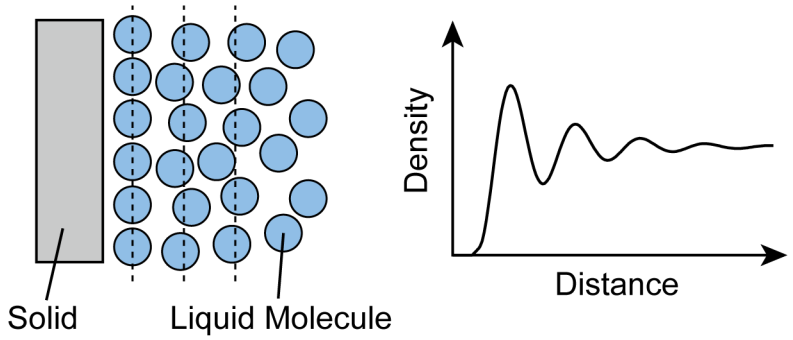

Figure 2.2: A schematic illustration of solvation structure.

Hydrodynamic Force

When the tip moves in liquid environments, the hydrodynamic forces act on the tip, which are dissipative force components originating from the viscosity of liquids. In the case that the tip approaches solid/liquid interfaces and squeezes out the liquid

from the gap with the surface (Fig. 2.3 a), the hydration force, assuming the no boundary slip condition, is given by[67]

$$F_{squeeze} = \frac{6\pi R_{tip}^2 \eta}{z} \cdot \frac{dz}{dt} \tag{2.8}$$

where R_{tip} is the tip radius, η is the viscosity of liquid, z is the tip-surface distance, and dz/dt is the tip approach velocity. In the case that the tip slides solid/liquid interfaces and drags the liquid in the gap with the surface (Fig. 2.3 b), the hydration force, assuming the no boundary slip condition, is given by[68]

$$F_{drag} = \frac{16\pi R_{tip}\eta}{5} \ln\left(\frac{R_{tip}}{z}\right) \cdot \frac{dx}{dt}, \tag{2.9}$$

where dx/dt is the sliding tip velocity. The coefficients of Eq. 2.8 and Eq. 2.9 correspond to the damping coefficients.

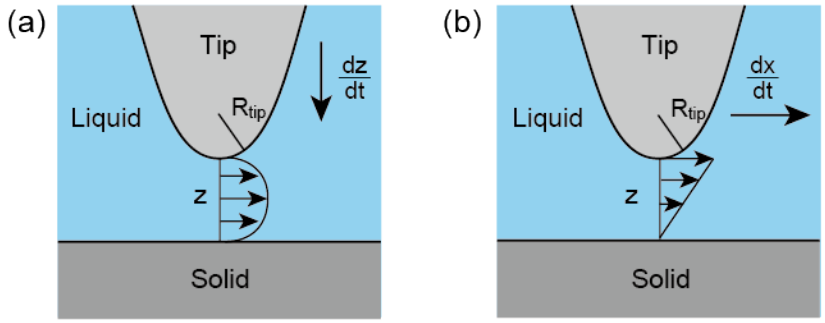

Figure 2.3: A schematic illustration of hydrodynamic forces (a) Squeeze force, R_{tip} is the tip radius, z is the tip-surface distance, and dz/dt is the tip approach velocity. (b) Drag force, dx/dt is the sliding tip velocity.

2.2.2 Force Sensor

qPlus Sensor

The qPlus sensor (Fig. 2.4 a) is a force sensor developed by Giessibl in 1998[43], in which a prong of a quartz tuning fork (QTF) is fixed to a substrate, and a probe is glued to the other prong. It is a self-sensing sensor that uses the piezoelectric effect of the quartz to detect its oscillation electrically.

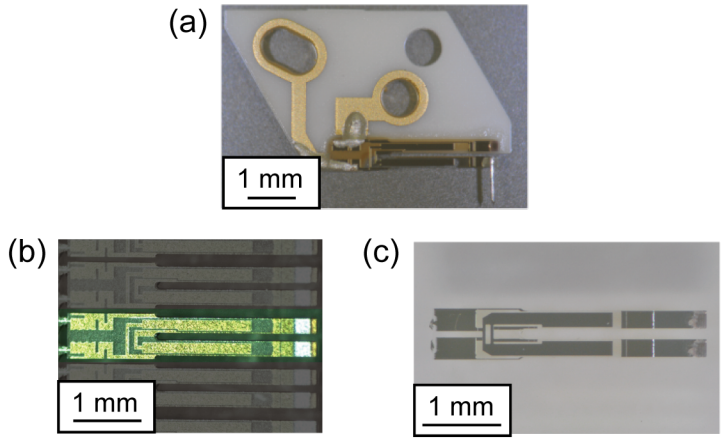

Figure 2.4: Photograph of (a) qPlus sensor, (b) QTF (TFW1165) purchased from STATEK Co., and (c) QTF purchased from SII Crystal Technology Inc.

For a rectangular beam with length L, thickness h, and width b, the spring constant k is given by

$$k = \frac{E_q \cdot b \cdot h^3}{4L^3}, \tag{2.10}$$

where E_q is Young's modulus of quartz. For a harmonic oscillator, the eigenfrequency is given by $f_0 = \sqrt{k/m}$, where m is effective mass. For a constant cross-section and constant mass density ρ, the effective mass is given by $m = 0.243m = 0.243 \cdot \rho \cdot b \cdot w \cdot L$; thus, the fundamental eigenfrequency f_0 is given by

$$f_0 = 0.162 \cdot \frac{h}{L^2} \cdot v_s, \tag{2.11}$$

where v_s is the speed of sound in quartz given by $v_s = \sqrt{E_q/\rho}$.

The QTFs used in this study were purchased from STATEK Co. (TFW1165) and SII Crystal Technology Inc. (Figs. 2.4 b and c). The geometry, spring constant, and eigenfrequency of those QTFs are listed in Table. 2.1.

In this study, an electrochemically etched tungsten probe is attached to the free prong of the QTF. The mass of the tungsten probe causes a non-negligible mass increase, and as a result, the fundamental eigenfrequency f_0 decreases to around 15 kHz. The shape of the eigenmode of qPlus sensor is also affected by attaching the tungsten probe, which will be studied in Chapter 4 and Chapter 5.

Table 2.1: The physical parameters of the QTFs used in this study.

	STATEK Co. (TFW1165)	SII Crystal Technology Inc.
Young's modulus E_q	80 GPa	80 GPa
Mass density ρ_q	2650 kg m^{-3}	2650 kg m^{-3}
Length L	2.357 mm	2.353 mm (i)
Thickness h	0.213 mm	0.223 mm (i)
Width b	0.127 mm	0.111 mm (i)
Electrode length L_e	1.74 mm (i)	1.16 mm (i)
Spring constant k	1884 N m^{-1}	1890 N m^{-1} (ii)
Eigenfrequency f_0	32.768 kHz	32.768 kHz

(i) Measured by optical microscopy (ii) Calculated from the geometry

Measurement of Tip Oscillation

The oscillation of qPlus sensors is electrically detected by using the piezoelectric effect of the quartz. The piezoelectric charge, $Q = Q_0 T(t)$, is generated on the top and bottom electrodes by the deformation of QTF, where Q_0 is the maximum charge in one oscillation cycle, and $T(t)$ is the temporal component. Q_0 is given by[51],

$$\begin{aligned} Q_0 &= -hE_q d_{31} \int_0^L \int_0^b \frac{\partial^2 w(x)}{\partial x^2} dy dx \\ &= -bhE_q d_{31} \frac{\partial w}{\partial x}(L_e), \end{aligned} \tag{2.12}$$

where L_e is the length of the electrode on the QTF prong, d_{31} is the piezoelectric coupling coefficient of quartz, $d_{31} = 2.31$ pC m^{-1}, $w(x)$ is the displacement of the QTF prong at the point of distance x from the root, and $\frac{\partial w}{\partial x}(L_e)$ is the gradient of the QTF prong at the end of the electrode. Assuming the sinusoidal tip oscillation with an amplitude A, $\Delta z = A \cdot T(t) = A \cdot \cos(2\pi i f t)$, sinusoidally varying charge $Q = Q_0 \cos(2\pi i f t)$ is generated, which corresponds to a current $I = \dot{Q} = -2\pi i f Q_0 \sin(2\pi i f t)$.

The piezoelectric current of a qPlus sensor is converted into voltage signals by a current-to-voltage conversion amplifier. In this study, a differential current preamplifier[69] (Fig. 2.5) is used. Both electrodes of the QTF are connected to the two input channels of the operational amplifier (op-amp). The non-inverting input is connected to the ground via a resistor. Therefore, the currents from both sensor electrodes are sensed by the op-amp. Since they are phase-shifted by 180°, and the op-amp simply amplifies the difference voltage between its inputs, the output sig-

nal is twice as large as compared to a single transimpedance system. Uncorrelated noise power adds up linearly, and noise power is proportional to the square of noise voltage amplitude. Therefore, the noise amplitude of uncorrelated noise increases by a factor of $\sqrt{2}$ for the differential setup. Correlated noise is canceled by the common mode rejection of the op-amp in analogy to the three op-amp detection scheme, though this design has just a single op-amp[70]. In addition, a 2 kΩ resistor is put in series directly at the output to avoid high-frequency ringing when a coaxial cable is connected to the output.

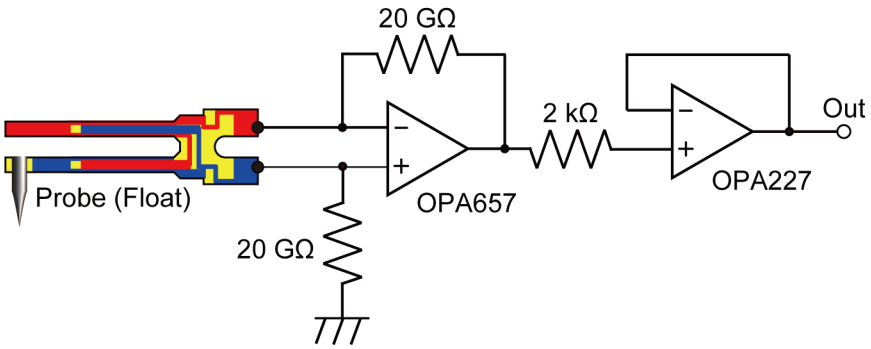

Figure 2.5: A schematic illustration of the circuit of the differential current preamplifier used in this study

Sensor Excitation

The qPlus sensor is mechanically vibrated by a lead zirconate titanate (PZT) actuator (Fuji Ceramics Corp., C-6) equipped on the sensor holder (Fig.2.6). The qPlus sensor is fixed to the sensor holder by two screws.

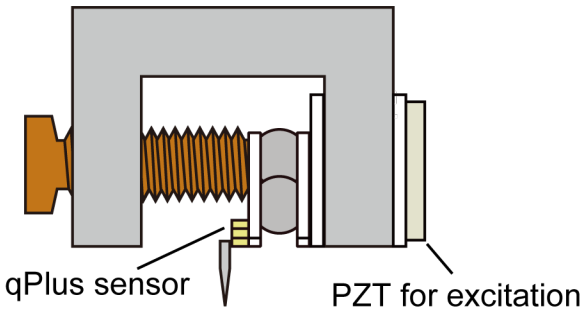

Figure 2.6: A schematic illustration of sensor holder with a PZT actuator

2.2.3 Basic Principles of Dynamic AFM

Sensor Dynamics

In dynamic AFM, the force sensor is excited at or near its eigenfrequency, and the tip-sample interaction in dynamic AFM is detected via changes in its oscillation state. Assuming that the force sensor is a damped harmonic oscillator, the equation of motion of the force sensor excited by an actuator is given by,

$$m\frac{\partial^2 \Delta z}{\partial t^2} + \gamma\frac{\partial \Delta z}{\partial t} + k\Delta z = F_{exc} + F_{ts}, \tag{2.13}$$

where k is the spring constant, m is the effective mass of the sensor, γ is damping coefficient, $\gamma = m\omega_0/Q$, and Q is the quality factor of the sensor. Δz denotes the deflection of the sensor, F_{exc} denotes the excitation force, and F_{ts} denotes the tip-dample interaction force. The sinusoidal excitation force F_{exc} is expressed as

$$F_{exc} = F_d \cos(\omega t) = kA_d \cos(\omega t), \tag{2.14}$$

where F_d is driving force amplitude, A_d is the oscillation amplitude of the PZT actuator. Assuming that the tip motion is sinusoidal, the tip deflection Δz can be described by

$$\Delta z = A\cos(\omega t + \phi), \tag{2.15}$$

where A is the oscillation amplitude, ϕ denotes the phase of the tip oscillation with respect to actuator vibration. From Eq. 2.13-2.15, A and ϕ without the tip-sample interaction ($F_{ts} = 0$) are obtained as

$$A = \frac{QA_d}{\sqrt{Q^2\left(1-\omega^2/\omega_0^2\right)^2 + \omega^2/\omega_0^2}}, \tag{2.16}$$

$$\phi = \arctan\left[\frac{-\omega/\omega_0}{Q\left(1-\omega^2/\omega_0^2\right)}\right]. \tag{2.17}$$

From these equations, the frequency dependence of A and ϕ is plotted as shown in Fig. 2.7.

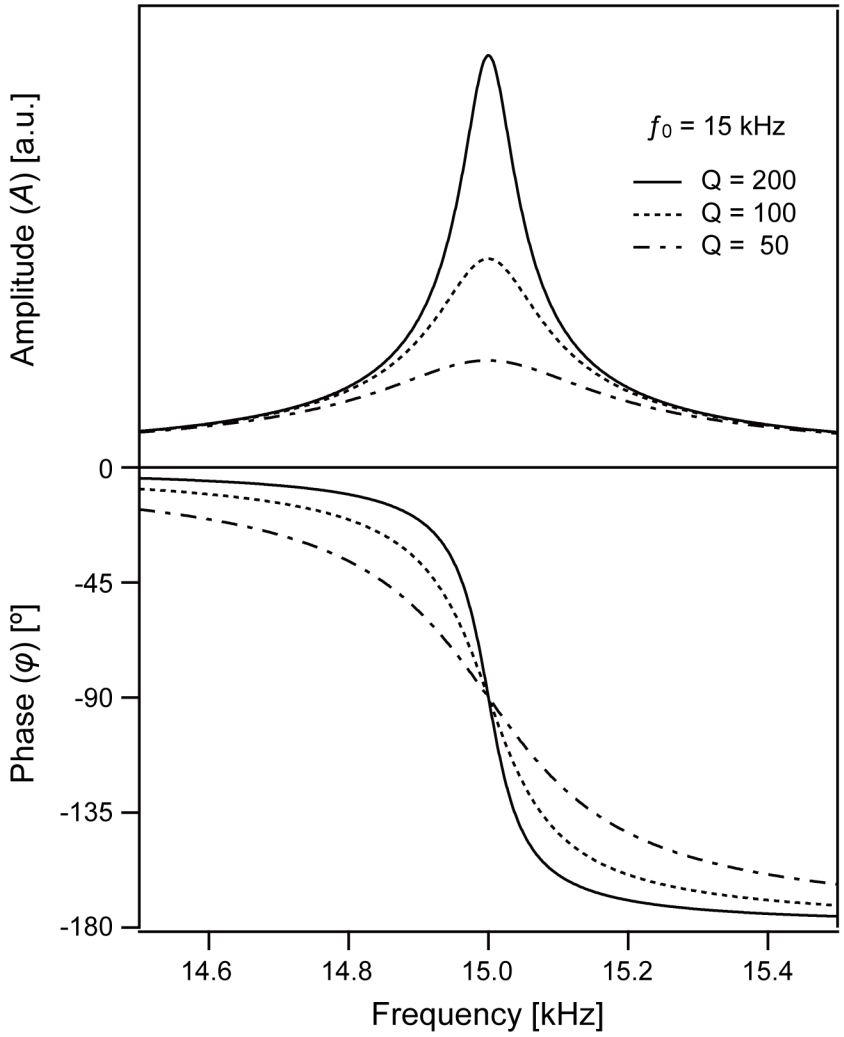

Figure 2.7: Frequency dependence of the amplitude (A) and the phase (ϕ) of the cantilever vibration plotted around the eigenfrequency, which was calculated from Eq. 2.16 and Eq. 2.17. At resonance, A and ϕ become QA_d and -90°, respectively.

Energy Dissipation

The first and the third terms on the left-hand side of Eq. 2.13 are the inertial force and the restoring force of the sensor, respectively. These two force components are conservative and have nothing to do with the energy dissipation process while the other two force components are relevant to the energy dissipation process. The external force $F_{exc} = kA_d \cos(\omega t)$ provides some energy to the oscillating the sensor, and the input power averaged over one period of the tip oscillation (E_{in}) is given by,

$$\begin{aligned} E_{in} &= \frac{1}{T}\int_0^T kA_d \cos(\omega t)\frac{d\Delta z}{dt}dt \\ &= \frac{1}{2}kAA_d\omega \sin(-\phi). \end{aligned} \tag{2.18}$$

The second term in the left-hand side of Eq. 2.13 originates from the internal and external viscosity, which results in the dissipation of the sensor vibration energy. Using $\gamma = m\omega_0/Q$ and $k = m\omega_0^2$, the mean power for this energy loss is obtained as,

$$\begin{aligned} E_0 &= \frac{1}{T}\int_0^T \gamma\left(\frac{d\Delta z}{dt}\right)^2 dt \\ &= \frac{kA^2\omega^2}{2Q\omega_0}. \end{aligned} \tag{2.19}$$

When the tip approaches the sample surface, the vibration energy of the cantilever is partially dissipated by the tip-sample interactions. The mean power of this dissipation (E_{ts}) is given by

$$\begin{aligned} E_{ts} &= E_{in} - E_0 \\ &= \frac{\pi kA^2 f}{Q}\left(\frac{QA_d}{A}\sin(-\phi) - \frac{f}{f_0}\right). \end{aligned} \tag{2.20}$$

Since $\omega \simeq \omega_0$, E_0 and E_{ts} can be approximated as

$$E_0 = \frac{\pi kA^2 f_0}{Q}, \tag{2.21}$$

$$E_{ts} = E_0\left(\frac{QA_d}{A}\sin(-\phi) - 1\right). \tag{2.22}$$

2.2.4 Force Detection with Frequency Modulation AFM (FM-AFM)

Sensor Excitation

In FM-AFM, the sensor is excited by a self-excitation circuit or a phase-lock loop (PLL) circuit. Figure 2.8 shows a typical experimental setup for FM-AFM using a self-excitation circuit. The deflection signal of the sensor is phase-shifted, routed through an automatic gain control (AGC) circuit, and fed back to the PZT actuator. The parameter of the phase shifter is adjusted so as ϕ = -90°. Thus the sensor continuously oscillates at its eigenfrequency during imaging.

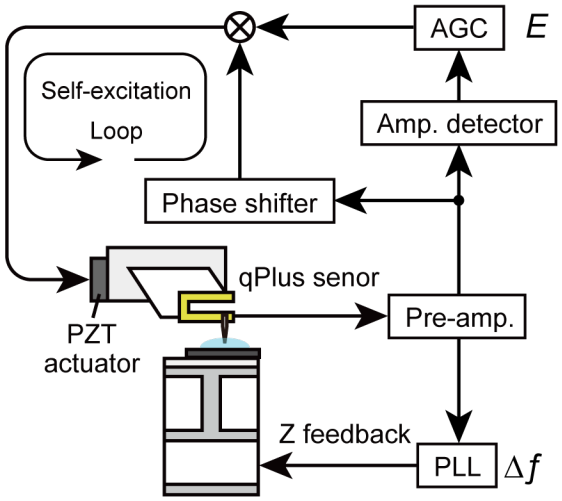

Figure 2.8: The experimental setup of FM-AFM.

Relationship between Force and Frequency Shift

If the oscillation amplitude is sufficiently small, the gradient of the tip-sample interaction force can be approximated to be constant. In this case, the frequency shift Δf induced by the tip-sample interaction is given by

$$\Delta f = -\frac{f_0}{2k}\frac{\partial F_{ts}}{\partial z}. \tag{2.23}$$

Namely, Δf is directly proportional to the force gradient. In contrast, when the oscillation amplitude is relatively large, Δf is obtained by integrating the contribution

of force gradient in the whole distance range of tip oscillation, which is given by[71]

$$\Delta f = -\frac{f_0}{\pi k A}\int_{-1}^{1} F_{ts}(z+A(1+u))\frac{u}{\sqrt{1-u^2}}dz. \tag{2.24}$$

Sader and Javis[72] proposed a formula converting frequency shift into force, which is given by

$$F_{ts} = 2k\int_{z}^{\infty}\left(1+\frac{A^{1/2}}{8\sqrt{\pi(t-z)}}\right)\Omega(t) - \frac{A^{3/2}}{\sqrt{2(t-z)}}\frac{d\Omega(t)}{dt}dt, \tag{2.25}$$

where $\Omega = \Delta f/f_0$. The experimentally obtained Δf-distance curves can be converted into force-distance curves by this equation.

Energy Dissipation Measurement

In FM-AFM, ϕ is kept at -90° using a self-excitation circuit or phase-lock loop. In constant amplitude mode, A_d is feedback-controlled so as to keep A constant, and the changes in A_d represent the variation in energy dissipation. From Eq. 2.22, $\phi = -90°$, and this point, the useful expression for E_{ts} is given by

$$E_{ts} = E_0\left(\frac{A_d}{A_{d,0}} - 1\right) = E_0\left(\frac{V_{exc}}{V_{exc,0}} - 1\right), \tag{2.26}$$

where $A_{d,0}(=A/Q)$ and $V_{exc,0}$ are defined as the values for A_d and V_{exc} without any tip-sample interactions, respectively. In this case, the energy dissipation is proportional to the excitation amplitude V_{exc}.

Assuming that the tip oscillates sinusoidally and γ does not vary with velocity, the damping coefficient can be expressed by

$$\gamma_{ts} = \frac{2E_{ts}}{\omega^2 A^2} \tag{2.27}$$

2.2.5 Vertical and Lateral Force Detection with Bimodal AFM

Basic Principles

Bimodal AFM is a method of exciting the sensor at its two different eigenfrequencies[19]. In the case that the tip oscillates vertically and laterally in the independent modes, the vertical and lateral forces can be detected separately. When the ampli-

tude of the two modes is in the same order of magnitude, the frequency shift of ith mode Δf_i is given by[20,21,73]

$$\Delta f_i = \frac{f_i}{2\pi n_i A_i k_i} \int_0^{2\pi n_i} F\left[tip(X,Z)\right] \cos\theta_i d\theta_i, \tag{2.28}$$

where k_i is the effective spring constant, A_i is the amplitude, n_i is the large number of oscillation cycles of ith mode, and $F_j(X,Z)$ is the conservative part of the force in the direction j acting on the tip at the tip position (X,Z). The tip position is described as $tip(X,Z) = (A_X \cos(2\pi f_X t), Z_0 + A_Z \cos(2\pi f_Z t))$, where A_X and f_X are the amplitude and the eigenfrequency of the mode where the tip oscillates laterally, A_Z and f_Z are the amplitude and the eigenfrequency of the mode where the tip oscillates vertically, and t denotes time. Eq. 2.28 is valid as long as $\Delta f_i / f_i \ll 1$. If two frequencies are incommensurate, only the force component oscillating at f_i makes a finite contribution to the integral in Eq. 2.28. In the limit of $n_i \to \infty$, incommensurability leads Eq. 2.28 to the same form as Eq. 2.24, where the single eigenfrequency is excited. In the small A_i limit, the force gradient F' is obtained as $F' = -2k_i \Delta f_i / f_i$.

The energy dissipation in each mode is obtained in the same way as the single excitation operation. However, it is convoluted with the tip motion made by the two different modes. In this thesis, however, the deconvolution of the averaged energy dissipation is not performed, assuming that the oscillation amplitude is sufficiently small.

Frequency Modulation-Amplitude Modulation (FM-AM) Bimodal AFM

Figure 2.9 shows a typical setup of frequency modulation-amplitude modulation (FM-AM) bimodal AFM. The oscillator and lock-in amplifier are added to the FM-AFM setup. The sensor is excited at f_Z and f_X simultaneously, where the excitation frequency of the lateral oscillation mode is fixed at a constant frequency, and its excitation amplitude is also constant. The tip-sample distance is regulated by using the frequency shift of the vertical oscillation mode Δf_Z. The vertical conservative force gradient and the energy dissipation in the vertical oscillation mode can be obtained in the same way as the single excitation FM-AFM by Eq. 2.24 and Eq. 2.26. During imaging, the amplitude A_X and phase ϕ_X of the lateral oscillation mode can freely change by the lateral tip-sample interactions, which are detected by the lock-

in amplifier. By applying the calculation method for AM mode[74], the conservative lateral force gradient detected by the lateral oscillation mode is given by

$$F'_X = \frac{k_X A_{X,0}}{Q_X A_X} \cos(-\phi_X), \tag{2.29}$$

where k_X is the effective spring constant, $A_{X,0}$ is the amplitude without tip-sample interactions, and Q_X is the quality factor of the lateral tip oscillation mode. The energy dissipation in the lateral oscillation mode is calculated by Eq. 2.22.

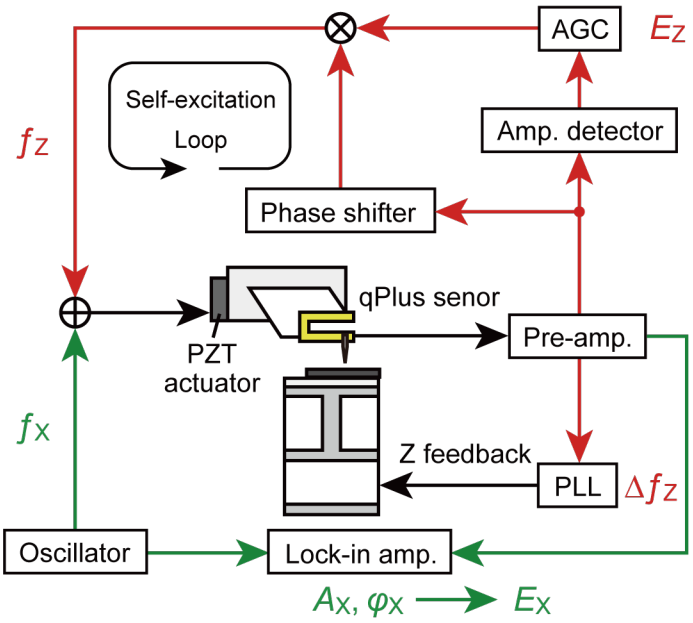

Figure 2.9: The experimental setup of FM-AM bimodal AFM for vertical and lateral force detection.

Frequency Modulation-Frequency Modulation (FM-FM) Bimodal AFM

Figure 2.10 shows a typical setup of frequency modulation-frequency modulation (FM-FM) bimodal AFM. Another set of PLL and AGC is added to the FM-AFM setup. The sensor is excited at f_Z and f_X simultaneously, where the vertical and lateral oscillation modes are continuously excited at their eigenfrequency by the PLL circuit, and their excitation amplitude are feedback by the AGC as keeping A_Z and A_X constant. The detected force gradient and energy dissipation in each mode can be obtained in the same way as the single excitation FM-AFM by Eq. 2.24 and Eq. 2.26.

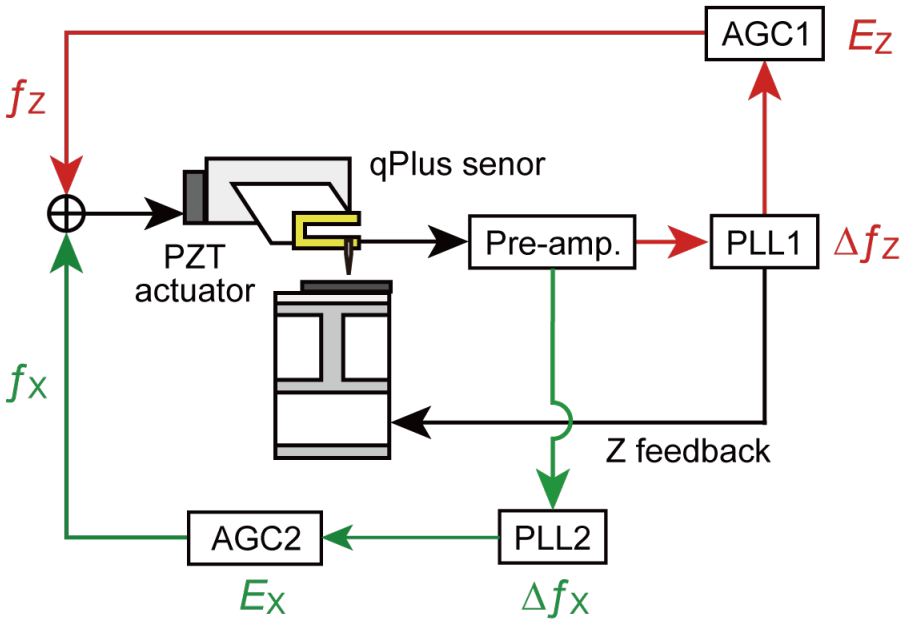

Figure 2.10: The experimental setup of FM-FM bimodal AFM for vertical and lateral force detection.

2.2.6 Noise in Dynamic AFM

The thermal deflection noise density of the sensor n_{th} is given by

$$n_{th} = \sqrt{\frac{2k_BT}{\pi f_0 kQ}\frac{1}{[1-(f/f_0)^2]^2+[f/f_0Q]^2}} \tag{2.30}$$

where k_B is Boltzmann constant, T is the temperature. Since the detection system has non-zero noise, the total noise density of the sensor n_{total} is given by

$$\begin{aligned} n_{total} &= \sqrt{n_{th}^2+n_{ds}^2} \\ &= \sqrt{\frac{2k_BT}{\pi f_0 kQ}\frac{1}{[1-(f/f_0)^2]^2+[f/f_0Q]^2}+n_{ds}^2}, \end{aligned} \tag{2.31}$$

where n_{ds} is equivalent deflection noise density, which originates from the detection system, such as the Johnson noise of the feedback resistor in the current-to-voltage conversion preamplifier.

Experimentally, the thermal noise density is obtained as the spectrum of the voltage signals V_{th}, $V_{th} = S_v n_{total}$, where S_v is the sensitivity which is the ratio of the signal voltage to the deflection of the sensor. By fitting the measured thermal noise density using Eq. 2.31, the S_v and n_{ds} can be obtained.

The noise density in FM-AFM N_{total} is given by[75]

$$N_{total} = \sqrt{\frac{f_0 k_B T}{\pi k Q A^2} + \frac{2 f_m^2 n_{ds}}{A^2} + \frac{f_0^2 n_{ds}^2}{2 Q^2 A^2}}, \tag{2.32}$$

where f_m is the modulation frequency. The first term in the square root in Eq. 2.32 originates from thermal deflection noise, the second term originates from the detection system noise, and the third term originates from the oscillator noise. In UHV environments, the high Q factor ($\sim 10^5$) makes the third term negligibly small. However, in the typical condition of FM-AFM in liquids utilizing qPlus sensors that f_0=15 kHz, Q=100, f_m=10 Hz, A=0.1 nm, the third term cannot be ignored. Therefore, n_{ds} should be suppressed. That would be achieved by high S_v because n_{ds} originates mainly from the electrical noise in the experimental setup in this work.

Chapter 3

Subnanometer-scale Imaging in Polymer Melt

3.1 Introduction

The structural and dynamic analysis of lubricant/solid interfaces has played an important role in the tribology field. Lubrication properties are dominated by the dynamic interaction between solid and liquid at the interface. In general, liquids at liquid/solid interfaces have a density distribution different from that of bulk liquid. This anisotropic density distribution should be induced by the interaction between the surface atoms and the liquid molecules. Therefore, atomic- and molecular-scale investigations of lubricant/solid interfaces are expected to provide crucial information for the understanding of lubrication.

The structure of polymer melt/solid interfaces has been investigated by X-ray reflectivity (XRR)[76,77], surface force apparatus (SFA)[78,79], and atomic force microscopy (AFM)[80–82]. Tribological studies, such as friction force measurement, were also performed on these interfaces by SFA[79,83,84] and contact-mode AFM[85]. These methods are capable of subnanometer-resolution analysis normal to the surface, and these studies revealed the nanoscale interfacial structures. Nevertheless, atomic-scale structural analysis in the lateral direction on polymer melt/solid interfaces has not been reported.

After the achievement of atomic-resolution imaging in water by FM-AFM reported by T. Fukuma et al. in 2005[24], FM-AFM utilizing Si cantilevers has been

applied to molecular-resolution imaging in organic solvents[25,26] and ionic liquids[27]. In recent years, the model system of lubricant/solid interfaces was investigated, and the lubrication layer was visualized at the molecular scale[30–32]. However, high-resolution imaging in viscous liquids, such as polymer melts, by using Si cantilevers is considered to be difficult because its Q factor further decreases due to the viscosity of the liquid, and the force sensitivity is seriously suppressed.

To overcome this issue, the use of a quartz tuning fork sensor, the so-called qPlus sensor, was proposed[44]. The Q factor of the qPlus sensor was kept higher than 100 by immersing only the tip apex into the liquid. Atomic-resolution imaging in viscous IL, of which viscosity is 300 times higher than that of water, was achieved[45]. In addition, the cross-sectional solvation structure was visualized by XZ two-dimensional frequency shift mapping (XZ 2D Δf mapping) at IL/solid interfaces[45,86].

These studies indicated the possibility of the application of qPlus sensors to high-resolution imaging in polymer melts, which has a high viscosity and large molecule size. In this chapter, a polymer melt/solid interface was investigated by FM-AFM using qPlus sensors. The atomic structure of the solid surface was successfully imaged in poly(dimethylsiloxane) (PDMS) melt, a silicone oil that has 1000 times higher viscosity than that of water. XZ 2D Δf mapping was also demonstrated at PDMS melt/solid interfaces, and the cross-sectional interfacial structure was visualized at the molecular scale. The energy dissipation-distance curve shows the fluid-like response of the PDMS melt near solid surfaces.

3.2 Experimental

3.2.1 Materials

Polydimethylsiloxane

Poly(dimethylsiloxane) (PDMS) $[(CH_3)_3Si\text{-}O\text{-}[Si(CH_3)_2\text{-}O]_n\text{-}\ Si(CH_3)_3]$ was used as a model polymer melt. It is known as typical silicone oil, of which the photograph and chemical structure are shown in Fig. 3.1. PDMS has siloxane bonds (Si-O-Si) in the chain backbone and two methyl groups per silicon-oxygen unit. There is a wide variety of viscosity of PDMS melt due to its molecular weight. The structures and dynamic properties of PDMS melt/solid interfaces have been studied by XRR[76,77], SFA[3,78,79,83,84], and contact-mode AFM[81,82,87].

PDMS (KF-96-1000cs) was purchased from Shin-Etsu Chemical Co., Ltd. and used without further purification. The PDMS used in this study has a viscosity of 970 mPa·s at 25°C[88], and number-average molecular weight M_n ∼26000 g mol^{-1} calculated from the viscosity[89].

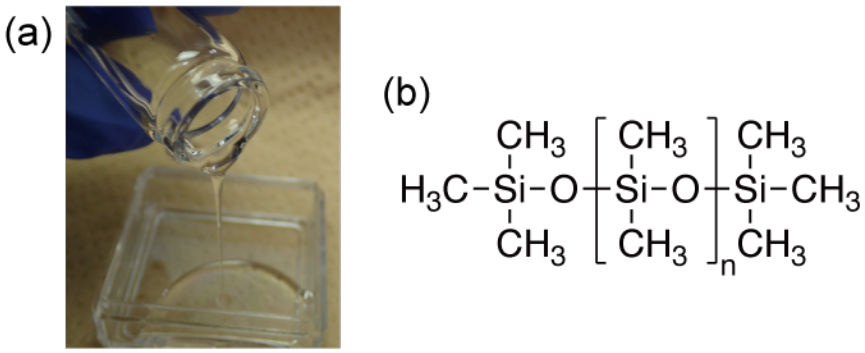

Figure 3.1: (a) A photograph of the PDMS (Shin-Etsu Chemical Co., Ltd., KF-96-1000cs). (b) The chemical structure of PDMS. The number-average polymerization degree n of KF-96-1000cs is about 350.

Muscovite Mica

A muscovite mica [$KAl_2(Si_3Al)O_{10}(OH)_2$] was used as a solid sample for topographic imaging and XZ imaging. Figure 3.2 shows the crystal structure of muscovite mica. The cleaved mica surface (Fig. 3.2 b) consists of hexagonal-arranged Si atoms (one-quarter are randomly replaced by Al atoms) and ditrigonal-arranged O atoms forming slightly distorted hexagons with a period of 0.52 nm[90]. The negative charge of tetrahedral layers due to the replacement of one of four Si atoms by Al atoms is neutralized by the K^+ between the opposing tetrahedral layers. It is easy to obtain clean atomically-flat surfaces of mica by cleavage. Muscovite mica is widely used for the model sample of high-resolution FM-AFM imaging in various liquids, such as water[24,28] and ionic liquids[44].

3.2.2 Experimental Setup

A quartz tuning fork (purchased from SII Crystal Technology Inc.), whose resonance frequency was 32.768 kHz, was used. Its spring constant was about 1.9×10^3 N m^{-1} calculated from its shape. One prong of the tuning fork was bound to a mount, and a tungsten wire (The Nilaco Co., diameter 0.1 mm) electrochemically etched in

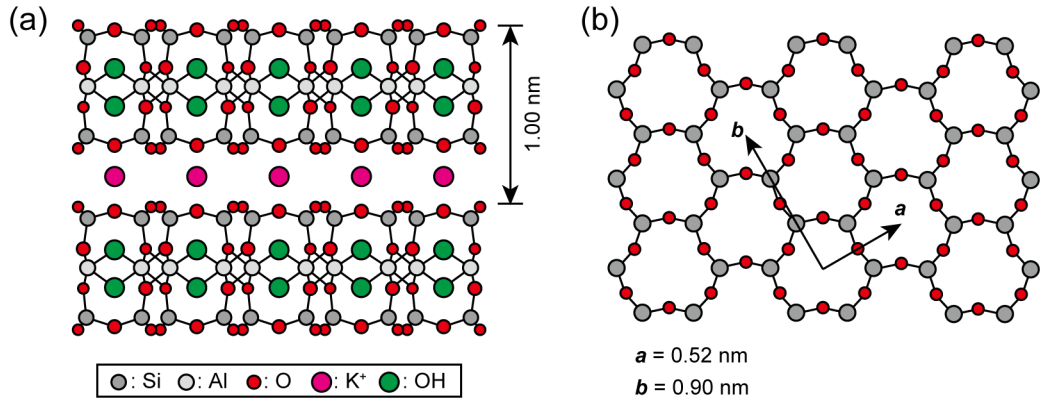

Figure 3.2: Crystal structure of muscovite mica. One of four Si in the tetrahedral layers is randomly substituted for Al, resulting in the negative charge, which is neutralized by the K^+ between the opposing tetrahedral layers. (a) [110] projection. (b) The basal plane [001] of the cleaved surface, showing the *a* and *b* vectors of the unit cell.

potassium hydroxide aqueous solution (1.2 mol l^{-1}) was glued to the other prong by EPO-TEK H70E (Epoxy Technology, Inc.). The length of the tungsten tip was about 1 mm, which is relatively larger than the typical value used in qPlus sensors. The experiment was performed by a system based on a commercial AFM (JEOL, JSPM-5200), of which the original AFM head was replaced by a home-built AFM head made for a qPlus sensor.

Figure 3.3 a shows a block diagram of the setup of the FM-AFM using a qPlus sensor. The sensor was mechanically oscillated by a lead zirconate titanate (PZT) piezoelectric plate driven at the resonance frequency. The deflection signal of the sensor was amplified by a differential current amplifier[69] embedded in the AFM head. The frequency shift Δf was detected by a commercial FM demodulator (Kyoto Instruments, KI-2001) with some modifications. Topographic images were obtained as two-dimensional maps of the tip trajectory where Δf was kept constant (Fig. 3.3 b). XZ 2D Δf mapping was performed by repeating the Δf-distance curve measurement changing the lateral position of the tip (Fig. 3.3 c).

3.2.3 Dynamics of the Sensor Immersed in Polymer Melt

Figure 3.4 a shows the thermal noise spectra of the qPlus sensor measured in ambient air and in the PDMS with various immersion depths (5, 10, 20, 50, 100, 200

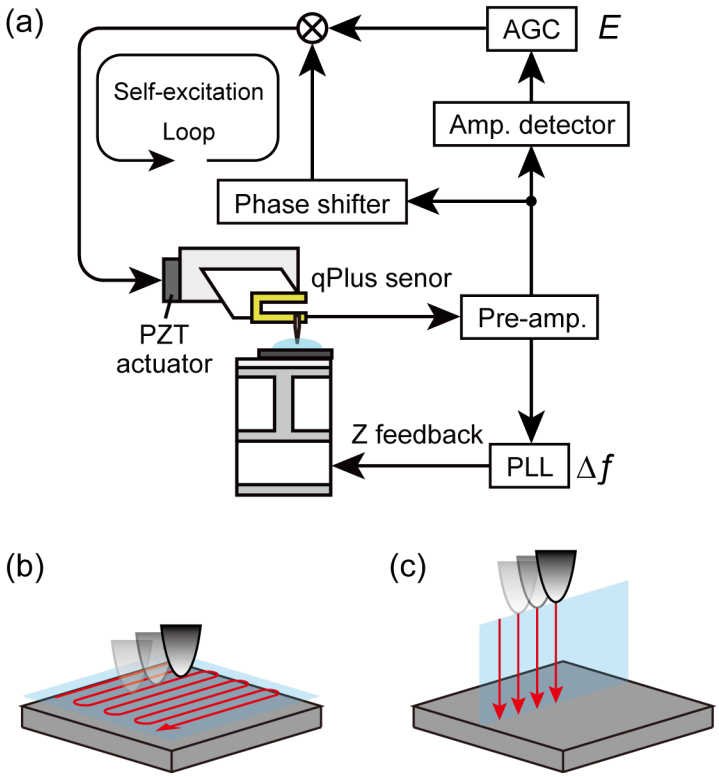

Figure 3.3: (a) Schematic block diagram of FM-AFM. (b) Schematic illustration of topographic imaging. (c) Schematic illustration of 2D Δf mapping.

μm). The resonance frequencies and Q factors of the sensor in each condition are summarized in Table 3.1. The Q factor drastically decreased by increasing the immersion depth because the motion of the sensor was damped by the viscosity of the liquid. However, as shown in Fig. 3.4 b, the sensor was not over-damped even when the tip was immersed 200 μm into the PDMS.

It is well known that the resonance frequency usually shifts negatively by the viscous effects when the system is modeled as a damped harmonic oscillator. In previous reports utilizing qPlus sensors, the negative frequency shift in water and ionic liquids was reported[44]. However, the resonance frequency of the qPlus sensor immersed in the PDMS shifted positively during increasing immersion depth up to 50 μm. The resonance frequency f is given by $f = 1/2\pi\sqrt{k/m^*}$, where k is the spring constant and m^* is the effective mass. The positive frequency shift results from effective spring constant increase Δk caused by conservative interactions. There

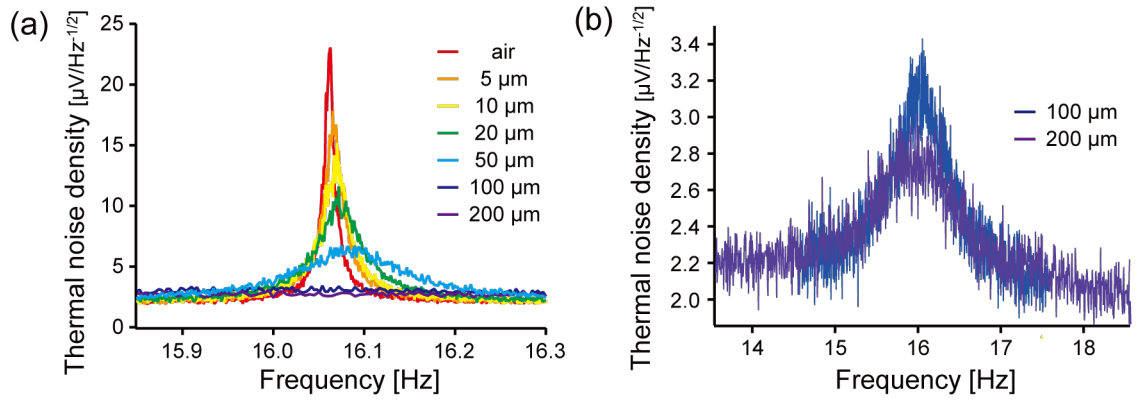

Figure 3.4: (a) Thermal deflection spectra of qPlus sensor obtained in various conditions, in ambient air, and in the PDMS with various immersion depths (5, 10, 20, 50, 100, 200 μm). (b) An enlarged graph of (a) for immersion depths of 100 and 200 μm.

Table 3.1: The resonance frequency and the Q factor of the qPlus sensor in each condition, in ambient air, and in the PDMS with various immersion depths (5, 10, 20, 50, 100, 200 μm).

	f [Hz]	Q factor
Air	16062	1952
5 μm	16066	966
10 μm	16069	681
20 μm	16073	392
50 μm	16085	143
100 μm	16036	22
200 μm	15947	13

are two possible conservative interactions; (1) the effective spring constant of the meniscus formed at the air-liquid-solid interface, which is determined by the surface tension of the liquid and the meniscus shape[91–93] and (2) the elastic component of the viscoelastic behavior of the PDMS[94,95].

The effective spring constant of the unbonded meniscus k_{men} is given by[93],

$$k_{men} = \frac{2\pi\gamma}{\ln\left(\frac{\kappa^{-1}}{r}\right) - \ln(1+\sin\theta) + \frac{1}{\sin\theta} + \ln 4 - \gamma_E - 1},$$

$$\kappa^{-1} = \sqrt{\frac{\gamma}{\rho g}}$$

where κ^{-1}, γ, and ρ are capillary length, surface tension, and density of the liquid. r and θ are the radius and contact angle of the liquid/solid interface. γ_E and g are Euler constant ($\simeq$0.577) and gravitational acceleration. Table 3.2 shows the parameters described above of the PDMS and water. In the case of r =5 μm, calculated k_{men} of the PDMS (2.2×10^{-2} N m^{-1}) was smaller than that of water (6.7×10^{-2} N m^{-1}). Therefore, the contribution of k_{men} to the positive frequency shift is considered to be small in this experimental system.

The viscoelastic behavior of various liquids has been investigated for decades. According to them, although there are only comparable data of the viscoelasticity measurements, which were carried out at a shear rate of 75 kHz, the PDMS melt has larger bulk shear elasticity than that of water[94,96,97]. It is considered that the bulk shear elasticity of the PDMS mainly contributes to the positive frequency shift of the sensor. By further increasing the immersion depth up to 100 and 200 μm, the resonance frequency shifted negatively. That is because the contribution to the frequency shift of the viscous effect became larger than that of the conservative interactions mentioned above. To minimize the experimental error caused by the frequency shift, the phase of the deflection signal was adjusted by the phase shifter (shown in Fig. 3.3 a) 200-1000 nm above the surface before imaging.

Table 3.2: The physical parameters (surface tension γ, density ρ, capillary length κ^{-1}, and contact angle θ) of the PDMS and water. The contact angle was measured by using a tungsten wire with a diameter of 0.1 mm.

	γ [mN m^{-1}]	ρ [g cm^{-1}]	κ^{-1} [mm]	θ [°]
PDMS (KF-96-1000cs)	21.2	0.97	1.5	55
Water	72.8	1.00	2.7	51

3.2.4 Sample Preparation

The muscovite mica substrate (Furuuchi Chemical Co.,) was cleaved by using scotch tape, and immediately a 1 μl droplet of PDMS (Shin-Etsu Chemical Co., Ltd., KF-96-1000cs) was put on the cleaved mica surface in a drying chamber (dew point < -50 °C). This sample was left in the drying chamber for over 12 hours in order to settle the droplet shape. Then, the PDMS/mica interface was investigated by FM-AFM

using a qPlus sensor in ambient conditions (temperature ∼24°C, relative humidity ∼30 %).

The contact angle of the PDMS on mica was less than 5° 12 hours after dropping. The thickness of the PDMS was typically less than 100 μm in this experimental condition. In this situation, the Q factors of the qPlus sensors were more than 30. Therefore, it was expected that qPlus sensors would have high force sensitivity even in the PDMS.

3.3 Subnanometer-scale Investigation of PDMS Melt/Mica Interface

3.3.1 Atomic Structure Imaging of Mica Surface in PDMS Melt

Figure 3.5 shows a topographic image of a cleaved mica surface obtained in the PDMS. Atomic-scale contrast with the honeycomb-like pattern with a period of 0.5 nm was imaged. The cleaved mica surface consists of hexagonal-arranged Si atoms (one-quarter are replaced by Al atoms) and ditrigonal-arranged O atoms forming slightly distorted hexagons with a period of 0.52 nm[90]. The insert in Fig. 3.5 shows the structure of the cleaved mica surface. The topographic image was in good agreement with the structure of the mica surface. The honeycomb-like pattern is considered to reflect ditrigonal-arranged oxygen atoms and hexagonal-arranged Si (Al) atoms on the mica surface. This result indicates that FM-AFM using qPlus sensors is capable of subnanometer-resolution imaging in viscous polymeric liquid. The viscosity of the PDMS used in this study (970 mPa·s) is 1000 times higher than that of water (0.87 mPa·s). This result also indicates that the tip apex directly interacts with the surface even in such a polymeric liquid with a large molecular length (>100 nm).

3.3.2 XZ Imaging on PDMS Melt/Mica Interfaces

Figure 3.6 a shows the XZ Δf map obtained at the PDMS-mica interface. The stripe-like structure of Δf distribution parallel to the surface was imaged. As shown in Fig. 3.6 b, the oscillation period of Δf was reproducibly 0.7-0.9 nm, which is roughly equal to the diameter of the PDMS molecules. The frequency shift Δf is in a linear relationship with the force gradient under the assumption that the oscillating

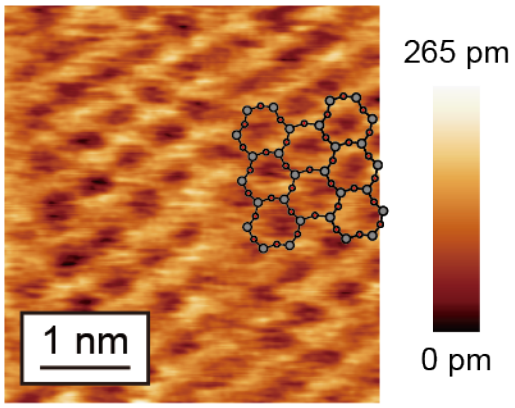

Figure 3.5: A topographic image of a cleaved mica surface obtained in the PDMS. 5 nm × 5 nm, f=15374 Hz, Q=27, A_{0-p}=190 pm, Δf=+53 Hz. The insert shows the structure of the cleaved mica surface. The gray and red dots show hexagonal-arranged Si (Al) atoms and ditrigonal-arranged O atoms, respectively.

amplitude is small enough[71]. Therefore, the force and the potential also have a distribution similar to the Δf distribution ($\sim$ the force gradient distribution). Since the PDMS molecules used in this study were quite large (>100 nm), solvent tip approximation[65,66] cannot be applied to this experimental system. However, it can be qualitatively said that there is a density distribution if there is a distribution in the potential. Therefore, it is considered that there is a density distribution of the PDMS with a period of 0.7-0.9 nm at the PDMS/mica interface. That agreed with the previous reports on XRR studies on PDMS (weight-average molecular weight M_w ~550, 770, 2000, 28000 g mol^{-1})/SiO_2 interfaces where the oscillated density with the period of 0.8-1.0 nm was observed[76,77]. That was also in good agreement with the period of the oscillated force (0.8-1.0 nm) detected by contact-mode AFM, which was performed in the PDMS (M_w ~18000 g mol^{-1}) on SiO_2 and mica[81,82]. Although the layered structure of density distribution of PDMS molecules near solid surfaces was already pointed out by such one-dimensional (1D) measurements, the XZ 2D Δf map obtained in this work shows it more obviously. On the other hand, the oscillation period of Δf obtained in this study was slightly larger than the value obtained by SFA studies (~0.7 nm)[78,79,83]. It might be because the confinement effect in SFA experiments is larger than that of AFM experiments.

Figure 3.6 c shows the XZ energy dissipation map simultaneously obtained with

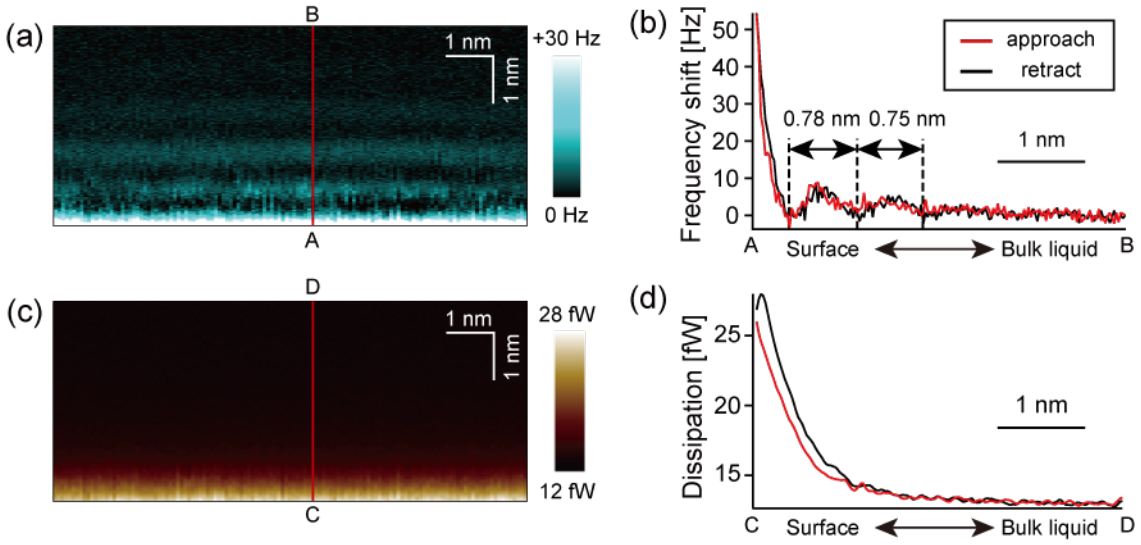

Figure 3.6: (a) A XZ Δf map obtained at the PDMS/mica interface. (b) A Δf-distance curve corresponding to the line AB in (a). (c) A XZ energy dissipation map obtained simultaneously with (a). (d) An energy dissipation-distance curve corresponding to the line CD in (c), which was obtained simultaneously with (b). 10 nm $\times$ 4.2 nm, f=18842 Hz, Q=354 and A_{0-p}=190 pm.

the Δf map shown in Fig. 3.6 a. It shows no layered structure, although the Δf map shows the layered structure. That is also indicated by the monotonic energy dissipation-distance curve shown in Fig. 3.6 d, which was obtained simultaneously with the Δf-distance curve shown in Fig. 3.6 b. Several previous FM-AFM studies showed the oscillatory[98,99] or periodic-peaking[100] dissipation-distance curves, and they were explained by the solidification of the solvation layers. Namely, the monotonic increase of energy dissipation as the tip approaching in this experiment indicates that the PDMS molecules near the mica surface showed a fluid-like behavior and that the solidification did not occur. S. Yamada has reported a SFA study on PDMS (M_w 80000 g mol^{-1}) placed between two mica surfaces[79]. He showed that the PDMS with a thickness of three or more molecular layers exhibited solid-like behaviors while the PDMS with two layers-thickness, in which both the layers contacted the mica surface and exhibited a viscous-like shear response. However, our results indicated that the PDMS molecules behave fluid-like even beside the mica surface. As shown in Fig. 3.5, the crystal structure of the mica surface was imaged in the PDMS, that is, the tip apex directly interacts with the mica surface. In addition,

the monotonic increase of the energy dissipation indicated the fluid-like behavior of the PDMS. This difference might be due to the confinement effects of the SFA experiments, the molecular weight of PDMS, or the presence of water[78] caused by humidity in our experimental condition.

Figure 3.7 shows the XZ Δf maps obtained in the same experimental condition. Although the layered Δf distribution was imaged on the right part in Fig. 3.7 a, it was not visible on the left part of the image. Fig. 3.7 b shows the subnanometer-scale Δf distribution in both the vertical and lateral directions. To the best of our knowledge, these types of images have not been reported on organic solvent/solid interfaces. It might be because of phenomena peculiar to polymers (entanglement etc.) or high flexibility[101] of siloxane bonds (Si-O-Si), the main chain of PDMS.

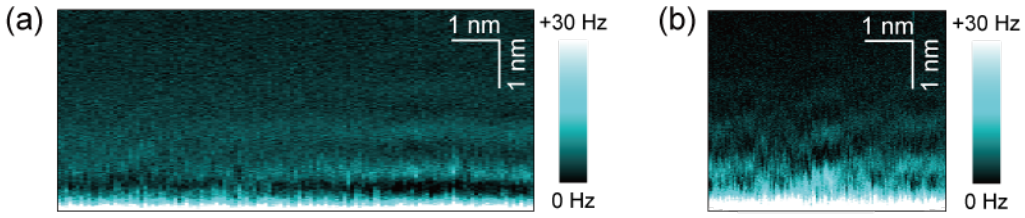

Figure 3.7: ((a) XZ Δf map where the layered structure was partially visible. 10 nm $\times$ 4.2 nm, f=18842 Hz, Q=354 and A_{0-p}=190 pm (b) XZ Δf map with vertical and lateral distribution. 5 nm $\times$ 4.2 nm, f=14572 Hz, Q=180 and A_{0-p}=180 pm.

3.4 Summary

In this chapter, FM-AFM with a qPlus sensor was applied to polymer melt/solid interfaces.

1. The crystal structure of the mica surface was successfully imaged in PDMS melt, of which viscosity is 1000 times higher than that of water.

2. The XZ 2D Δf mapping was also demonstrated at the interface and the layered structure of density distribution of the PDMS was imaged, of which period agrees with the diameter of PDMS molecules and previous reports using XRR and contact-mode AFM. The lateral variation of the Δf distribution was also imaged, which has not been achieved by previous 1D measurements.

3. The monotonic energy dissipation curve indicated the fluid-like behavior of the PDMS near the mica surface.

These results indicated that FM-AFM using qPlus sensors would be quite useful for atomic-scale analysis of lubrication using practical lubricants, including polymeric liquids.

Chapter 4

Lateral Tip Oscillation in Higher Modes of qPlus Sensor with Long Probe

4.1 Introduction

Detecting the vertical and lateral forces at the nanometer scale by atomic force microscopy (AFM) can provide essential knowledge on tribological issues[9]. To access the vertical and lateral interactions simultaneously in dynamic AFM, it is required that the tip oscillates in the vertical and lateral directions separately in independent modes, the so-called bimodal AFM. In the case of Si cantilevers, it is realized by utilizing its flexural and torsional modes detected by an optical beam deflection detector with a quadrant photodiode[20–22,102] or by an optical interferometer system[23]. Atomic-scale friction analysis was demonstrated in ultra-high vacuum (UHV) environments[20,22] and recently in water[102]. However, it is difficult to apply dynamic AFM with Si cantilevers to viscous liquid environments such as lubricant oil/solid interfaces because the quality factor of the Si cantilever decreases, and the force sensitivity is seriously suppressed.

On the other hand, subnanometer-scale imaging on the polymer melt/solid interface is achieved using the qPlus sensor in Chapter 3. In these reports, the vertical tip-sample interaction was detected for regulating the tip-sample distance. The probe was attached perpendicularly to the QTF prong, and its tip oscillated verti-

cally to the surface in its fundamental flexural mode (Fig. 4.1 a). However, torsional oscillations cannot be detected because commercially available QTFs are generally manufactured for detecting flexural oscillations.

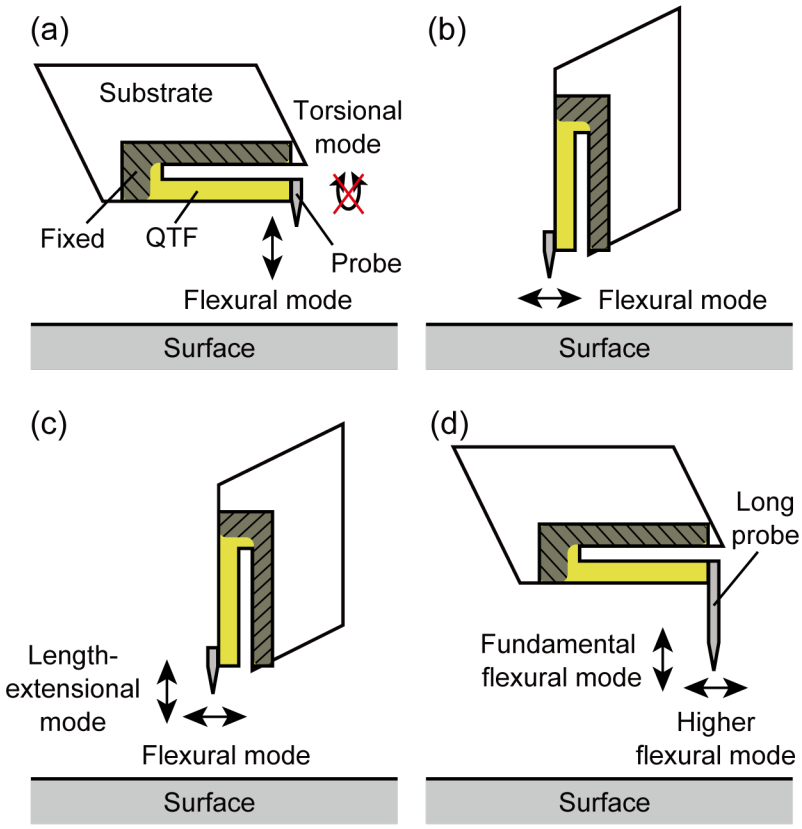

Figure 4.1: Schematic illustrations of the four types of qPlus sensors (a) Conventional qPlus sensor. A prong and the base of a QTF are fixed to a substrate (the gray-colored shaded area). The torsional mode cannot be detected by the piezoelectric effect of the QTF. (b) LFM qPlus sensor. A probe is attached parallel to the QTF prong. (c) qPlus sensor for biaxial excitation. A probe is attached parallel to the QTF prong with a different electrode arrangement. (d) qPlus sensor with a long probe (this study). A long probe is attached perpendicularly to the QTF prong.

By attaching the probe parallel to the QTF prong and rotating the sensor by 90°, the tip oscillates parallel to the surface (Fig. 4.1 b). The lateral tip-sample interaction can also be detected with atomic resolution by lateral force microscopy (LFM) utilizing this qPlus sensor[17,49,50,103]. Namely, the vertical and lateral forces can be individually detected by qPlus sensors with different arrangements. However,

simultaneous detection of both vertical and lateral forces with a single qPlus sensor had not been reported until recent years.

Kirpal *et al.*[54] recently presented a method to simultaneously excite the fundamental flexural and length-extensional modes of a qPlus sensor, where the probe was attached parallel to the QTF prong (biaxial excitation). By setting the QTF prong perpendicular to the surface, the vertical and lateral movements of the tip were provided by the length-extensional and flexural modes, respectively (Fig. 4.1 c). They achieved atomic resolution in both modes in UHV and ambient conditions. However, the electrode arrangement of the QTF they used, which is required for detecting the length-extensional mode, differs from that of conventional QTFs.

In this Chapter, the qPlus sensor with a long probe (> 1 mm) attached perpendicularly to the long axis of the QTF prong (Fig. 4.1 d) was adopted. It was found that the tip apex of the sensor oscillates vertically at the lowest eigenfrequency f_1 and laterally at the second lowest eigenfrequency f_2 by the finite element method (FEM) simulation. Atomic resolution imaging of KBr(100) was demonstrated by the bimodal AFM using f_1 and f_2 of the qPlus sensor to confirm the lateral tip oscillation at f_2. Energy dissipation measurement on graphene oxide (GO) sheets spin-coated on a highly oriented pyrolytic graphite (HOPG) substrate is also demonstrated by the bimodal AFM to confirm that the surface properties can be detected by f_2 mode.

4.2 Eigenmode Analysis with Finite Element Method (FEM)

4.2.1 Eigenfrequencies of the qPlus Sensor with Long Probe

First, the eigenfrequencies of a qPlus sensor with a long probe were experimentally measured. One prong of a commercial quartz tuning fork (QTF, STATEK Co., TFW 1165, spring constant 1884 N m^{-1}) was bound to a mount. A tungsten wire (The Nilaco Co., diameter 0.1 mm) was electrochemically etched in potassium hydroxide aqueous solution (1.2 mol $^{-1}$) and glued to the other prong by EPO-TEK H70E (Epoxy Technology, Inc.). The length of the tungsten probe was 1.33 mm, which is relatively larger than the typical value used in qPlus sensors.

Figure 4.2 a shows the photograph of the qPlus sensor used in this experiment. Figures 4.2 b and c show the thermal Brownian spectra of the qPlus sensor around

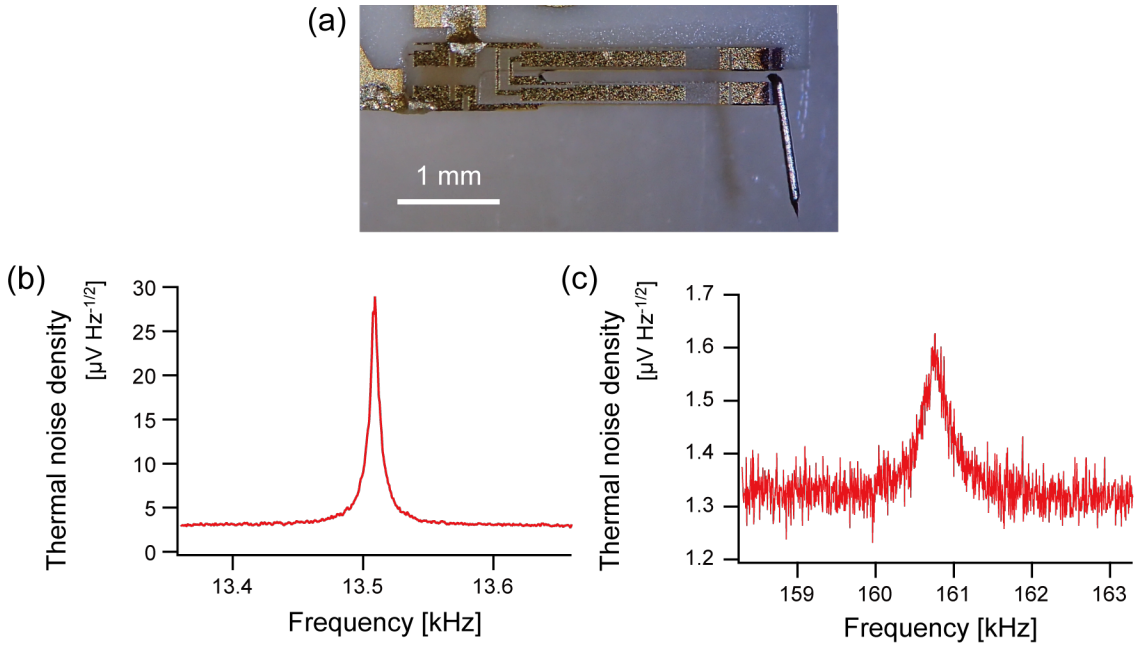

Figure 4.2: (a) Photograph of the qPlus sensor used in this experiment. (b, c) Thermal noise spectra of the qPlus sensor obtained in ambient air around the first eigenfrequency ((b), $f_1 = 13.509$ kHz, $Q_1 = 2439$) and around the second eigenfrequency ((c), $f_2 = 160.760$ kHz, $Q_2 = 423$).

the first two peaks obtained in ambient air. The first two eigenfrequencies were $f_1 = 13.509$ kHz and $f_2 = 160.760$ kHz. The quality factors (Q factors) of f_1 and f_2 were 2439 and 423 respectively. The second eigenfrequency, f_2, was 11.9 times higher than f_1. It is quite different from theoretical values of the cantilever's second and third eigenfrequencies (6.27 times and 17.6 times of f_1) because higher eigenmodes of qPlus sensors are drastically affected by the mass and rotation inertia of the long probe[51].

Preferring Ref. 51 (Tung *et al.*, *J. Appl. Phys.*, 2010), eigenfrequencies and modes were calculated considering the mass and rotation inertia of the probe. In this method, only in-plane oscillations (vertical oscillations) of the QTF were considered. The probe was approximated as a rigid circular column length of 1.17 mm in order to equalize its mass to the actual amount. The solutions of the first three eigenfrequencies were 13.8 kHz, 64.2 kHz, and 240 kHz, and their oscillation modes of them are shown in Fig. 4.3. The calculated first eigenfrequency was in good agreement with the experimental values of f_1. In contrast, the root corresponding to f_2

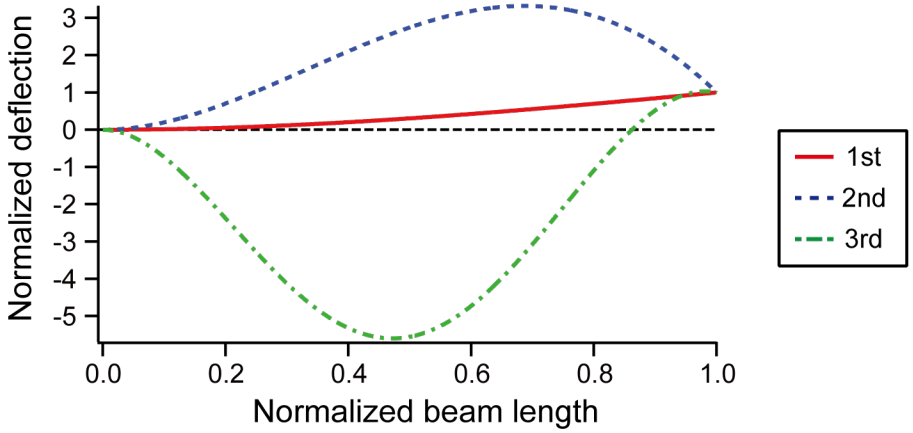

Figure 4.3: Calculation results of eigenmodes obtained by the theory described in Ref. 51 approximating the probe as a rigid circular column. The solutions of the first three eigenfrequencies were 13.8 kHz (red solid line), 64.2 kHz (blue broken line), and 240 kHz (green dashed-dotted line).

was not theoretically obtained. In fact, the spring constant of the probe calculated by approximating the probe as a circular column is 2730 N m^{-1}, which is the same in order of magnitude as that of the QTF beam in the in-plane direction, 1884 N m^{-1}. Furthermore, the spring constants of higher eigenmodes are generally much higher than that of the fundamental mode. Therefore, there is the possibility that the probe doesn't behave as a rigid body at f_2, and the rigid-probe approximation was not suitable in this case. The results also suggested the presence of out-of-plane or torsional oscillation modes. These modes, however, are considered less likely to be detected by the piezoelectric effect of QTFs because they are manufactured for sensing in-plane oscillation.

4.2.2 Eigenmode Analysis with FEM

The calculated frequencies at higher eigenmodes under the rigid-probe approximation are obviously different from the experimental values. In order to investigate the eigenmodes of the qPlus sensor more exactly, FEM simulations were carried out. The probe attached to the qPlus sensor had tilted 8° from the perpendicular direction of the QTF beam (Fig. 4.4 a), which was reflected in the simulation model (Fig. 4.4 b). FEM simulation was carried out by FreeCAD (ver. 0.17), an open-source 3D parametric modeler with FEM solvers, in order to reveal the oscillation modes of the

qPlus sensor numerically. Table 4.1 shows the physical parameters of the QTF and the tungsten probe. It was approximated that the QTF and the probe were bonded by a plane, and the QTF, except for the prong with the probe, was fixed. The creation of a mesh and the solution of eigenmodes were conducted by Gmsh and Calculix on FreeCAD.

Table 4.1: The physical properties of the QTF and the tungsten probe used for the calculation and FEM simulation.

Quartz tuning fork		Tungsten probe	
Young's modulus	80 GPa	Young's modulus	345 GPa
Poisson's ratio	0.17	Poisson's ratio	0.284
Density	2650 kg m^{-3}	Density	19300 kg m^{-3}
Length	2.357 mm	Length	1.33 mm
Width	0.2134 mm	Diameter	0.1 mm
Thickness	0.127 mm		

The simulation results of the first six eigenfrequencies were obtained at 7.94 kHz, 13.4 kHz, 32.6 kHz, 43.5 kHz, 94.0 kHz, and 162 kHz, and the oscillation modes of them are shown in Fig. 4.4 c-h. The frequencies of the oscillation modes shown in Fig. 4.4 d and h agree well with the experimental values of f_1 and f_2 respectively, and the QTF vertically oscillates at both f_1 and f_2. Although the simulation suggests that the QTF oscillates in the vertical direction at 43.5 kHz (Fig. 4.4 f), the deflection signal of this mode was not detected by its piezoelectric effect. This is ascribed that this mode mostly consists of the tip oscillation, and the QTF oscillation is negligibly small. The others consist of out-of-plane or torsional oscillation, which was not detectable by the piezoelectric effect.

Figures 4.4 i and j side views of eigenmodes at f_1 and f_2 (Fig. 4.4 d and h), respectively. According to them, the probe also bends at f_2, and the tip apex oscillates in a direction orthogonal to that of f_1. The deflection of the QTF end at f_2 was relatively small, and the probe bent to +x (-x) direction when the middle part of the QTF deflected to +z (-z) direction. Figure 4.4 k is the image of the tip apex displacement at f_2 viewed from a side. The misalignment from the lateral direction was 7°, which indicates that the crosstalk of vertical force was suppressed to 12 % and the lateral force was dominantly detected. It was also found that the misalignment can

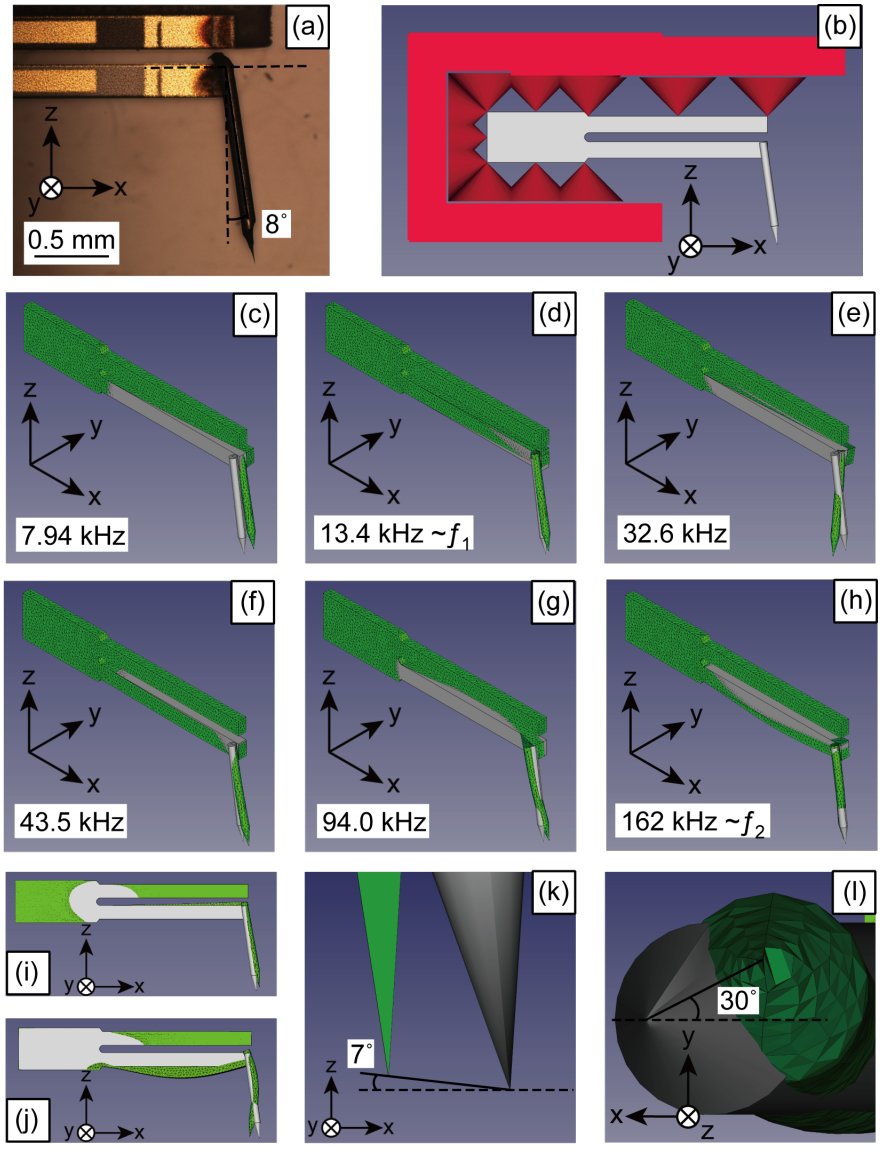

Figure 4.4: (a) An optical microscope image of the probe attached to the qPlus sensor used in this experiment. The probe was tilted 8degree from the long axis of the QTF. (b) A 3D parametric model of the qPlus sensor. Red bodies indicated fixed boundary conditions. (c)-(h) FEM simulation results of the eigenmodes. The first six eigenfrequencies were 7.94 kHz (c, out-of-plane), 13.4 kHz (d, in-plane), 32.6 kHz (e, torsion), 43.5 kHz (f, in-plane and probe-bending), 94.0 kHz (g, out-of-plane and probe-bending) and 162 kHz (h, in-plane and probe-bending). (i) The side view of (d). (j) The side view of (h). (k) The tip apex of (h) viewed from a side. The misalignment from the lateral direction is 7degree. (l) The tip apex of (h) viewed from the bottom. The dithering direction of the probe apex tilted 30degree from the long axis of the quartz beam.

be decreased to 1° by elongating the probe length to 2 mm, where the crosstalk is suppressed less than 2 %. Figure 4.4 l is the image of the eigenmode at f_2 viewed from the bottom. It was found that the angle formed by the direction of the tip apex oscillation and the long axis of the QTF is about 30°. This is probably because the probe was attached to the side of the QTF, and that made some torque around the long axis of the QTF. Additionally, it was confirmed that the effect of the adhesive on the oscillation modes was negligibly small. At this stage, it is considered that the tip apex oscillates in the lateral direction at f_2, while it is difficult to interpret the deflection signal of f_2 to its actual amplitude because of the complex coupled motion of the QTF and the probe.

4.3 Experimental Confirmation of Lateral Tip Oscillation

In the previous section, it was found that the tip apex of the qPlus sensor with a long tip oscillates vertically at f_1 and laterally at f_2 by FEM simulation. In order to experimentally confirm this simulation result, atomic resolution imaging was conducted by the bimodal AFM with the qPlus sensor.

4.3.1 Experimental Setup

The experiment was performed by a system based on a commercial AFM (JEOL, JSPM-5200), of which the original AFM head was replaced by a home-built AFM head made for a qPlus sensor. Fig. 4.5 shows a block diagram of the bimodal AFM setup. The qPlus sensor used in this experiment was the same one analyzed in Sec. 4.2. The sensor was mechanically oscillated by a lead zirconate titanate (PZT) piezoelectric plate driven at two different resonance frequencies simultaneously. The deflection signal of the sensor was amplified by a differential current amplifier[69] embedded in the AFM head. The frequency shift of the lowest resonance frequency (Δf_1) was detected by a commercial FM demodulator (Kyoto Instruments, KI-2001) with some modifications, and amplitude and phase shift at the second lowest resonance frequency (A_2, ϕ_2) were detected by a lock-in amplifier (NF Electronic Instruments, LI 5640). Topographic images were obtained as two-dimensional maps of the tip trajectory where Δf_1 was kept constant.

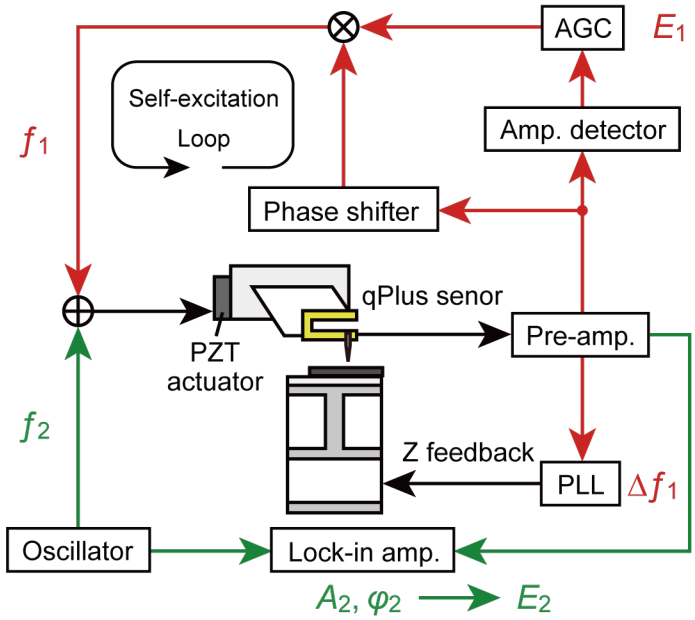

Figure 4.5: Experimental setup of FM-AM bimodal AFM utilizing qPlus sensor The sensor is simultaneously mechanically excited at f_1 and f_3. The first mode is operated by frequency modulation. The frequency shift of the first mode Δf_1 is detected by an FM demodulator and used for z-feedback. The amplitude of the first mode A_1 is kept constant, and the energy dissipation in the first mode E_1 is obtained from the driving amplitude. The third mode is excited at a constant frequency equal to f_3, with a constant driving amplitude. The amplitude and phase of the third mode (A_3 and ϕ_3) are detected by a lock-in amplifier. The energy dissipation in the third mode E_3 is derived from A_3 and ϕ_3.

4.3.2 Sample Preparation

A KBr(100) substrate was used as a standard sample for atomic resolution imaging. 1-Butyl-3-methylimidazolium hexafluorophosphate (BMIM-PF_6, > 98 %, Fig. 4.6) was purchased from Tokyo Chemical Industry Co., Ltd. and used without further purification. The saturated KBr solution of BMIM-PF_6 was prepared by adding 1 wt% of KBr powder (Nacalai Tesque Inc., > 99 %) and agitating on a tube rotator for 1 day. After that, a (100) oriented KBr single crystal (Furuuchi Chemical Co.) was cleaved by using a sharp knife, and immediately supernatant of the solution (0.5 μl) was dropped on the cleaved KBr(100) surface. This sample was left in the dry chamber (dew point < -50 °C) for 1 day, and then it was investigated by the

bimodal AFM.

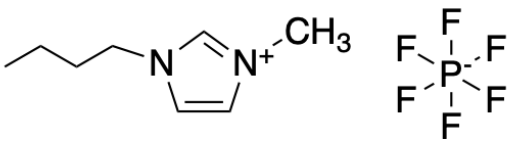

Figure 4.6: Chemical structure of BMIM-PF_6.

4.3.3 Results and Discussion

Figure 4.7 shows atomically resolved KBr(100) surface images obtained with the same fast scan direction in the saturated KBr solution of BMIM-PF_6 and their two-dimensional Fast Fourier Transform (2D-FFT) patterns. KBr has a rock-salt structure with a lattice constant a = 0.66 nm (Fig. 4.7 a). Figure 4.7 b was obtained by operating only the first mode with the amplitude A_1=180 pm. The square-lattice bright spots with the lattice spacing of 475 pm were clearly imaged, which are in good agreement with the spacing between equally charged ions, $\frac{a}{\sqrt{2}}$. Thus, the bright spots correspond to the periodic sites of only one atomic species as described in previous reports[47,73,104].

Figures 4.7 c, d, and e were obtained by bimodal AFM operating with constant A_1 (180 pm) and various A_2 (28.3 mV, 56.5 mV, and 113 mV). The lateral amplitude A_2 is described by the detected signal voltage because interpretation from the voltage to the actual lateral amplitude has not been achieved. Although the separated bright spots forming a square-lattice structure were imaged in Figs. 4.7 b and c, the image changed to stripe-like patterns as A_2 was increased, which can also be confirmed in the 2D-FFT patterns. That is, the imaged atoms were apparently connected to each other. These results are quite different from the previous report in which a short tip was used[104].

In atomic resolution images obtained by dynamic LFM[18] and scanning tunneling microscopy (STM) combined with dynamic LFM[49,59,60] in which the tip apex oscillates laterally, neighboring atoms in the direction of the tip dithering were apparently connected. In order that the direction of the observed stripes corresponds well to the direction of the tip apex oscillation in the FEM simulation (Fig. 4.4 l).

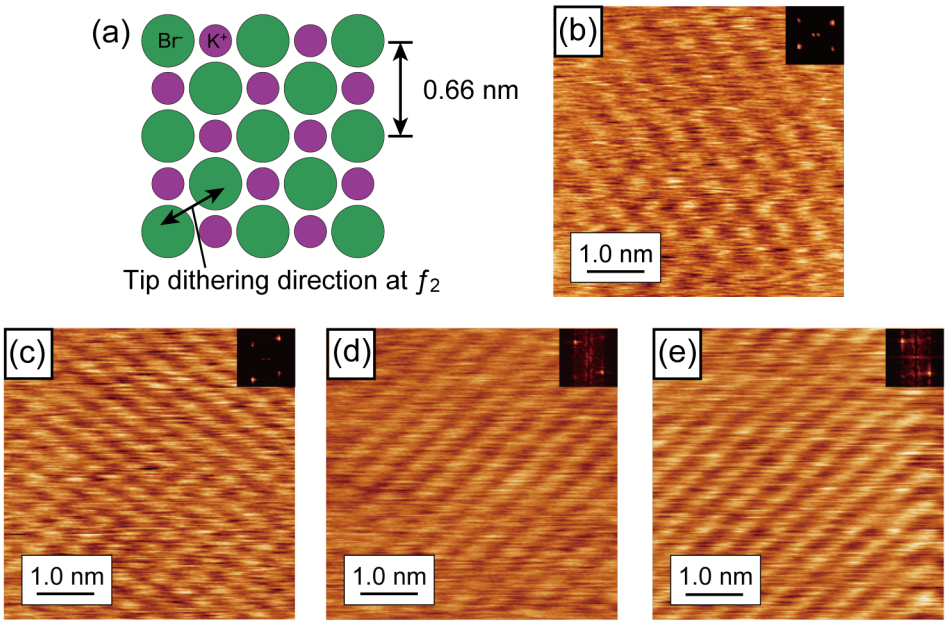

Figure 4.7: (a) A schematic illustration of KBr(100) surface and the tip dithering direction at f_2 (b)-(e) Topographic images and its FFT patterns of KBr(100) obtained in KBr-saturated BMIM-PF_6 by the bimodal AFM with constant A_1 (180 pm) and different A_2. Δf_1 was kept constant during each imaging. (a) A_2 = 0 mV, Δf_1 = +250 Hz (b) A_2 = 28.3 mV, Δf_1 = +280 Hz (c) A_2 = 56.5 mV, Δf_1 = +290 Hz (d) A_2 = 113 mV, Δf_1 = +260 Hz.

Therefore, these experimental results revealed that the tip apex oscillates laterally at f_2. In addition, considering the fact that atoms were separately imaged in Fig. 4.7 c with A_2 = 28.3 mV and were apparently connected in Fig. 4.7 d with A_2 = 56.5 mV, the lateral amplitude of the tip apex at f_2 can be roughly estimated to be in the same order as the lattice spacing.

4.4 Bimodal AFM with qPlus Sensor with Long Probe

It was confirmed by the atomic resolution imaging of KBr(100) that the tip apex of a qPlus sensor with a long tip oscillates laterally at f_2. The next step is the simultaneous detection of vertical and lateral forces by the bimodal AFM. In this section, force detection by the second mode was experimentally examined.

4.4.1 Experimental Setup

The experimental setup was the same as described in Sec. 4.3 except for using another qPlus sensor. The probe length of the qPlus sensor used in this experiment was 1.68 mm, and its f_1 was 11.222 kHz, and f_2 was 133.46 kHz.

4.4.2 Sample Preparation

Graphite and graphene oxide (GO, Fig. 4.8 b) were used as test samples for energy dissipation measurements. GO sheets were prepared through a modified Hummers method[105]. A highly oriented pyrolytic graphite (HOPG, SPI supplies, SPI-2 grade, 10 x 10 x 2 mm) was cleaved using scotch tape. The GO 1-propanol dispersion was spin-coated onto the cleaved HOPG surface. 1-Ethyl-3-methylimidazolium bis(trifluoromethylsulfonyl)imide (EMIM-Tf_2N, Fig. 4.9) was purchased from Kanto Chemical Co., Inc. and used without further purification. 0.5 μl of EMIM-Tf_2N was dropped on the GO-coated HOPG substrate, and the interface was investigated by the bimodal AFM.

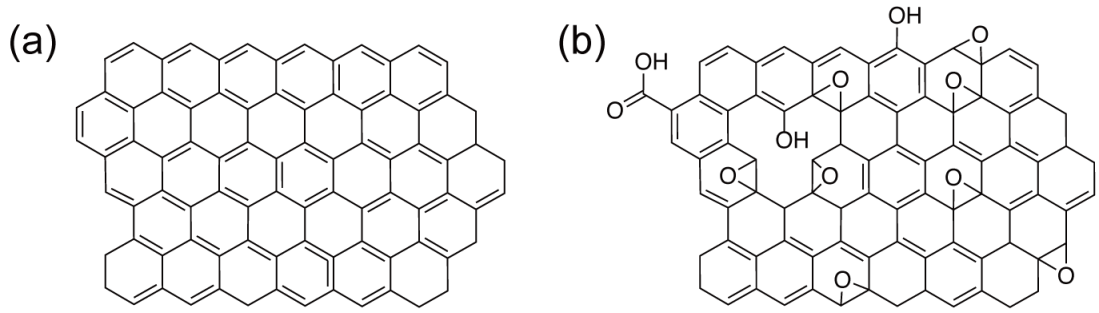

Figure 4.8: Chemical structure of (a) graphene and (b) graphene oxide (GO).

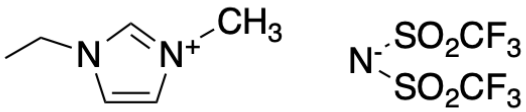

Figure 4.9: Chemical structure of EMIM-Tf_2N.

4.4.3 Results and Discussion

Figures 4.10 a-c show bimodal AFM results of the GO-coated HOPG substrate obtained in EMIM-Tf_2N. Protrusions were observed only in the upper area of the topographic image (Fig. 4.10 a). These are typical structures of GO sheets, which originated from the oxygen functional groups and the defects[106]. Thus, the upper area and the lower area correspond to the GO-covered area and the bare HOPG surface, respectively. The GO-covered area exhibits larger amplitude attenuation and phase shift of the second mode compared to the HOPG area, as shown in Figs. 4.10 b and c. It was also found that the height variation in the bare HOPG did not affect the amplitude and the phase of the second mode, which indicated that the surface properties are detected by the second mode without topographic effects.

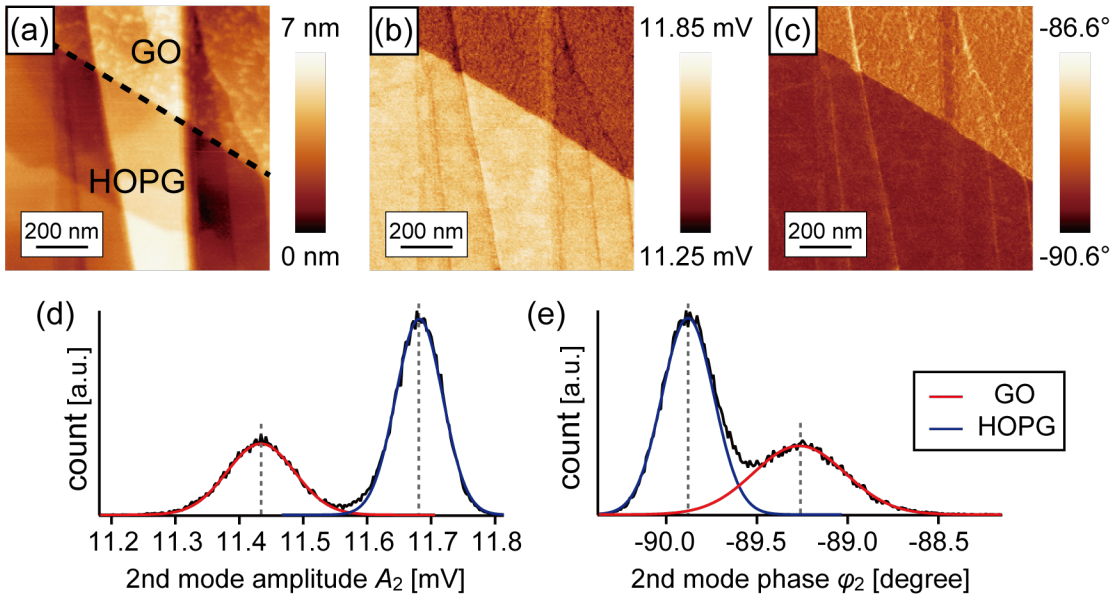

Figure 4.10: The bimodal AFM result of the GO-coated HOPG substrate obtained in EMIM-Tf_2N. (a) Topography. The broken line shows the edge of the GO sheet. (b) second mode amplitude. (c) second mode phase. $A_1 = 190$ pm, $A_2 = 11.9$ mV, and $\Delta f_1 = +82$ Hz. (d) Histogram of (b). (e) Histogram of (c). The red and blue curves are fitting curves with the Gaussian function.

The energy dissipation in the second mode is given by

$$E_2 = \frac{\pi k_2 A_2 f_2}{Q_2}\left(\frac{Q_2 A_{exc}}{A_2}\sin(-\phi_2) - \frac{f_{exc}}{f_2}\right), \tag{4.1}$$

where k_2 is the spring constant, and Q_2 is the quality factor of the second mode. f_{exc} is the excitation frequency, and A_{exc} is the excitation amplitude. Since $f_{exc} \simeq f_2$, and $Q_2 A_{exc}$ is equal to the amplitude of the second mode without any interactions $A_{2,0}$, E_2 ca be approximated as

$$E_2 = \frac{\pi k_2 A_2 f_2}{Q_2} \left(\frac{A_{2,0}}{A_2} \sin(-\phi_2) - 1 \right). \tag{4.2}$$

Although the absolute value of the energy dissipation cannot be obtained because k_2 and A_2 were not calibrated. However, the ratio of the energy dissipation on GO and HOPG can be obtained. According to the histograms (Figs. 4.10 d and e), the averaged amplitude and the averaged phase shift of the second mode on the GO-covered area were 11.43 mV and -89.27°, and those on the bare HOPG area were 11.68 mV and -89.88°. The relationship of the energy dissipation on these surfaces was obtained as $E_{2\_GO}/E_{2\_HOPG} = 2.1$.

The energy dissipation in the lateral oscillation can be originated from the friction force acting between the tip and the surface by considering the motion equation. Therefore, it is considered that the friction force detected on GO sheets by this bimodal AFM was larger than on HOPG. The result was in qualitative agreement with that of a previous report by contact-mode LFM utilizing Si cantilevers, where GO showed larger friction forces than HOPG[107]. However, there are the possibilities that the energy dissipation reflected other properties of GO and HOPG, such as wettability, surface free energy[108], and mechanical properties[109]. Further research is needed to reveal whether the second mode is sensitive to lateral interactions or not.

4.5 Summary

In this chapter, the eigenmodes of the qPlus sensor with a long probe were analyzed, and the bimodal AFM using the sensor was demonstrated.

FEM Analysis of Eigenmodes

The eigenmodes of the qPlus sensor with a long probe were analyzed by FEM.

1. The eigenmode solutions corresponding to the experimentally-obtained eigenfrequencies were obtained.

2. It was found that the tip apex oscillates laterally at the second eigenfrequency

of the qPlus sensor with a long probe.

Confirmation of Lateral Tip Oscillations

KBr(100) surface was investigated in KBr-saturated BMIM-PF_6 by bimodal AFM using a qPlus sensor with a long probe. Atomic resolution imaging is demonstrated by the first mode. By adding the excitation signal at f_2 and increasing the excitation amplitude, the imaged atoms connected in the tip oscillation direction at f_2 which indicated the lateral tip oscillations in the second mode of the qPlus sensor.

Surface property detection

GO-coated HOPG was investigated in EMIM-Tf_2N by bimodal AFM using a qPlus sensor with a long probe. In the energy dissipation in the second mode, the contrast corresponding to GO and HOPG surfaces was obtained, which indicated that the surface properties can be detected by the second mode.

Chapter 5

Theoretical Analysis of Eigenmodes of qPlus Sensor with Long Probe

5.1 Introduction

To detect the vertical and lateral forces simultaneously with bimodal AFM, it is required that the tip oscillates in the vertical and lateral directions separately in independent modes. In Chapter 4, it was experimentally confirmed that the probe apex oscillates laterally in the higher flexural mode of a qPlus sensor where a long probe was attached perpendicularly to the QTF prong. However, some issues remain to be solved. First, the determination of the spring constant and oscillation amplitude is necessary for the quantitative analysis of tip-sample interaction. The effective spring constant of the qPlus sensor with a long probe was already analyzed by FEM[52,53,55]. Some methods to calibrate the amplitude of the higher mode of the qPlus sensor with a long probe were proposed, such as scanning electron microscopy[52,53] and laser Doppler vibrometry[55,56]. Furthermore, analysis of piezoelectric sensitivity, which is the ratio of the output voltage signals to the tip oscillation amplitude, is crucial because it determines the deflection noise density, which dominates the minimum detectable force gradient in AFM[110]. Although several research groups have analyzed the piezoelectric current[53], there have been no studies analyzing piezoelectric sensitivity.

In general, FEM is a powerful method for sensor vibration mode analysis. However, it can only analyze individual sensors. Mathematical analysis based on equa-

tions of motion is more effective for sensor optimization and is also crucial in the scientific context. In previous mathematical studies on the dynamic properties of qPlus sensors[51,111,112], the probe was treated as rigid in the mathematical models. The higher eigenmodes of a qPlus sensor with a long probe, which are the coupled oscillations of the QTF prong and probe, cannot be described in these models (see Chapter 4).

In this chapter, a mathematical study on the first three eigenmodes of the qPlus sensor with a long probe considering the deformation of the probe is shown. The eigenfrequencies, the tip oscillation angles, the effective spring constants, and the piezoelectric sensitivities of these modes are obtained by solving a set of equations of motion for the QTF prong and the probe. The probe length is optimized for lateral force detection in terms of piezoelectric sensitivity. The calculated eigenfrequencies and piezoelectric sensitivities are compared with the experimental results to confirm the validity of the mathematical analysis proposed here.

5.2 Theory

5.2.1 Mathematical Modeling

A photograph of a qPlus sensor is shown in Fig. 5.1a. One prong and the base of a QTF are fixed to a substrate, and an electrochemically etched tungsten needle is attached to the end of the other prong perpendicularly. In the before chapter, the probe was attached to the side of the QTF prong. Here, it is attached to its end not to cause the coupling of the torsional oscillation into flexural oscillation. This sensor design has two advantages: the direction of the lateral tip oscillation in its flexural modes is always the long axis of the QTF, and that the flexural modes of the sensor can be more simply calculated than when the flexural and torsional modes are coupled.

Preferring to the discussion in Ref. 51 (Tung *et al.*, *J. Appl. Phys.*, 2010), the eigenmodes of the qPlus sensor are analyzed by adding considerations for the probe deformation. The qPlus sensor is modeled as shown in Fig. 5.1b. L and h are the length and thickness of the QTF prong, l and d are the length and diameter of the needle, l_c is the length of the etched part of the needle, l_b is the length of the free cylindrical part of the needle, $l_b = l - h - l_c$, and L_e is the length of the electrode on the QTF prong. The physical parameters of the QTF prong and the tungsten needle

are tabulated in Table. 5.1. The QTF prong and tungsten needle are modeled as Euler-Bernoulli beams to analyze their coupled oscillation. The bonded part and etched part of the tungsten needle are modeled as a rigid cylinder and a rigid cone, respectively. Though the tungsten needle was attached to the QTF prong using epoxy glue, they are modeled as rigidly bonded.

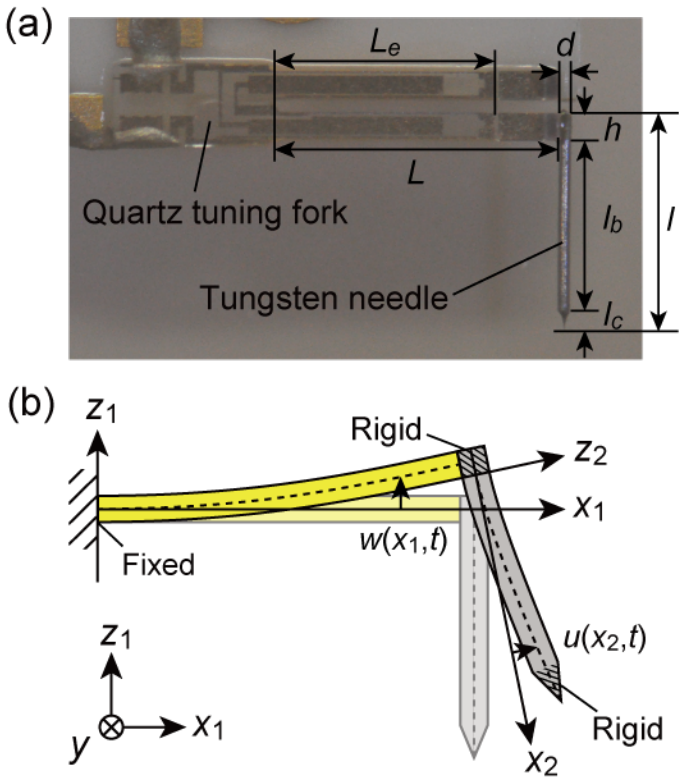

Figure 5.1: Photograph (a) and Mathematical model (b) of a qPlus sensor with a long needle. L and h are the length and thickness of the QTF prong, l and d are the length and diameter of the needle, l_c is the length of the etched part of the needle, l_b is the length of the free cylindrical part of the needle, $l_b = l - h - l_c$, L_e is the length of the electrode on the QTF prong, $w(x_1,t)$ is the bending displacement of the QTF prong, and $u(x_2,t)$ are the local displacement of the tungsten needle.

The bending displacements of the QTF prong and tungsten needle are described in the (x_1, z_1) and (x_2, z_2) coordinate systems, respectively. The bending displacement of the QTF prong at x_1 in the z_1 direction as a function of time is represented as $w(x_1,t)$, and that of the tungsten needle at x_2 in the z_2 direction is represented as $u(x_2,t)$. To simplify the expression, the point, $x_2 = 0$, is set to the lower end of the

Table 5.1: The physical parameters of the QTF prong and the tungsten needle used in the calculation. ρ_q and E_q are the mass density and Young's modulus of quartz, L, h, and b are the length, thickness, and width of the QTF prong, L_e is the length of the electrode on the QTF prong, ρ_w and E_w are the mass density and Young's modulus of tungsten, d is the diameter of the tungsten needle, and l_c the length of the etched part of the tungsten needle.

QTF prong		Tungsten needle	
ρ_q	2650 kg m^{-3}	ρ_w	19300 kg m^{-3}
E_q	80 GPa	E_w	345 GPa
L	2.357 mm	d	0.10 mm
h	0.2134 mm	l_c	0.15 mm
b	0.127 mm		
L_e	1.74 mm		

QTF prong ($z_1 = -\frac{h}{2}$ without displacements). The axial displacements and rotational inertia of two beams are assumed to be negligibly small.

5.2.2 Equations of Motion

The equations of motion for the bending motion of qPlus sensors are derived according to the mathematical model described above. The total kinetic energy T and potential energy U of a qPlus sensor are given by,

$$\begin{aligned} T = {} & \frac{1}{2}\int_0^L \rho_q A_q \left(\dot{w}(x_1,t)\right)^2 dx_1 + \frac{1}{2} M_{needle}\left(\dot{w}(L,t) + \frac{d}{2}\frac{\partial \dot{w}}{\partial x_1}(L,t)\right)^2 \\ & + \frac{1}{2} I_a \left(\frac{\partial \dot{w}}{\partial x_1}(L,t)\right)^2 + \frac{1}{2}\int_0^{l_b} \rho_w A_w \left(\dot{u}(x_2,t) + \left(x_2 + \frac{h}{2}\right)\frac{\partial \dot{w}}{\partial x_1}(L,t)\right)^2 dx_2 \\ & + \frac{1}{2} M_c \left(\dot{u}(l_b,t) + \frac{1}{4} l_c \frac{\partial \dot{u}}{\partial x_2}(l_b,t) + \left(l_b + \frac{h}{2} + \frac{1}{4} l_c\right)\frac{\partial \dot{w}}{\partial x_1}(L,t)\right)^2 + \frac{1}{2} I_c \left(\frac{\partial \dot{w}}{\partial x_1}(L,t) + \frac{\partial \dot{u}}{\partial x_2}(l_b,t)\right)^2, \end{aligned} \tag{5.1a}$$

$$U = \frac{1}{2}\int_0^L E_q I_q \left(\frac{\partial^2 w}{\partial x_1^2}(x_1,t)\right)^2 dx_1 + \frac{1}{2}\int_0^{l_b} E_w I_w \left(\frac{\partial^2 u}{\partial x_2^2}(x_2,t)\right)^2 dx_2, \tag{5.1b}$$

where ρ_x is the mass density, A_x is the cross-sectional area, E_x is the Young's modulus, and I_x is the area moment of the cross-section $(x = q, w)$. The subscripts q and w indicate that the properties are those of the QTF prong and the tungsten needle,

respectively. M_{needle} is the mass of the whole needle, $M_{needle} = \rho_w A_w \left(l - \frac{2}{3} l_c\right)$, M_c is the mass of the etched part of the needle, $M_c = \frac{1}{3}\rho_w A_w l_c$, I_a is the rotational inertia of the bonded part of the needle about y direction calculated about its center of gravity, $I_a = \rho_w A_w h \left(\frac{d^2}{16} + \frac{h^2}{12}\right)$, I_c is the rotational inertia of the etched part about y direction calculated about its center of gravity, $I_c = \frac{3}{80} M_c \left(d^2 + l_c^2\right)$. Overdots represent derivatives with respect to time. Using Eq. 5.1 along with Hamilton's principle, we obtain the equations of motion for free undamped oscillations and the relevant boundary conditions (shown in Appendix A.1). As the global displacement of the tungsten needle, $v(x_2,t) = u(x_2,t) + \left(x_2 + \frac{h}{2}\right) \frac{\partial w}{\partial x_1}(L,t)$, is induced under an assumption that the bending displacements of the beams and the gradient at the end of the QTF prong are small ($w(x_1,t), u(x_2,t) \ll h$ and $\frac{\partial w}{\partial x_1}(L,t) \ll 1$), the equations of motion are obtained in the form of

$$E_q I_q \frac{\partial^4 w}{\partial x_1^4}(x_1,t) + \rho_q A_q \ddot{w}(x_1,t) = 0, \tag{5.2a}$$

$$E_w I_w \frac{\partial^4 v}{\partial x_2^4}(x_2,t) + \rho_w A_w \ddot{v}(x_2,t) = 0, \tag{5.2b}$$

and the boundary conditions for the QTF prong are given by,

$$w(0,t) = 0, \tag{5.3a}$$

$$\frac{\partial w}{\partial x_1}(0,t) = 0, \tag{5.3b}$$

$$E_q I_q \frac{\partial^3 w}{\partial x_1^3}(L,t) - M_{needle}\left(\ddot{w}(L,t) + \frac{d}{2}\frac{\partial \ddot{w}}{\partial x_1}(L,t)\right) = 0, \tag{5.3c}$$

$$\begin{aligned} -E_q I_q \frac{\partial^2 w}{\partial x_1^2}(L,t) - \frac{d}{2} M_{needle}\left(\ddot{w}(L,t) + \frac{d}{2}\frac{\partial \ddot{w}}{\partial x_1}(L,t)\right) + \int_0^{l_b} -\rho_w A_w \left(x_2 + \frac{h}{2}\right) \ddot{v}(x_2,t)\, dx_2 \\ -I_a \frac{\partial \ddot{w}}{\partial x_1}(L,t) - I_c \frac{\partial \ddot{v}}{\partial x_2}(l_b,t) - \left(l_b + \frac{h}{2} + \frac{1}{4} l_c\right) M_c \left(\ddot{v}(l_b,t) + \frac{1}{4} l_c \frac{\partial \ddot{v}}{\partial x_2}(l_b,t)\right) = 0, \end{aligned} \tag{5.3d}$$

and the boundary conditions for the tungsten needle are given by,

$$v(0,t) = \frac{h}{2}\frac{\partial w}{\partial x_1}(L,t), \tag{5.4a}$$

$$\frac{\partial v}{\partial x_2}(0,t) = \frac{\partial w}{\partial x_1}(L,t), \tag{5.4b}$$

$$E_w I_w \frac{\partial^3 v}{\partial x_2^3}(l_b,t) - M_c\left(\ddot{v}(l_b,t) + \frac{1}{4}l_c\frac{\partial \ddot{v}}{\partial x_2}(l_b,t)\right) = 0, \tag{5.4c}$$

$$-E_w I_w \frac{\partial^2 v}{\partial x_2^2}(l_b,t) - \frac{1}{4}M_c\left(\ddot{v}(l_b,t) + \frac{1}{4}l_c\frac{\partial \ddot{v}}{\partial x_2}(l_b,t)\right) - I_c\left(\frac{\partial \ddot{v}}{\partial x_2}(l_b,t)\right) = 0. \tag{5.4d}$$

Using the method of separation of variables, the solutions of the displacements of the QTF prong and tungsten needle are assumed as

$$w(x_1,t) = \exp(i\omega t)\Phi(x_1)$$

and

$$v(x_2,t) = \exp(i\omega t)\Psi(x_2),$$

where $\exp(i\omega t)$ is the temporal component of the solution with an angular frequency ω, and $\Phi(x_1)$ and $\Psi(x_2)$ are the spatial components of the solution. By substituting the solutions of the displacements into Eq. 5.2 and eliminating the temporal component, the equations of the spatial components are given below:

$$\frac{\partial^4 \Phi}{\partial x_1^4}(x_1) = \frac{\omega^2 \rho_q A_q}{E_q I_q}\Phi(x_1), \tag{5.5a}$$

$$\frac{\partial^4 \Psi}{\partial x_2^4}(x_2) = \frac{\omega^2 \rho_w A_w}{E_w I_w}\Psi(x_2). \tag{5.5b}$$

Then, the general solutions of $\Phi(x_1)$ and $\Psi(x_2)$ are given by,

$$\begin{aligned}\Phi(x_1) &= C_1\sin(\alpha x_1) + C_2\cos(\alpha x_1) + C_3\sinh(\alpha x_1) + C_4\cosh(\alpha x_1),\\ \alpha &= \sqrt[4]{\frac{\omega^2\rho_q A_q}{E_q I_q}},\end{aligned} \tag{5.6a}$$

$$\Psi(x_2) = D_1 \sin(\beta x_2) + D_2 \cos(\beta x_2) + D_3 \sinh(\beta x_2) + D_4 \cosh(\beta x_2),$$
$$\beta = \sqrt[4]{\frac{\omega^2 \rho_w A_w}{E_w I_w}}. \tag{5.6b}$$

The boundary conditions Eqs. 5.3a and 5.3b lead $C_4 = -C_2$ and $C_3 = -C_1$. Substituting Eq. 5.6 for the remaining boundary conditions, we obtain a 6×6 matrix equation,

$$\begin{pmatrix} M_{11} & M_{12} & \dots & M_{16} \\ M_{21} & M_{22} & \dots & M_{26} \\ \vdots & \vdots & \ddots & \vdots \\ M_{61} & M_{62} & \dots & M_{66} \end{pmatrix} \begin{pmatrix} C_1 \\ C_2 \\ D_1 \\ D_2 \\ D_3 \\ D_4 \end{pmatrix} = \mathbf{0}. \tag{5.7}$$

The elements of the matrix $[M]$ in Eq. 5.7 are shown in Appendix A.2, All of the matrix elements M_{ij} are functions of α and β, which can be represented only by functions of the angular frequency ω according to Eq. 5.6. For a non-trivial solution to exist, the determinant of the coefficient matrix in Eq. 5.7 should be equal to zero. The countably infinite solutions for ω derived from the equation,

$$\det M = 0. \tag{5.8}$$

Though it is very difficult to obtain an explicit formula for the roots of Eq. 5.8, it is easy to find the roots by examining the zero crossings of the plot of the left-hand term of the equation with respect to ω. The roots of Eq. 5.8 correspond to the eigenfrequencies of the qPlus sensor, $f_i = \omega_i / 2\pi \, (i = 1, 2, 3...)$. The shape of the eigenmode was determined via Eq. 5.6 with the coefficients corresponding to the eigenfrequency, $C_1 \cdots D_4$, derived from Eq. 5.7.

5.3 Analysis of Eigenmodes

5.3.1 Probe Length Dependence of Sensor Characteristics

In this section, the probe length dependence on sensor characteristics of qPlus sensors is analyzed based on the theory described in the previous section. The first, second, and third eigenfrequencies are obtained with the help of mathematical software (Maple^{TM}), varying the probe length (1.36 mm $\leq l \leq$ 2.0 mm) with the physical parameters shown in Table 5.1. The sensor characteristics are calculated for the probe length longer than 1.36 mm because Eq. 5.2b holds for the condition that the length of the cylindrical part of the tungsten needle l_b is enough longer than the diameter $d(l_b/d \geq 10)$.

Eigenfrequency

Figure 5.2 shows the calculated first three eigenfrequencies. As increasing the probe length from 1.36 mm to 2.0 mm, the first, second, and third eigenfrequencies (f_1, f_2, and f_3) monotonically decrease from 13 kHz to 10 kHz, from 45 kHz to 20 kHz, and from160 kHz to 100 kHz, respectively. f_2 and f_3 are 2-3 times and 10-13 times higher than f_1, respectively. That is different from those of a simple cantilever-shape oscillator, $f_2 = 6.27 f_1$ and $f_3 = 17.6 f_1$ [113].

Note that the mode called "second mode" in Chapter 4 was detected at 160.8 kHz, which was the second lowest resonance peak in the thermal noise density spectrum. According to these calculation results, it should be called "third mode" actually. It seems that the piezoelectric sensitivity of the *true* second mode of the sensor was too low to be detected. The piezoelectric sensitivity of the eigenmodes is discussed later.

Shape of Eigenmode

Figure 5.3 shows the displacement of the center lines of the QTF prong and tungsten needle of the qPlus sensors at the first, second, and third eigenfrequencies with the

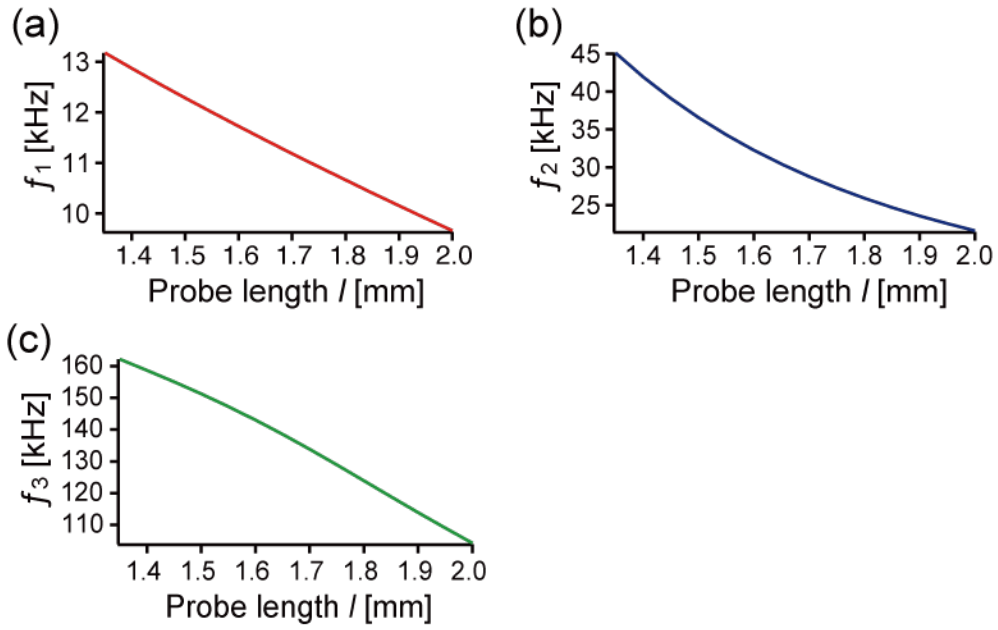

Figure 5.2: The first three eigenfrequencies calculated by using the properties listed in Table 5.1 while varying the probe length. (a) The first eigenfrequency, f_1. (b) The second eigenfrequency, f_2. (c) The third eigenfrequency, f_3.

probe length of 1.4, 1.7, and 2.0 mm, and those of the QTF prong without the needle (no probe) for comparison. The first eigenmodes are normalized with the vertical displacement of the tip (the apex of the tungsten needle), $A_v = \Phi(L) + \frac{d}{2}\frac{\partial \Phi}{\partial x_1}(L)$. The second and third eigenmodes are normalized with the lateral displacement of the tip, $A_l = \Psi(l_b) + l_c \frac{\partial \Psi}{\partial x_2}(l_b)$. To clarify the shape of the eigenmodes, the displacements of the QTF prong and tungsten needle are exaggerated in Fig. 5.3 as on the order of 0.1 mm (typically 0.1-1.0 nm in dynamic AFM). The calculated eigenmode shapes agreed with the finite element simulation results shown in Fig. 5.4, The simulation was carried out with the physical parameters listed in Table 4.1 using 3D CAD software (FreeCAD), same as described in Sec. 4.2.

It is clear from Fig. 5.3a that the displacement of the QTF prong in the first eigenmode is barely affected by the probe length. In addition, the tungsten needle scarcely deforms in the first eigenmode shown in Fig. 5.3a, which explains why

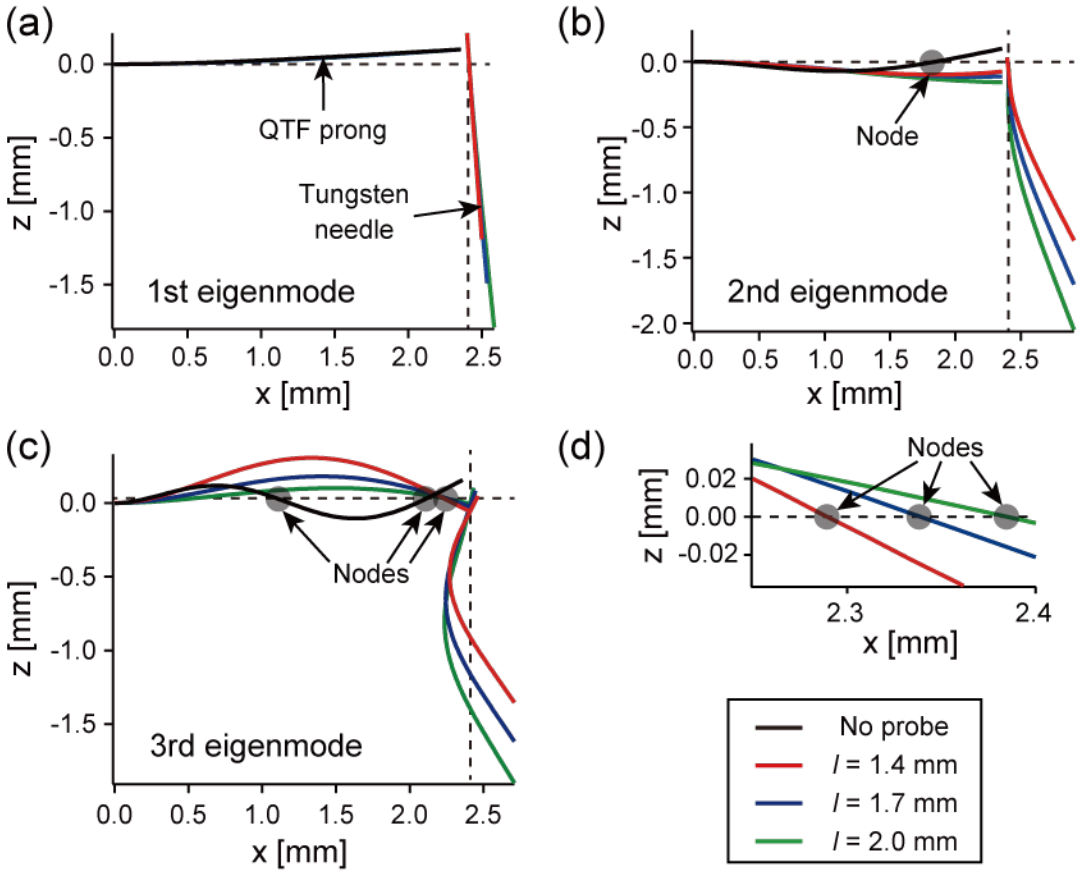

Figure 5.3: The shapes of the first three eigenmodes of the qPlus sensors, corresponding to Φ_i and Ψ_i, calculated by using the properties listed in Table 5.1 for varying the probe length ($l = 1.4$ mm (red lines), 1.7 mm (blue lines) and 2.0 mm (green lines)). The black lines show the eigenmodes of the QTF prong without the probe (no probe) for comparison. (a) The first eigenmode. (b) The second eigenmode. (c) The third eigenmode. (d) The third eigenmode expanded around its node in the QTF prong. The node shifts toward the end of the QTF prong as increasing the probe length.

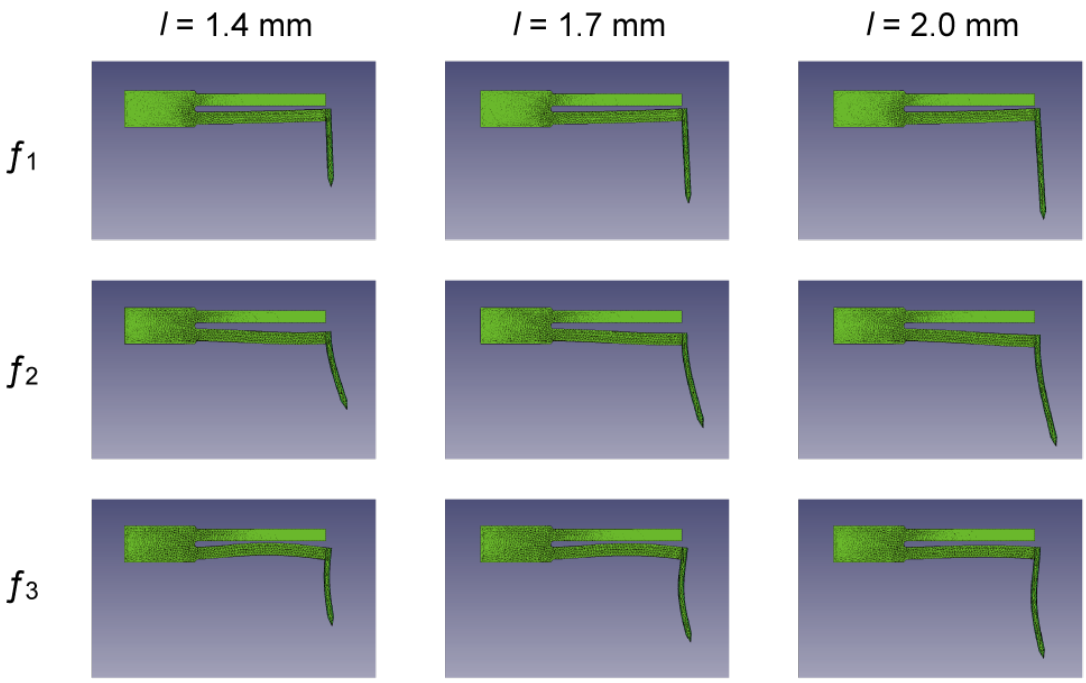

Figure 5.4: The finite element simulation results of the first, second, and third eigenmodes of the qPlus sensors with the probe length of 1.4, 1.7, and 2.0 mm.

the first eigenmode can be calculated accurately by the previously reported theories treating the probe as rigid[51,111,112]. Figures 5.3b and c show that the second and third modes are greatly affected by the probe length. Although the second mode of the sensor without the probe has a node, those of the sensors with the long probe are nodeless. The third mode of the sensor without the probe has two nodes. On the other hand, the sensor with a probe length of 1.4 mm has only one node. The node shifts toward the end of the QTF prong ($+x$ direction) as the probe length increases from 1.4 mm to 2.0 mm. These results agree with the previous report that the node in the higher eigenmode of the qPlus sensor shifts toward the end of the QTF prong as increasing the probe length[51]. As the node approaches the end of the QTF prong, the tip oscillation amplitude in the vertical direction decreases.

Tip Oscillation Angle

The tip oscillation angles in each eigenmode are calculated from the vertical and lateral displacements of the tip, $\theta_i = \arctan|A_v/A_l|$ (Fig. 5.5a). Although the trajectory of the tip oscillation is in an arc shape, it can be regarded as linear when the amplitude is sufficiently small.

Figure 5.5b shows the tip oscillation angle from the lateral direction of the first three eigenmodes. The tip oscillation angle of the first mode θ_1 is relatively close to 90° (normal to the surface) and decreases as increasing the probe length. In the first eigenmode, the displacement of the QTF prong is barely affected by the probe lengths, and the tungsten needle barely deforms (see Fig. 5.3a). Therefore, A_l increases, and θ_1 decreases as the probe length increases. The tip oscillation angles of the second and third modes, θ_2 and θ_3, are relatively close to 0° (parallel to the surface). As increasing the probe length, θ_2 increases, and θ_3 decreases. That is because of the variation of those modes of qPlus sensors, especially the position of the node of the QTF prong described above (also see Fig. 5.3b-d).

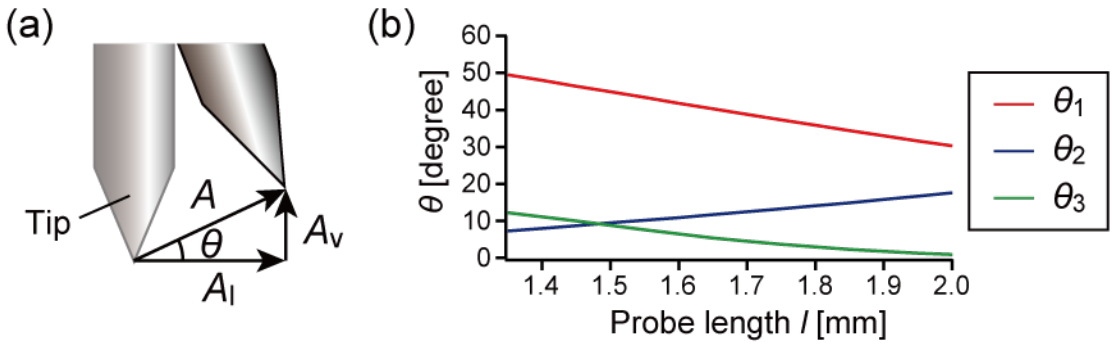

Figure 5.5: The tip oscillation angle of the first (red), second (blue) and third (green) eigenmodes, $\theta_i = \arctan|A_v/A_l|$, for the properties listed in Table 5.1 while varying the probe length. θ_1 is relatively close to 90° (normal to the surface). θ_2 and θ_3 are relatively close to 0° (parallel to the surface).

Effective spring constant

The tip motion in dynamic AFM can be described by a point-mass oscillator model[114,115]. We calculated the effective spring constant of the ith eigenmode k_i by equating the strain energy stored in the sensor, $U = \frac{1}{2}\int_0^L E_q I_q \left(\frac{\partial^2 \Phi_i}{\partial x_1^2}\right)^2 dx_1 + \frac{1}{2}\int_0^{l_b} E_w I_w \left(\frac{\partial^2 \Psi_i}{\partial x_2^2}\right)^2 dx_2$, to the potential energy of a point-mass oscillator, $U = \frac{1}{2}k_i A^2$, where A is the maximum displacement of the tip, $A = \sqrt{A_v^2 + A_l^2}$. The effective spring constant in the vertical and lateral directions can be described as $k_{i,v} = k_i \sin^{-2}\theta_i$ and $k_{i,l} = k_i \cos^{-2}\theta_i$, respectively[112].

Figure 5.6 shows the probe length dependence of $k_{1,v}$, $k_{2,l}$, and $k_{3,l}$, which are the effective spring constants in its main oscillation direction. $k_{1,v}$ varies little with the probe length at 1.9 kN m^{-1}, which agrees with the previous theoretical studies[51,111]. $k_{2,l}$ and $k_{3,l}$ decrease as increasing the probe length. $k_{2,l}$ is in the same order of magnitude as $k_{1,v}$, and $k_{3,l}$ is 10-100 times higher than $k_{1,v}$.

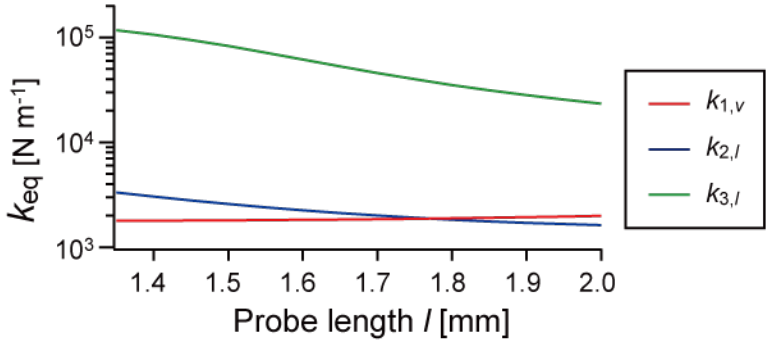

Figure 5.6: Effective spring constants calculated by equating the strain energy stored in the sensor to the potential energy of a point-mass oscillator for the properties listed in Table 5.1 while varying the probe length. The effective spring constant in the vertical direction of the first mode, $k_{1,v}$ (red line), the lateral direction of the second mode, $k_{2,l}$ (blue line), and the lateral direction of the third mode, $k_{3,l}$ (green line).

Piezoelectric sensitivity

The qPlus sensors utilize the piezoelectric effect to convert the tip oscillation to electric signals. The piezoelectric sensitivity of qPlus sensors is dramatically affected

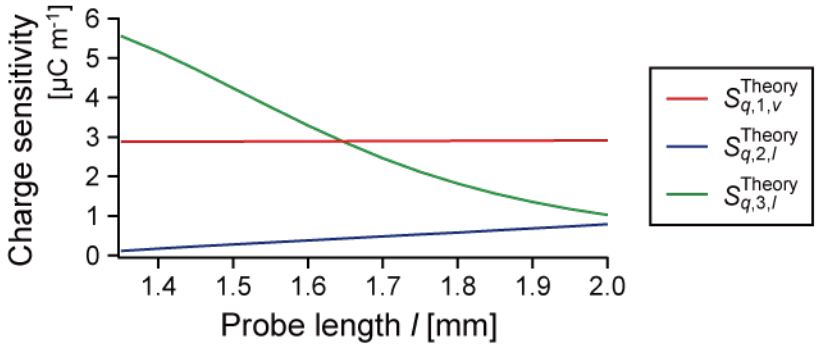

Figure 5.7: Piezoelectric charge sensitivities, the relation between the oscillation amplitude and the generated charge $S_q = Q/A$, calculated for the properties listed in Table 5.1 while varying the probe length. The calculated charge sensitivity of the vertical oscillation of the first mode, $S_{q,1,v}^{Theory}$ (red line), the lateral oscillation of the second mode, $S_{q,2,l}^{Theory}$ (blue line), and the lateral oscillation of the third mode, $S_{q,3,l}^{Theory}$ (green line).

by the shape of the eigenmode[51]. The piezoelectric charge, $Q = Q_0 T(t)$, is generated on the top and bottom electrodes by the tip oscillation, where Q_0 is the maximum charge in one oscillation cycle, and $T(t)$ is the temporal component. Q_0 is given by[51],

$$\begin{aligned} Q_0 &= -hE_q d_{31} \int_0^L \int_0^b \frac{\partial^2 \Phi(x_1)}{\partial x_1^2} dy dx_1 \\ &= -bhE_q d_{31} \frac{\partial \Phi(L_e)}{\partial x_1}, \end{aligned} \tag{5.9}$$

where d_{31} is the piezoelectric coupling coefficient, $d_{31} = 2.31$ pC m^{-1}. Young's modulus and sensor geometry are shown in Table 5.1. The gradient of the QTF prong at the end of the electrode $\partial\Phi(L_e)/\partial x_1$ is obtained from the calculated eigenmode shape. The charge sensitivity of the qPlus sensor S_q, that is, the relation between the oscillation amplitude A and the maximum generated charge Q_0, is given by $S_q = Q_0/A$.

Figure 5.7 shows the calculated charge sensitivities, $S_{q,1,v}^{Theory}$, $S_{q,2,l}^{Theory}$, and $S_{q,3,l}^{Theory}$, which are the sensitivity of the first three eigenmodes in their main oscillation direc-

tion. $S_{q,1,v}^{Theory}$ is kept almost constant at 2.9 μC m^{-1} while varying the probe length because the shape of the eigenmode barely changes (see Fig. 5.3a). $S_{q,2,l}^{Theory}$ increases from 0.1 μC m^{-1} to 0.8 μC m^{-1} as the probe length increases. It is much lower than $S_{q,1,v}^{Theory}$, which corresponds to the gradient of the QTF prong at the end of the electrode $\partial\Phi(L_e)/\partial x_1$ is close to 0 (see Fig.5.3b). $S_{q,3,l}^{Theory}$ decreases from 5.5 μC m^{-1} to 1.0 μC m^{-1} as the probe length increases. It is, however, higher than $S_{q,1,v}^{Theory}$ when the probe length is shorter than 1.65 mm.

5.3.2 Discussion

In this section, the characteristics of the eigenmodes of the qPlus sensor are analyzed by considering the deformation of the probe. The probe barely deforms in the first mode, and the mode shape of the QTF prong is less affected by the probe length. The second and third modes are coupled oscillations of the QTF prong and tungsten needle, and the mode shapes are greatly affected by the probe length.

Coupled Oscillation of QTF Prong and Probe

The spring constant of the QTF prong and the cylindrical part of the tungsten needle, calculated by $3E_qI_q/L^3$ and $3E_wI_w/l_b^3$, are 1.9 kN m^{-1} and 1.2-5.1 kN m^{-1}, respectively. The fundamental eigenfrequencies of the QTF prong and the cylindrical part of the tungsten needle calculated from their shapes and physical parameters are 34 kHz and 22-59 kHz, respectively. Thus, the qPlus sensor with the long tungsten needle can be regarded as the two cantilevers with similar spring constants and eigenfrequencies, perpendicularly connected at the one's free and the other's fixed ends. The first mode of the coupled oscillation system is the first mode of the QTF prong, whose eigenfrequency is decreased by the mass and rotational inertia of the tungsten needle. In the second mode, the first mode of the tungsten needle is coupled with the fundamental mode of the QTF prong, in which the free end is weakly constrained. The third mode is considered to be the coupled oscillation of the second mode of the QTF prong and tungsten needle. Although the tip apex oscillates

laterally in the second mode, the deflection of the QTF prong is small, and the gradient of the QTF prong at the end of the electrode is almost 0. Thus, the piezoelectric sensitivity of the second mode is low. In contrast, in the third mode, the QTF prong deforms, and the gradient of the QTF prong at the end of the electrode is large. Thus, the piezoelectric sensitivity of the third mode is high.

Detection of Vertical and Lateral Forces

The third mode is more suitable for lateral force detection because the sensitivity of the third mode is expected to be much higher than that of the second mode. In dynamic LFM, the tip oscillation angle should be parallel to the surface to suppress the crosstalk of the vertical force components. However, as the probe length is increased, θ_3 approaches 0°, and $S_{q,3,l}^{Theory}$ decreases. That is, there is a trade-off between the piezoelectric sensitivity and the crosstalk of the vertical force component in the third mode. The probe length of 1.6-1.7 mm is suitable for the vertical and lateral force detection where $S_{q,3,l}^{Theory}$ is in the same magnitude as $S_{q,1,v}^{Theory}$. In this case, the crosstalk of the vertical force component in the third mode is less than 2 percent.

5.4 Comparison between Theory and Experimental Results

5.4.1 Experimental

In this section, the eigenfrequencies and piezoelectric sensitivities of qPlus sensors with various probe lengths were experimentally obtained and compared with the theoretical values. The thermal oscillation analysis was carried out on the qPlus sensor with a long probe to obtain the piezoelectric sensitivities of the qPlus sensors.

Sensor Fabrication

The qPlus sensors were fabricated to measure their eigenfrequencies and piezoelectric sensitivities experimentally. One prong and the base of the QTF (STATEK Co.,

TFW 1165, the geometry and physical parameters corresponding to the values listed in Table 5.1) were glued to an alumina substrate. A tungsten wire (Nilaco Co., diameter: 0.10 mm) was electrochemically etched in potassium hydroxide (1.2 mol L^{-1}) and was cut in the various probe lengths (l= 1.53 mm, 1.60 mm, 1.61 mm, 1.68 mm, 1.69 mm, and 1.75 mm, l_c=0.15 mm), and then was glued to the end of the free QTF prong by using epoxy glue (EPO-TEK H70E, Epoxy Technology, Inc.).

Current-to-Voltage Conversion Amplifier

Experimentally, the piezoelectric signal of a qPlus sensor is measured with a current-to-voltage conversion amplifier. The voltage sensitivity of the qPlus sensor is given by $S_v = V_0/A$, where V_0 is the maximum voltage output of the amplifier in one oscillation cycle. In this experiment, a differential current preamplifier[69], whose output signal is twice as large as a single transimpedance system, is used to convert the piezoelectric current of the qPlus sensor into a detectable voltage signal. The frequency response of this differential amplifier has not been thoroughly examined. However, assuming that it is similar to that of a single transimpedance amplifier, the gain of the amplifier is inversely proportional to the frequency f for frequencies higher than the corner frequency $f_c = 1/(2\pi RC)$, where R is the resistance of feedback resistor and C is its parasitic capacitance[110]. In this work, the corner frequency is given by $f_c \sim 40$ Hz for $R = 20$ GΩ and $C \sim 0.2$ pF. The gain of the amplifier G is assumed to be inversely proportional to the frequency f in the frequency range first three eigenfrequencies of the sensor (10-200 kHz), $G = V/I = G_0/f$, where G_0 is a constant of proportionality. Sinusoidally varying charge $Q = Q_0 \exp(2\pi i f t)$ is corresponding to a current $I = \dot{Q} = 2\pi i f Q_0 \exp(2\pi i f t)$. Thus, we obtain $S_v = V_0/A = 2\pi Q_0 G_0/A = 2\pi G_0 S_q$. That means the voltage sensitivity of qPlus sensor S_v in this experimental system should be linear with the calculated charge sensitivity S_q.

Thermal Noise Spectra Measurement

The qPlus sensor was set to the AFM head with the differential current amplifier, and the thermal noise spectrum was measured by a spectrum analyzer (Agilent Technologies Inc., N9000A) under an ambient condition at $T = 25$ °C. The spectra were measured around the first three eigenfrequencies of each sensor. The average number is set to 100 for the first eigenfrequency and 1000 for the second and third eigenfrequencies. The voltage sensitivity is obtained by fitting the spectra as described in Sec. 2.2.6. The spring constant calculated by the theory is substituted in the fitting function.

5.4.2 Results and Discussion

Thermal Noise Spectra

Figure 5.8 shows the optical microscopy images of the qPlus sensors with the various probe lengths, l= 1.53 mm, 1.60 mm, and 1.61 mm, and the thermal noise spectra around their first three eigenfrequencies. Note that the voltage signal shown in the spectra is 0.65 times lower than the total voltage signal since the input impedance of the spectrum analyzer is 50 Ω and the output impedance of the preamplifier, which is equal to that of OPA227, is 27 Ω. The thermal peaks of the second mode of three sensors (l = 1.53 mm, 1.60 mm, and 1.61 mm) were not detected, which would be due to the low piezoelectric sensitivity of the second mode, which corresponds well to the theoretical prediction described in Sec. 5.3.1.

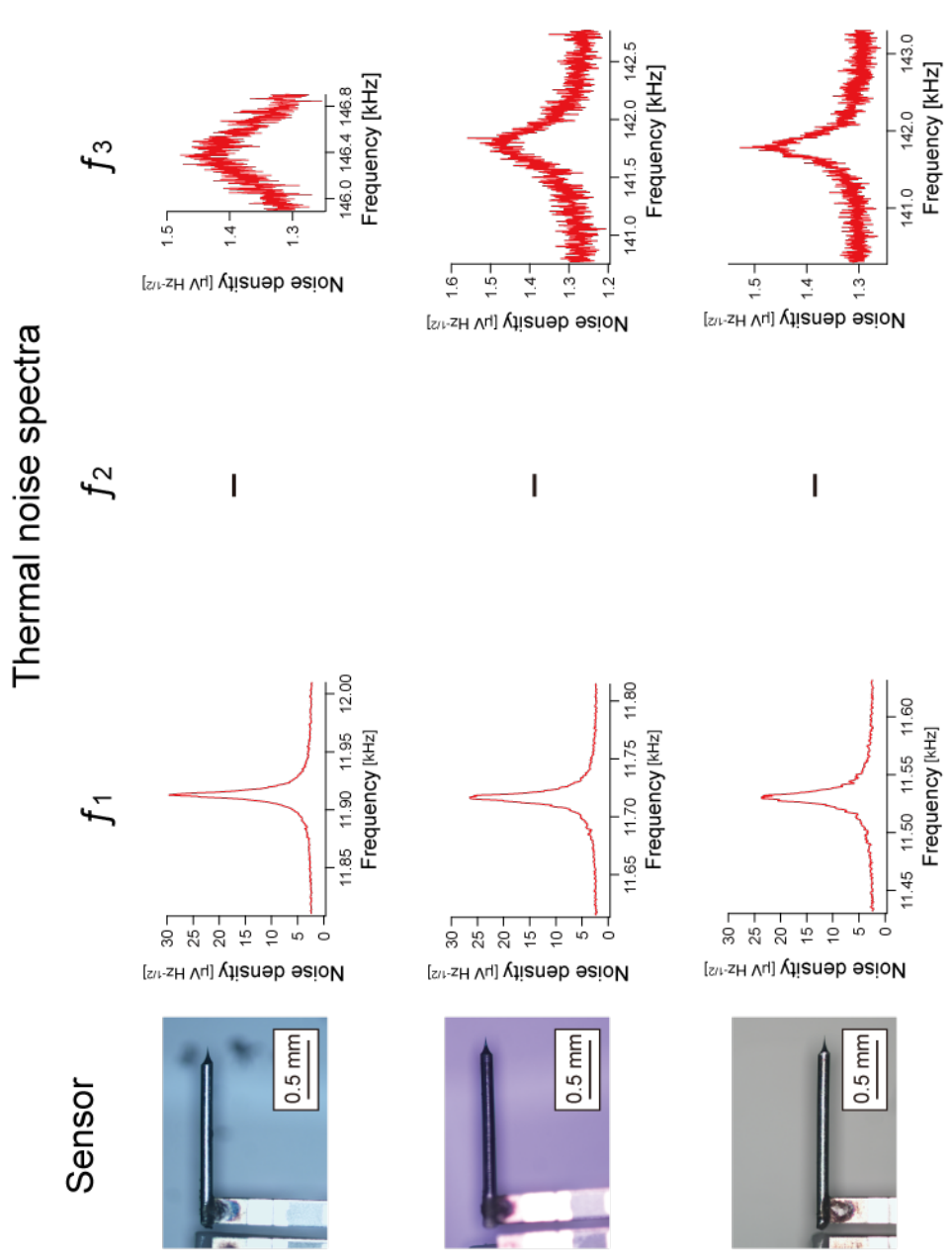

Figure 5.8: Optical microscopy images of the qPlus sensors with the various probe lengths, l = 1.53 mm, 1.60 mm, and 1.61 mm, and the thermal noise spectra around their first three eigenfrequencies.

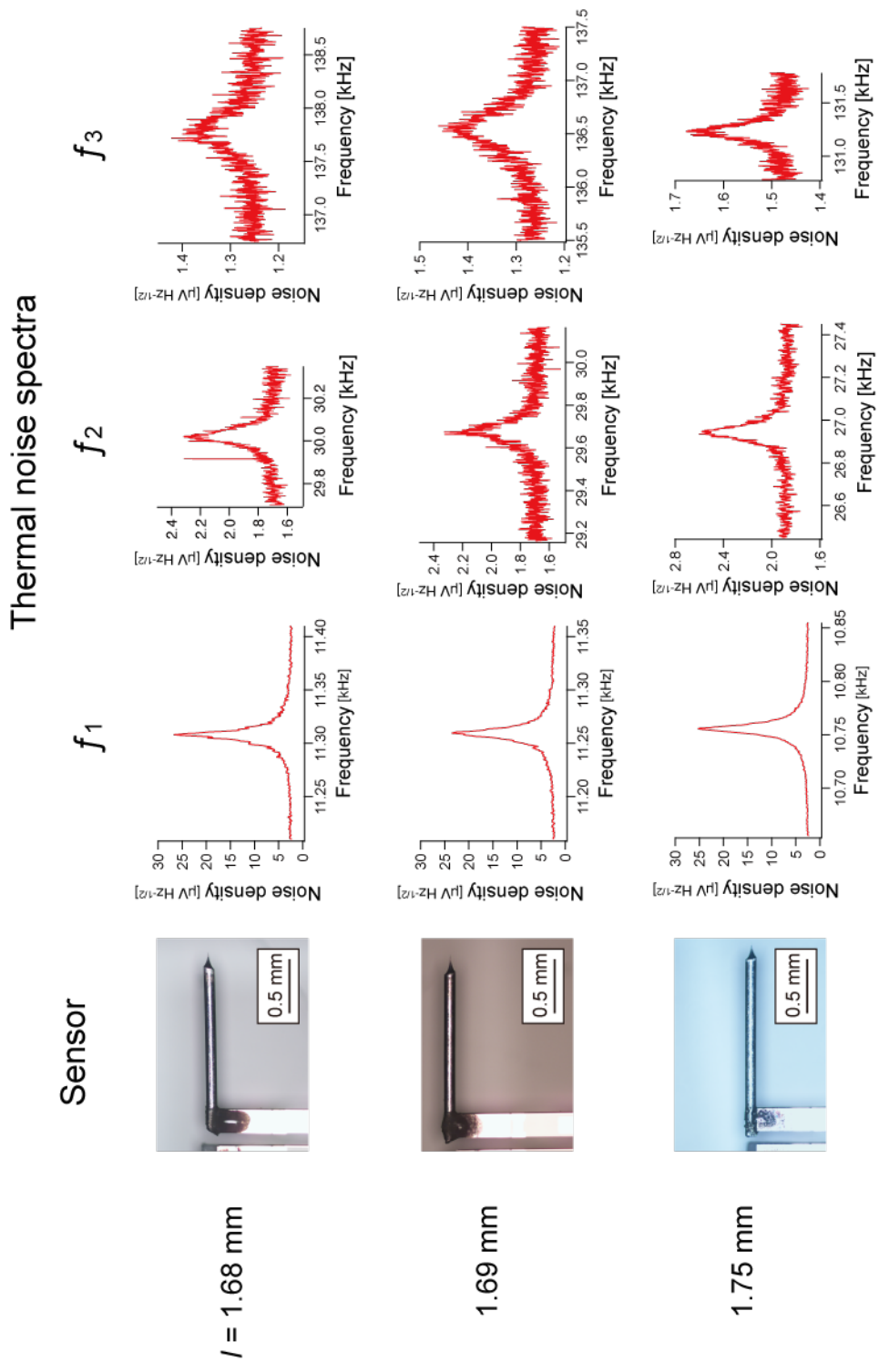

Figure 5.8: (cont.) Optical microscopy images of the qPlus sensors with the various probe lengths, l = 1.68 mm, 1.69 mm, and 1.75 mm, and the thermal noise spectra around their first three eigenfrequencies.

Eigenfrequency

Figures 5.9 a-c show the first three eigenfrequencies of the qPlus sensors. The calculated eigenfrequencies are also shown in these figures for comparison (solid lines, same data shown in Fig. 5.2). The eigenfrequencies experimentally obtained from the thermal spectra are in excellent agreement with the theoretical values (the deviation is less than 2 percent).

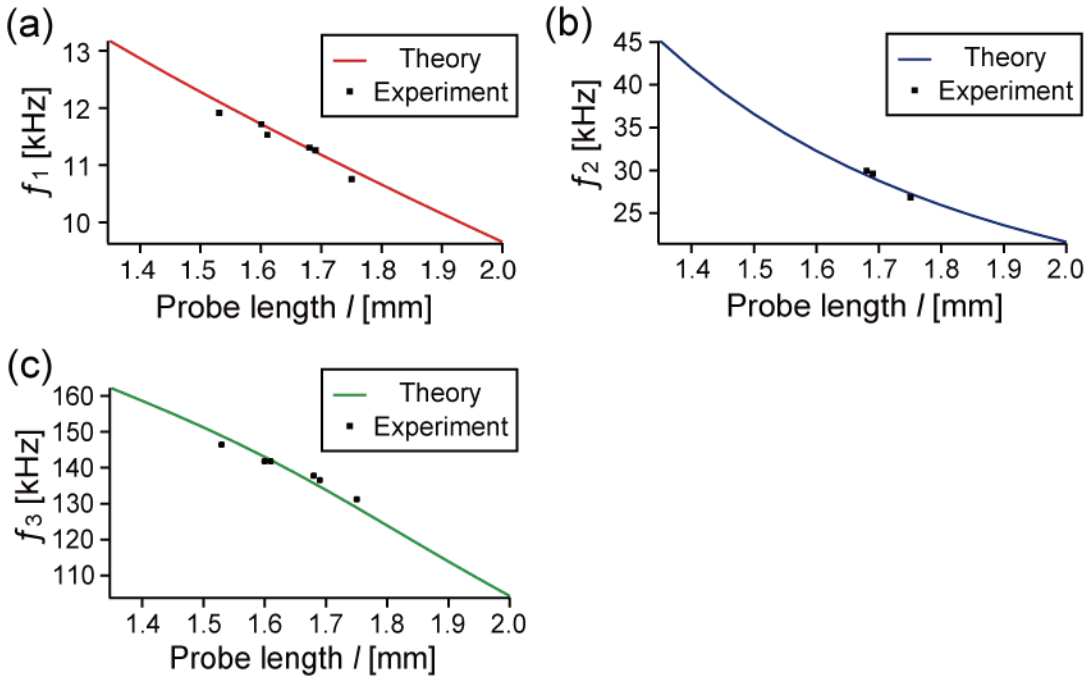

Figure 5.9: (a)-(c) Experimentally obtained first (a), second (c), and third (c) eigenfrequencies of the qPlus sensors with various probe lengths (1.53 mm, 1.60 mm, 1.61 mm, 1.68 mm, 1.69 mm, and 1.75 mm). The calculated eigenfrequencies (already shown in Fig. 5.2) are also shown for comparison (solid lines). Experimentally obtained eigenfrequencies are in good agreement with the theory.

Piezoelectric Sensitivity

Figure 5.10 shows the piezoelectric voltage sensitivities of the first three eigenmodes of the qPlus sensors experimentally obtained by their thermal noise spectra. The calculated charge sensitivities (same data shown in Fig. 5.7) are also shown in Fig.

5.10 for comparison. Note that the relationship between the vertical axes of these data is not precise; it is simply set up to facilitate a comparison of the experimental and theoretical results.

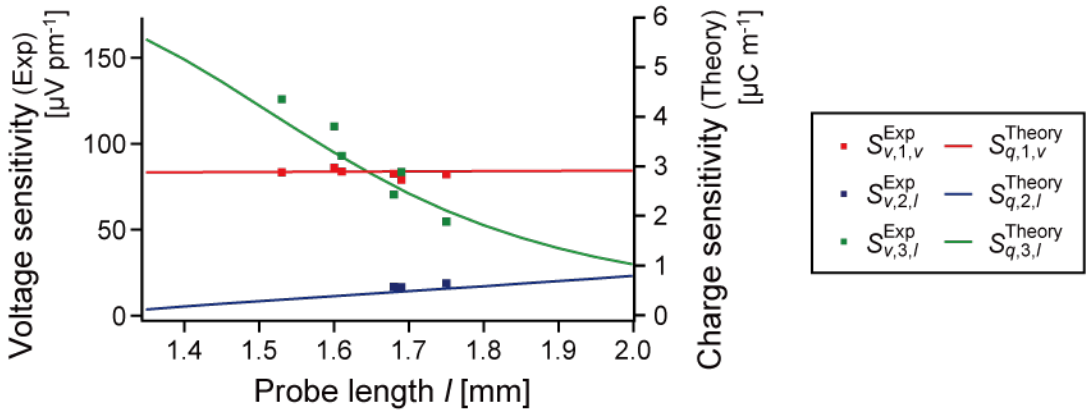

Figure 5.10: Piezoelectric voltage sensitivities, $S_v = V_0/A$, derived from the thermal spectrum of the qPlus sensors. The sensitivity of the vertical oscillation of the first mode, $S^{Exp}_{v,1,v}$ (red points), the lateral oscillation of the second mode, $S^{Exp}_{v,2,l}$ (blue points), and the lateral oscillation of the third mode, $S^{Exp}_{v,3,l}$ (green points). Piezoelectric charge sensitivities, the relation between the oscillation amplitude and the generated charge $S_q = Q/A$ (same data shown in Fig. 5.7). The calculated charge sensitivity of the vertical oscillation of the first mode, $S^{Theory}_{q,1,v}$ (red line), the lateral oscillation of the second mode, $S^{Theory}_{q,2,l}$ (blue line), and the lateral oscillation of the third mode, $S^{Theory}_{q,3,l}$ (green line). Note that the relationship between the vertical axes is simply set up to facilitate a comparison of the experimental and theoretical results.

The sensitivities of the vertical oscillation of the first mode $S^{Exp}_{v,1,v}$ of all tested sensors were $83 \pm 4\ \mu\text{V pm}^{-1}$. This result is 28 percent lower than previously reported by Huber and Giessibl ($115\ \mu\text{V pm}^{-1}$)[69]. This is probably due to the different resistance values of the feedback resistor used in the preamplifier (this study: 20 GΩ, Huber & Geissibl: 10 GΩ[69]) and the different QTFs used for qPlus sensors (this study: STATEK Co., TFW 1165, Huber & Geissibl: custom-designed QTF[110,116]). The sensitivities of the lateral oscillation of the second mode $S^{Exp}_{v,2,l}$ for three sensors (l = 1.53 mm, 1.60 mm, and 1.61 mm) were too low to be detected. Though it

increased as the probe length increased, it was still much lower than $S_{v,1,v}^{Exp}$. The sensitivity of the lateral oscillation of the third mode $S_{v,3,l}^{Exp}$ decreased as increasing the probe length. It is higher than $S_{v,1,v}^{Exp}$ for three sensors (l = 1.53 mm, 1.60 mm, and 1.61 mm) and lower than $S_{v,1,v}^{Exp}$ for two sensors (l = 1.68 mm and 1.75 mm). For the sensor with the probe length of 1.69 mm, $S_{v,1,v}^{Exp}$ and $S_{v,3,l}^{Exp}$ are similar values. This length-dependent sensitivity for the first three eigenmodes was similar to the theoretically obtained charge sensitivity S_q^{Theory}. Thus, we experimentally and theoretically confirmed that the piezoelectric sensitivity depends on the probe length, which changes the shape of the eigenmode.

5.5 Summary

In this chapter, the dynamics of the qPlus sensor with a long probe were theoretically and experimentally studied.

Theoretical Analysis of Sensor Characteristics

The first three eigenmodes of the qPlus sensor were analyzed by solving the equations of motion of the coupled oscillation of the QTF prong and probe.

1. The eigenfrequencies, eigenmode shapes, tip oscillation angles, effective spring constants, and piezoelectric sensitivities of the first three eigenmodes were successfully obtained by solving the equations of motion of the coupled motion of the QTF prong and probe.

2. The calculated first eigenmode indicates that the probe barely deforms. The probe length greatly influences the second mode and third modes, and the probe deforms in these modes.

3. The tip oscillation angle of the first mode is relatively close to the vertical direction, and those of the second and third modes are close to the lateral direction.

4. The sensitivity of the third mode is expected to be much higher than that of the second mode. The third mode is more suitable for lateral force detection in this condition analyzed here.

Comparison between Theory and Experiment

The eigenfrequency and piezoelectric sensitivity of the qPlus sensor with various probe lengths were obtained by measuring the thermal noise spectra and compared with the theoretical value.

1. The calculated eigenfrequencies were in excellent agreement with the experimentally obtained values.

2. The probe length dependence of the calculated piezoelectric sensitivities agreed with that of the sensitivities derived from thermal spectra.

These calculation results indicated that the first and third modes of the qPlus sensor with a long probe are suitable for the simultaneous detection of vertical and lateral forces.

Chapter 6

Lateral Force Detection with qPlus Sensor with Long Probe

6.1 Introduction

In Chapters 4 and 5, it was experimentally and theoretically shown that the tip of the qPlus sensor with a long probe laterally oscillates in its third flexural mode. In terms of the tip oscillation angle and piezoelectric sensitivity, the first and third modes of the qPlus sensor with a long probe are suitable for detecting vertical and lateral forces. However, it was not thoroughly examined that the lateral force is detected by the third mode. To confirm that the higher modes are sensitive to lateral (in-plane) interactions, it is appropriate to analyze samples with in-plane anisotropic properties, such as friction anisotropy.

LFM studies reported friction anisotropy on polymer crystals, such as high-density polyethylene crystals[117,118] and highly-oriented poly(tetrafluoroethylene) on glasses[118]. The friction force measured perpendicularly to the polymer chains is larger than the friction force measured along the chains. Friction anisotropy was also detected on a well-crystalized poly(vinylidenefluoride-trifluoroethylene) (P(VDF-TrFE)) by lateral-modulation LFM (LM-LFM)[119].

In conventional LFM experiments, the tip is in contact with the sample surface, and the lateral force (friction force) is detected via the torsional deflection of the cantilever. Friction anisotropy caused by atomic- or molecular-scale surface structure was also detected by dynamic LFM without static contact[49,120]. L. Huang *et al.* detected friction anisotropy corresponding to the backbone orientation of a polydiacetylene single crystal by torsional resonance mode of a Si cantilever, where the tip-sample distance was regulated by keeping its amplitude constant, and the friction anisotropy was detected in the phase images[120]. A.J. Weymouth *et al.* investigated the directional dependence friction on H-terminated Si (110) in UHV, where the tip-sample distance was regulated by tunneling current, and the lateral force was detected via the frequency shift of the LFM qPlus sensor[49]. Therefore, friction anisotropy detection in our bimodal AFM setup will reveal its capability of detecting the lateral (in-plane) tip-sample interactions.

In this chapter, the P(VDF-TrFE) thin film is investigated by the bimodal AFM utilizing the qPlus sensor with a long probe to confirm that the lateral force can be detected by the third mode.

6.2 Experimental

6.2.1 Materials

Poly(vinylidenefluoride-trifluoroethylene) (P(VDF-TrFE): CH_3-$(CH_2CF_2)_n$-$(CHFCF_2)_m$-CH_3) is a copolymer of vinylidenefluoride (VDF) and trifluoroethylene (TrFE), which is a well-known ferroelectric crystalline polymer with a -C-C- main chain having spontaneous C-F dipoles. The Curie point T_c and melting point T_m of P(VDF-TrFE) depend on its molar content ratio of VDF/TrFE. The ferroelectric-to-paraelectric phase transition of P(VDF-TrFE) with the VDF ratio below 82% can be observed since its T_c is lower than its T_m. In this experiment, P(VDF-TrFE) with the VDF/TrFE molar content ratio of 75/25 is used, whose ferroelectric-to-paraelectric phase transition tem-

perature during the heating process T_{c-heat} and the paraelectric-to-ferroelectric one during the cooling process T_{c-cool} are observed at 123°C and 70°C, respectively[121]. A well-crystallized P(VDF-TrFE) film can be obtained by annealing at a temperature between T_{c-heat} and its T_m (147°C[121]), which is constructed by many randomly oriented rodlike grains. These grains are considered to be edge-on lamellae[119,122]. In its paraelectric phase, the surface roughness of edge-on lamellae of the P(VDF-TrFE) with this molar content ratio is suppressed[123], and the friction anisotropy corresponding to the molecular chain orientation in the edge-on lamellae of the P(VDF-TrFE) becomes significant[119].

6.2.2 Experimental Setup

The experiments are carried out by a system based on a commercial AFM (JEOL, JSPM-5200) with a home-built AFM head made for a qPlus sensor[44]. Figure 6.1 shows a block diagram of the bimodal AFM. The first and third eigenmodes of the sensor were simultaneously excited by using a lead zirconate titanate (PZT) piezoelectric actuator. The frequency shift of the first eigenmode Δf_1 was detected by a commercial FM demodulator (Kyoto Instruments, KI-2001) with some modifications. The oscillation amplitude of the first mode A_1 was kept constant with an automatic gain controller, and the energy dissipation in the first mode E_1 was measured via the driving amplitude. The third eigenmode was excited at a constant frequency equal to f_3 with constant driving amplitude. The amplitude and phase of the third eigenmode, A_3 and ϕ_3, were detected by a lock-in amplifier (NF Electronic Instruments, LI 5640). Such bimodal AFM operation is called frequency modulation-amplitude modulation, "FM-AM".

Topographic images were obtained by scanning the tip on the surface while Δf_1 was kept constant. E_1, A_3, and ϕ_3 images were obtained simultaneously with the topographic image. The energy dissipation in the third mode E_3 was calculated from

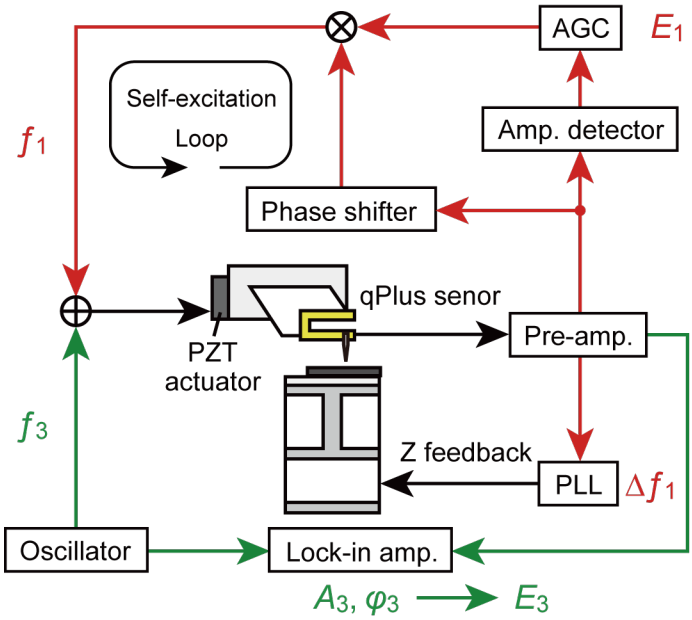

Figure 6.1: Block diagram of the FM-AM bimodal AFM setup. The sensor is simultaneously mechanically excited at f_1 and f_3. The first mode is operated by frequency modulation. The frequency shift of the first mode Δf_1 is detected by an FM demodulator and used for z-feedback. The amplitude of the first mode A_1 is kept constant, and the energy dissipation in the first mode E_1 is obtained from the driving amplitude. The third mode is excited at a constant frequency equal to f_3, with a constant driving amplitude. The amplitude and phase of the third mode (A_3 and ϕ_3) are detected by a lock-in amplifier. The energy dissipation in the third mode E_3 is derived from A_3 and ϕ_3.

A_3 and ϕ_3 as

$$E_3 = \frac{\pi k_3 A_3 f_3}{Q_3}\left(\frac{A_{3,0}}{A_3}\sin(-\phi_3) - 1\right), \tag{6.1}$$

where k_3 is the spring constant, and Q_3 is the quality factor of the third mode. $A_{3,0}$ is the amplitude of the third mode without any tip-sample interactions.

The interaction stiffness in the third mode $k_{int,3}$ was also derived from A_3 and ϕ_3 as[74]

$$k_{int,3} = \frac{k_3 A_{3,0}}{Q_3 A_3}\cos(-\phi_3). \tag{6.2}$$

6.2.3 Sample Preparation

A schematic of the sample preparation process is shown in Fig. 6.2. P(VDF-TrFE) with a VDF/TrFE molar content ratio of 75:25 was provided by Daikin Industries Ltd and used as received. A P(VDF-TrFE) film was obtained by spin-coating 2 wt% P(VDF-TrFE)-methylethylketone solution on a freshly cleaved HOPG (SPI supplies, SPI-2 Grade). The film was annealed for 2 h to improve its crystallinity at 145°C and cooled naturally to room temperature under ambient conditions. After crystallization, the film surface was investigated by bimodal AFM using a qPlus sensor. The P(VDF-TrFE) crystal shows highly-regulated molecular orientation above T_{c-heat} (paraelectric phase), whose friction force was detected uniformly inside each crystal[119]. The sample temperature during the AFM measurement was kept at 125°C, slightly above T_{c-heat} of the P(VDF-TrFE) used in this study, to clarify the friction difference between differently oriented crystals. The sample was heated by using a ceramic heater (Sakaguchi E.H Voc Corp., MC1020) equipped on the sample holder with a direct current to avoid the noise increase in the signal of the qPlus sensor.

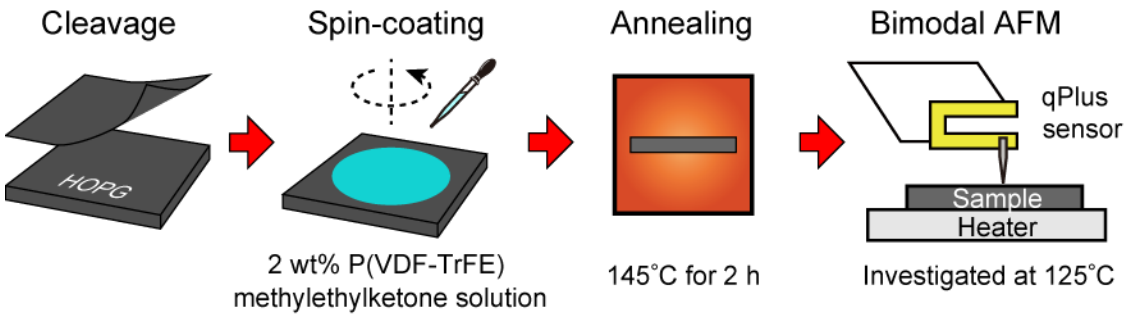

Figure 6.2: Schematic illustration of the preparation process of the well-crystallized P(VDF-TrFE) thin film on HOPG.

6.3 Friction Anisotropy Detection with Bimodal AFM

6.3.1 Sensor Characterization

The probe length l and the etched part length l_c of the qPlus sensor used in this experiment were 1.61 mm and 0.17 mm, respectively. The first three eigenfrequencies confirmed by mechanically forced excitation at 25°C were 11.6 kHz (f_1), 32.9 kHz (f_2), and 142.8 kHz (f_3). They are in good agreement with eigenfrequencies calculated by the theory described in Sec. 5.2, of 11.7 kHz, 32.4 kHz, and 143.2 kHz. The calculated tip oscillation angles were 41.7°, 10.8°, and 6.3° for f_1, f_2, and f_3, respectively. The first and third modes were used to detect vertical and lateral forces in the bimodal AFM experiment.

The thermal spectra and transfer functions around f_1 and f_3 of the sensor were measured to analyze the sensor characteristics. Figures 6.3 a and b show thermal noise spectra of the qPlus sensor used in the experiment around its f_1 and f_3 obtained at the sample temperature of 25°C and 125°C. The temperature of the qPlus sensor was not certainly known when the sample temperature was 125°C because the sensor was not in contact with the heater but was mildly heated. Both eigenfrequencies are slightly negatively shifted at the sample temperature of 125°C because the eigenfrequency of QTFs varies with temperature as an inverted parabola centered around 25°C[124,125]. The sensitivities of the first and third modes were determined from the thermal noise spectra obtained at 25°C. The voltage sensitivities, $S_{v,1,v}$ and $S_{v,3,l}$, obtained from the thermal noise spectra were 84.4 μV pm^{-1} and 110 μV pm^{-1}, respectively. Figures 6.3 c and d show the transfer functions of the qPlus sensor around f_1 and f_3 at the sample temperature of 125°C. There is no "forest of peaks" in the amplitude components of the transfer functions, which can cause instrumental artifacts in the detected signals.

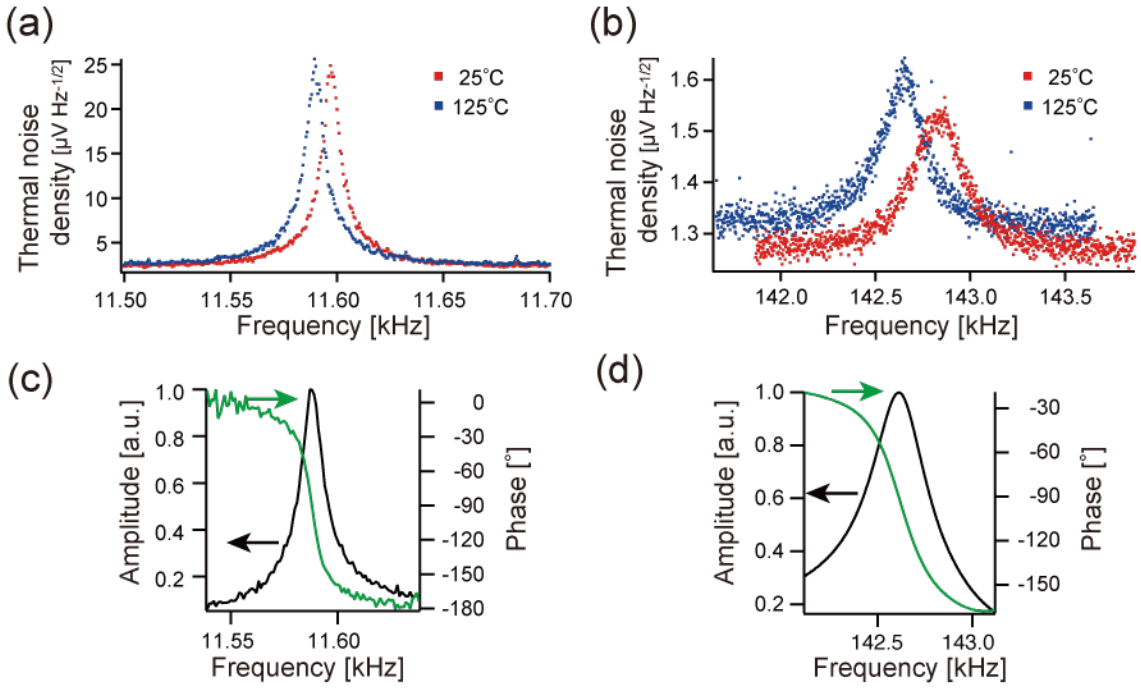

Figure 6.3: Thermal noise spectra around the first eigenfrequency (a) and third eigenfrequency (b) of the qPlus sensor used in this experiment ($l = 1.61$ mm, $l_c = 0.17$ mm). The spectra were taken at the sample temperature of 25°C (red points) and 125°C (blue points). Transfer functions of the first mode (c) and third mode (d) of the qPlus sensor measured at the sample temperature of 125°C. The black and green lines show the normalized amplitude and phase of the qPlus sensor.

6.3.2 Friction Anisotropy Detection on P(VDF-TrFE) Thin Films

The bimodal AFM images obtained on the P(VDF-TrFE) film at the sample temperature of 125 °C are shown in Fig. 6.4. The probe oscillated laterally in the y direction at f_3 as indicated by the arrow in Fig. 6.4a. In the topographic image shown in Fig. 6.4b, randomly oriented rodlike grains are recognized. This feature indicates that they were the edge-on lamellae of P(VDF-TrFE)[119]. In edge-on lamellae, the molecular chains align parallel to the film surface and perpendicular to the lamellar plane, the direction of the short axis of the grains, with folds as illustrated in Fig. 6.4a. Figures 6.4c and d show E_1 and E_3 images simultaneously obtained with the

topographic image shown in Fig. 6.4b. E_1 did not depend on the direction of the grains. In contrast, E_3 changed depending on the grain directions. Figure 6.4e shows the line profile of E_3 on the black lines in Fig. 6.4d. Figures 6.4d and e show that E_3 increased between the grains, which is because of the topographic effects, that the tip strongly interacts with the surface at the grain edge where the topographic slope is large, and that the tip interacts with two grains when the tip is between the grains.

Next, E_3 in the grains is discussed by considering the relation between the tip oscillation direction and the molecular orientation in the grains. The short axis of the grains 1-4 indicated in the topographic image (Fig. 6.4b) tilted 66°, 84°, -12°, and -81° from $+y$ direction, respectively. The gray-colored zones in the line profiles (Fig. 6.4e) correspond to the numbered grains. Fig. 6.4e shows $E_3^{grain1(66^\circ)} \simeq E_3^{grain2(84^\circ)} \simeq E_3^{grain4(-81^\circ)} > E_3^{grain3(-12^\circ)}$. Thus, E_3 decreased when the shorter axis of the grain was parallel to the tip oscillation direction at f_3. Namely, the dissipative tip-sample interactions detected in the third mode decreased when the tip oscillated parallel to the molecular chain orientation of the P(VDF-TrFE). In the previous LM-LFM study[119], the friction force on the P(VDF-TrFE) film was smaller when the molecular chain orientation was parallel to the lateral modulation direction. These results indicate that the friction anisotropy on the P(VDF-TrFE) was detected by this bimodal AFM and that lateral force was detected by the third mode of the qPlus sensor with a long probe.

Figure 6.5a shows the interaction stiffness in the third mode $k_{int,3}$. $k_{int,3}$ increased between the grains because of the topographic effects, which is the same as already pointed out about E_3. Figure 6.5b shows a line profile of $k_{int,3}$ on the black line in Figure 6.5 a. The gray-colored zones in the line profiles (Fig. 6.5 b) correspond to the numbered grains. The line profile indicated the relationship of $k_{int,3}$ between the numbered grains as $k_{int,3}^{grain2(84^\circ)} \simeq k_{int,3}^{grain4(-81^\circ)} > k_{int,3}^{grain1(66^\circ)} > k_{int,3}^{grain3(-12^\circ)}$. The conservative tip-sample interactions detected in the third mode $k_{int,3}$ decreased when the

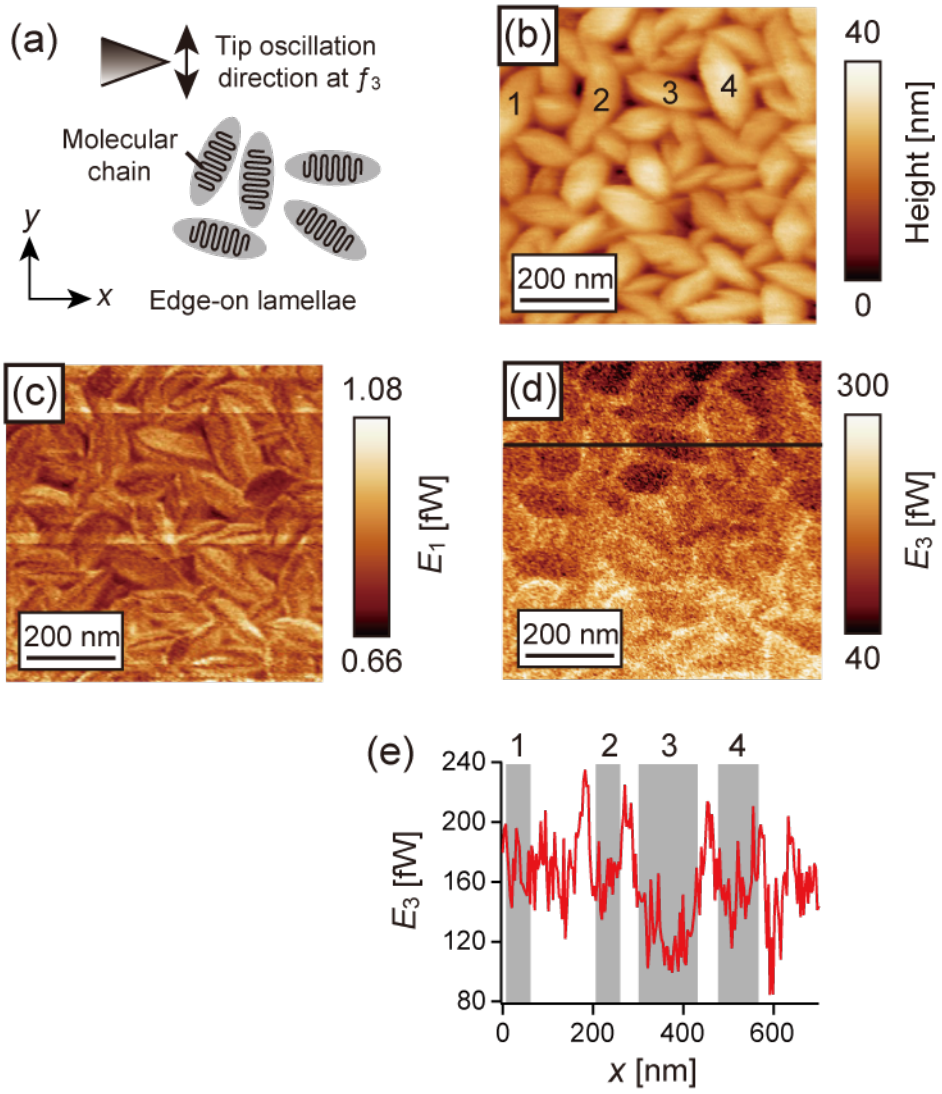

Figure 6.4: The bimodal AFM results on the P(VDF-TrFE) film obtained at 125°C under an ambient condition. (a) Schematic illustration of the P(VDF-TrFE) edge-on lamellae and tip oscillation at f_3. (b) Topography. (c) Energy dissipation in the first mode E_1. (d) Energy dissipation in the third mode E_3. (e) Line profile of E_3 on the black line in (d). The gray-colored zones in (e) correspond to the numbered grains indicated in (b). The probe length l and the etched part length l_c were 1.61 mm and 0.17 mm, respectively. $f_1 = 11.6$ kHz, $Q_1 = 1600$, $k_{1,y} = 1.9$ kN m^{-1}, $\theta_1 = 41.7°$, $A_1 = 118$ pm, $f_3 = 142.6$ kHz, $Q_3 = 550$, $k_{3,l} = 58.6$ kN m^{-1}, $\theta_3 = 6.3°$, $A_{3,0} = 386$ pm. These images were taken at $\Delta f_1 = +3.5$ Hz.

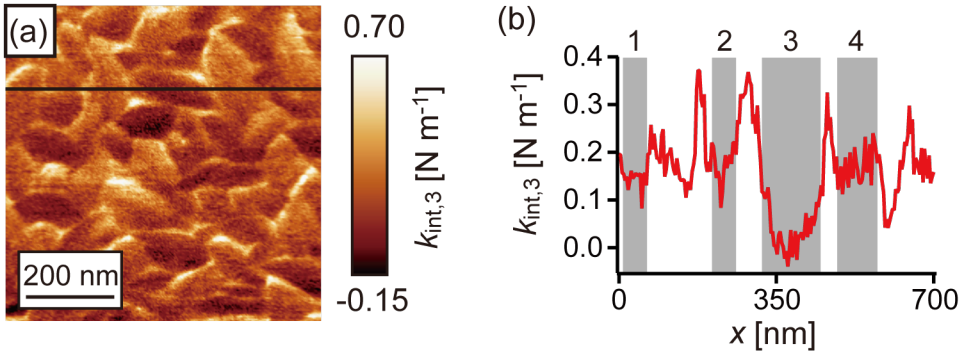

Figure 6.5: (a) Interaction stiffness in the third mode $k_{int,3}$ calculated from A_3 and ϕ_3 along with Eq. 6.2. (b) Line profile of $k_{int,3}$ on the black line in (a).

tip oscillated parallel to the molecular chain orientation of the P(VDF-TrFE); that is, the anisotropy of conservative lateral interactions on the P(VDF-TrFE) thin film was also detected.

It should noted that E_3 and $k_{int,3}$ gradually drifted in the slow scan direction (y direction) because A_3 and ϕ_3 drifted (shown in Fig. 6.6). It assumes that the sensor was being heated during the imaging, which caused the shift of the eigenfrequencies and the variation of the quality factors. It reproducibly occurs even after heating 1 h before approaching and keeping in the imaging condition for over 1 h. Thus, these data at the same y position are discussed above.

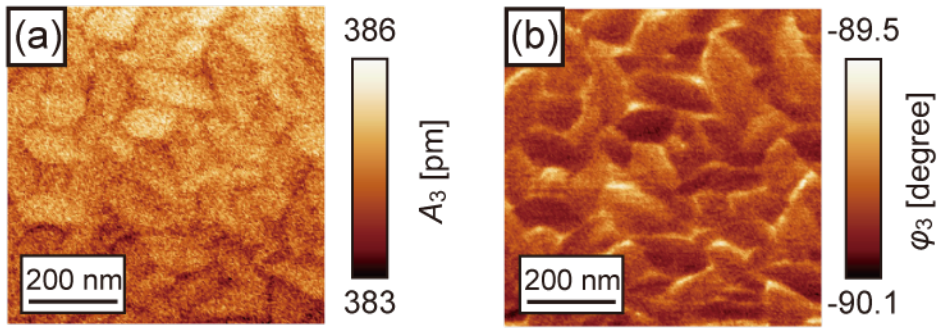

Figure 6.6: The bimodal AFM results on the P(VDF-TrFE) film obtained at 125°C under an ambient condition. (a) Amplitude of the third mode A_3 and (b) Phase of the third mode ϕ_3 simultaneously obtained with topography shown in Fig. 6.4b.

6.4 Summary

In this chapter, simultaneously detect the vertical and lateral force components by a single qPlus sensor with a long probe. The friction anisotropy on the P(VDF-TrFE) was investigated by bimodal AFM utilizing a qPlus sensor with a long probe.

1. The energy dissipation in the third mode corresponding well with the molecular chain orientation in the lamellae grains was observed. This result agreed well with the previous contact-mode LFM study, which indicated that the developed bimodal AFM can detect lateral tip-sample interactions simultaneously with vertical interactions.

2. The conservative interaction in the third mode corresponding well with the molecular chain orientation was also detected.

Chapter 7

Effects of Liquid-Solid Interactions on Polymer Melt near Solid Surfaces

7.1 Introduction

In Chapter 3, the subnanometer-scale imaging at polymer melt/solid interfaces was demonstrated by FM-AFM using qPlus sensors. In Chapters 4-6, the bimodal AFM using the qPlus sensor with a long probe capable of detecting vertical and lateral forces was developed. In this chapter, the developed method is applied to the analysis of polymer lubricant/solid interfaces.

It is known that differences in the interaction between solid surfaces and liquid molecules affect the density distribution and shear properties of liquid molecules near the interface. The shear properties of polymer-liquid/solid interfaces have been analyzed mainly by Surface Force Apparatus (SFA)[3,4,79,83,84,126], while there are few examples of AFM analysis. In SFA experiments, the liquid is confined between atomically flat surfaces, resulting in a large confinement effect. In contrast, in AFM experiments, the pointed tip approaches the surface, resulting in a smaller confinement effect[127]. In addition, the high spatial resolution allows local analysis. Therefore, AFM analysis has the potential to provide different findings.

Dynamic LFM has also been applied to analyze the shear response of various liquids near solid surfaces[33–42]. However, there are few reports that dynamic LFM is applied to the analysis of polymer melt/solid interfaces because the high viscosity of polymer melt reduces the Q factors of sensors, and the force sensitivity is seriously suppressed.

In this chapter, polydimethylsiloxane (PDMS) melt on mica and graphite surfaces is investigated by the bimodal AFM utilizing the qPlus sensor with a long probe, which is capable of subnanometer-resolution imaging in polymer melt and detecting vertical and lateral forces. In this experiment, graphite flakes were supported on a mica surface to investigate both surfaces under the same experimental condition. The purpose of this experiment was to analyze the difference in the interface structure and shear response due to the difference in the interactions between the solid surface and the liquid molecules.

7.2 Experimental

7.2.1 Materials

Polydimethylsiloxane (PDMS) $[(CH_3)_3Si\text{-}O\text{-}[Si(CH_3)_2\text{-}O]_n\text{-}\ Si(CH_3)_3]$ was used as polymer melt. PDMS has a linear siloxane chain (Si-O-Si) as a backbone and two methyl groups per silicon-oxygen unit. Muscovite mica and Graphite were used as solid samples with different surface properties. Mica surface consists of hexagonal-arranged Si atoms (one-quarter are randomly replaced by Al atoms) and ditrigonal-arranged O atoms forming slightly distorted hexagons with a period of 0.52 nm[90]. The tetrahedral layers are negatively charged due to the replacement of one of four Si atoms by Al atoms. In contrast, on graphite surface, carbon atoms are arranged in a honeycomb network. The PDMS melt wets very well on both surfaces (contact angle is below 5°) due to its low surface tension (21.2 mN m^{-1} at 25°C[88]).

7.2.2 Experimental Setup

The experiments are carried out by a system based on a commercial AFM (JEOL, JSPM-5200) with a home-built AFM head made for a qPlus sensor[44]. Figure 7.1 shows a block diagram of the bimodal AFM. The first and third eigenmodes of the sensor were simultaneously excited by using a lead zirconate titanate (PZT) piezoelectric actuator. The current generated from the qPlus sensor was converted to the voltage signal by a differential current preamplifier[69], The signals of f_1 and f_3 were demodulated by two separated phase-lock-loop circuits (Zurich Instruments Ltd., MFLI), and the frequency shifts (Δf_1 and Δf_3) were detected. The amplitude of the first and third modes (A_1 and A_3) were kept constant with automatic gain controllers, and the damping coefficients in these modes (γ_1 and γ_3) was measured via the driving amplitude. Both modes Such an operation of bimodal AFM is so-called frequency modulation-frequency modulation, "FM-FM" bimodal AFM. The tip oscillated mainly in the vertical direction at f_1 and in the lateral direction at f_3. Therefore vertical and lateral interactions were considered to be detected by the first and third modes, respectively. Topographic images were obtained by scanning the tip on the surface while Δf_1 was kept constant.

The qPlus sensor with a probe length of 1.70 mm was used in this experiment, whose f_1 is 11.3 kHz, and f_3 is 136.5 kHz. The tip oscillation angles calculated by the theory described in Sec. 5.2 were 39° and 4.5° for f_1 and f_3, respectively. The effective spring constant of these modes was calculated as $k_{1,v}$=1.85 kN m^{-1} and $k_{3,l}$=45.8 kN m^{-1}

7.2.3 Sample Preparation

Because the tip geometry has a large influence on the results of AFM experiments, care must be taken when comparing results from different experiments. In bimodal qPlus AFM, the eigenfrequency and the tip oscillation angle greatly vary depending on the probe length which also affects experimental results. In order to eliminate

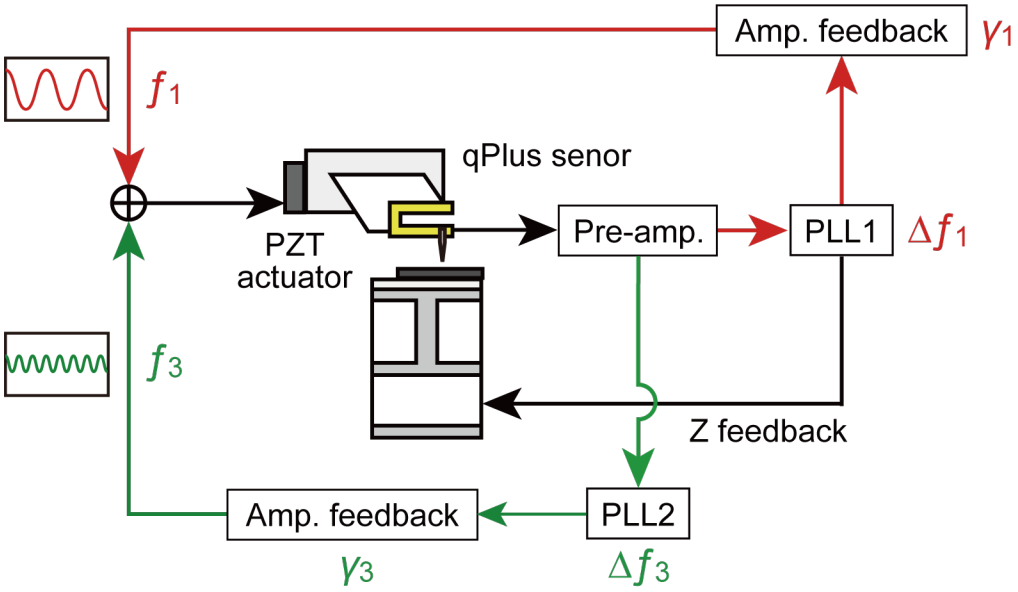

Figure 7.1: Block diagram of the bimodal AFM setup. The sensor is simultaneously mechanically excited at f_1 and f_3. The signals of f_1 and f_3 were demodulated by two separated phase-lock-loop circuits (Zurich Instruments Ltd., MFLI), and the frequency shifts (Δf_1 and Δf_3) were detected. The amplitude of the first and third modes (A_1 and A_3) were kept constant with automatic gain controllers, and the damping coefficients in these modes (γ_1 and γ_3) was measured via the excitation amplitude.

these effects, it is necessary to prepare samples with comparables in the same observation range and analyze them under the same conditions.

A schematic of the sample preparation process, based on Ref. 128, is shown in Fig. 7.2. Sample preparation was carried out in a drying chamber. Two mica substrates (Furuuchi Chemical Co.) and a HOPG substrate (SPI supplies, SPI-2 grade) were cleaved by using scotch tape to expose their clean surfaces. A piece of thin graphite flake was removed from the HOPG substrate and placed on a mica surface. The clean surface of the other mica substrate was pressed on the graphite flake by hand for about 30 s. Then, the graphite flake was removed from the bottom mica surface. 1 μl of poly(dimethylsiloxane) (PDMS, Shin-Etsu Chemical Co., KF96-1000cs) was immediately dropped onto the partially graphite-covered mica surface. The sample was left in the dry chamber for 24 h to allow the PDMS droplet to settle.

The solid-liquid interface of the sample was investigated by bimodal AFM utilizing a qPlus sensor with a long probe in an ambient condition.

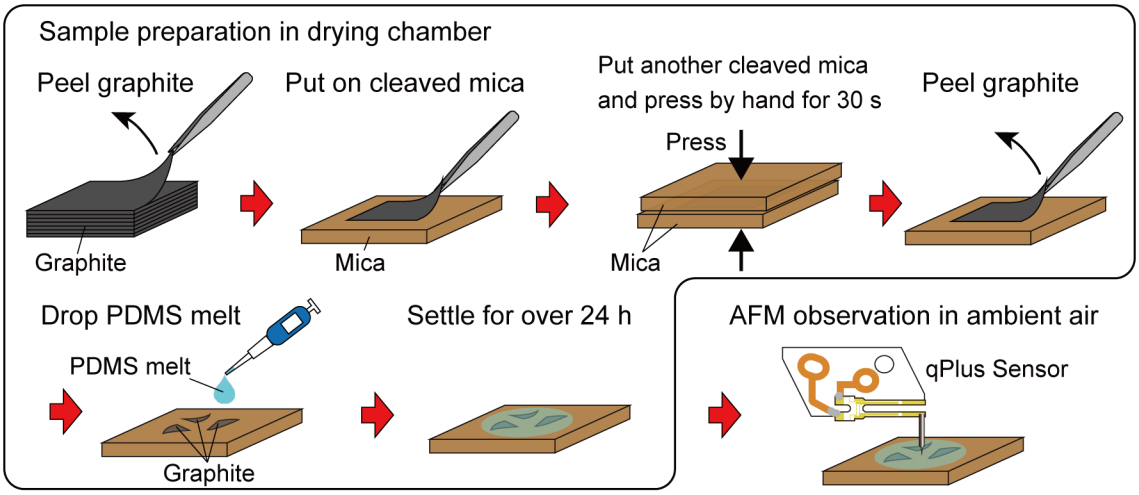

Figure 7.2: Schematic illustration of the preparation process.

7.3 PDMS Melt on Mica and Graphite Investigated by Bimodal AFM

7.3.1 Mica and Graphite Surfaces Investigated in PDMS Melt

Figure 7.3 shows the bimodal AFM images obtained on the partially graphite-covered mica surface in the PDMS melt. These images were taken at $\Delta f_1 = +10$ Hz, where the tip directly interacted with both mica and graphite, which is indicated by Δf_1-distance curves shown in the following part (Fig. 7.4 b). Although the steep increase of Δf_1 indicated the interaction with the solid surface, it is difficult to distinguish whether the tip interacts with mica (graphite) or not. In the case of mica, the atomic structure of the mica surface was successfully imaged (shown in Chapter 3), which indicated that the tip directly interacts with the mica surface.

On the right side of the topographic image (Fig. 7.3 a), a wide terrace about 30 nm higher than the lowest plane was imaged. The damping coefficient of the first

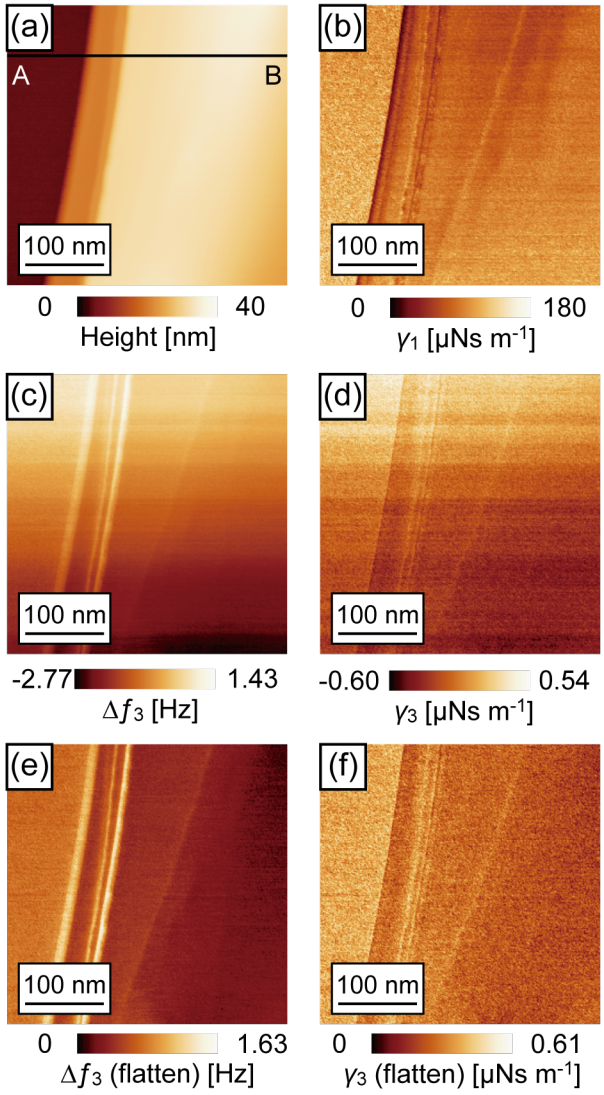

Figure 7.3: Bimodal AFM results on the partially graphite-covered mica in PDMS melt (KF-96-1000cs). (a) Topography (b) Damping of the first mode γ_1 (c) Frequency shift of third mode Δf_3 (d) Damping of the third mode γ_3 (e) flattened imaged of Δf_3 (f) flattened imaged of γ_3. f_1=11.3 kHz, Q_1=110, A_1=170 pm, f_3=136.5 kHz, Q_3=280, A_3=650 pm, Δf_1=+10 Hz.

mode γ_1 image (Fig. 7.3 b) obtained at the same time shows that γ_1 on the lowest plane on the left side is higher than that of the terraces on the right side. In addition, γ_1 is almost constant for the different terrace surfaces on the right side. Although it is difficult to interpret the energy dissipation (damping coefficient) due to the vertical interaction between the tip and the surface, this contrast seems to originate from the difference in surface properties, which leads to the conclusion that the lowest surface on the left side is bare mica surface, and the higher area is graphite.

The frequency shift of the third mode Δf_3 (Fig. 7.3 c) and the damping coefficient of the third mode γ_3 (Fig. 7.3 d) showed that both Δf_3 and γ_3 are lower on the graphite surface than the mica surface, although it is difficult to be recognized because of its drift. The images after applying to "flatten (offset)" filter by the WsXM software to ignore the effect of drift are shown in Figs. 7.3 e and 7.3 f, respectively, which clearly show the contrast described above. Δf_3 is related to the interaction stiffness (conservative force component) of the lateral interaction $k_{int,3}$, $k_{int,3} = 2k_3\Delta f_3/f_3$. The conservative and dissipative components of the lateral interaction, k_3 and γ_3, detected on graphite are lower than on mica. This result is consistent with the relationship between the friction forces detected on mica and HOPG by contact-mode LFM in air[129].

7.3.2 XZ Mapping on Mica and Graphite in PDMS Melt

Next, XZ two-dimensional mapping was carried out by bimodal AFM on line AB in the topographic image (Fig. 7.3 a). Figure 7.4 a shows Δf_1 displayed with a vertical axis as actual height (absolute height) with a schematic illustration of the partially graphite-covered mica substrate. The height variation in this image originated from the existence of the graphite flake supported on the mica surface, which confirmed that this XZ image was taken on the mica and graphite surfaces. To compare the data on mica and graphite, XZ Δf_1 maps obtained on mica and graphite shown in Fig. 7.4 b, which correspond to the areas enclosed by red and white squares in Fig.

7.4 a. These images show a layered contrast parallel to the surface of both mica and graphite. Figures 7.4 d, f, and g show the XZ maps of γ_1, Δf_3, and γ_3, respectively, which are simultaneously obtained with the XZ Δf_1 image (Fig. 7.4 b). These XZ maps are vertically varying and laterally almost homogeneous.

The distance (z) dependence curves extracted from the XZ maps are shown in Figs. 7.4 c, e, g, and i, which are average data of ten curves to reduce noise. Although the absolute value of the distance between the probes cannot be known due to the measurement principle, the endpoints of the two distance-dependent curves were aligned because the measurement was triggered by Δf_1, and the same Δf_1 assumes that the vertical interactions of similar magnitude acted on the tip.

In Δf_1-z curves (Fig. 7.4 c), periodic Δf_1 oscillations of 0.86 nm were observed on both mica and graphite. This result is consistent with the period (0.7-0.9 nm) of the Δf oscillation obtained on mica in Chapter 3. It is also consistent with the jump period detected on mica by contact mode AFM[130] (0.8-1.0 nm) and by SFA[78,79,83] ($\sim$0.7 nm). These periods are consistent with the diameters of the PDMS molecules, indicating that PDMS is distributed in layers on the mica and graphite surfaces with the main chains oriented parallel to the surface, which is obviously indicated by XZ Δf_1 maps (Fig. 7.4 b). Although the period of the frequency shift on the mica and graphite surfaces coincides, the strength of Δf_1 oscillation on graphite is larger than on mica. The frequency shift in FM-AFM is not directly proportional to force gradient but positively correlated. Since the PDMS molecules used in this study were quite large (>100 nm), solvent tip approximation[65,66] cannot be applied to this experimental system. However, it is reasonable that there is a density distribution if there is a distribution in the potential. Assuming that the Δf_1 oscillations correspond to the density variations of the liquid, the greater Δf_1 oscillation detected on the graphite surface indicated larger density variations of PDMS molecules existed on graphite than on mica. Namely, the PDMS molecules are more highly ordered in layers on graphite than on mica.

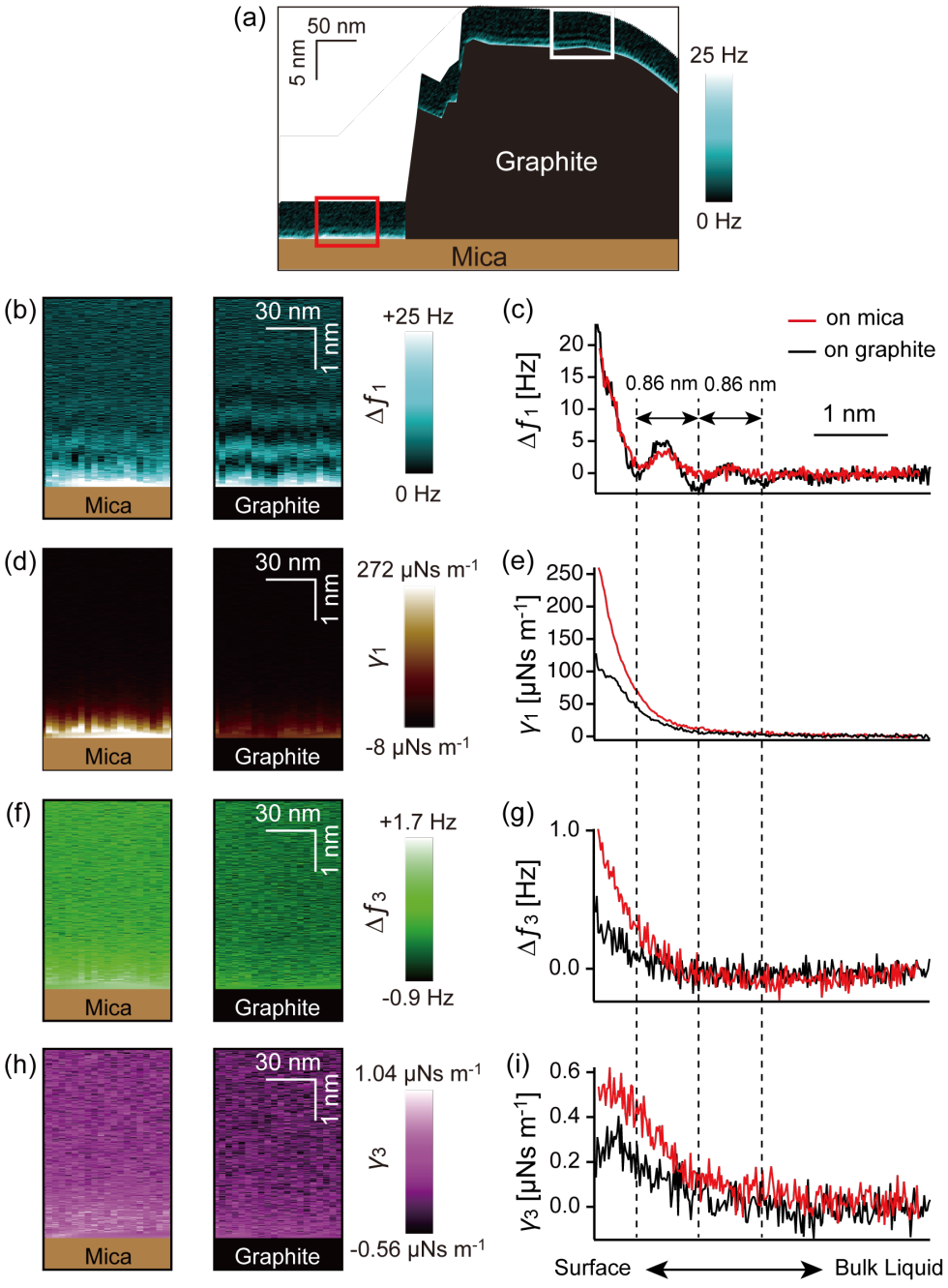

Figure 7.4: (a) XZ map of the frequency shift of first mode Δf_1 on the line AB in Fig. 7.3 a. (b,d,f,h) XZ maps of bimodal AFM data obtained on mica and graphite, corresponding to the areas enclosed by red and white squares in (a). (b) Δf_1 (d) Damping of the first mode γ_1 (f) Frequency shift of third mode Δf_3 (h) Damping of the third mode γ_3 (c,e,g,i) Distance dependence curves extracted from the XZ maps, which are average data of ten curves. (c) Δf_1-z curve (e) γ_1-z curve (g) Δf_3-z curve (i) γ_3-z curve f_1=11.3 kHz, Q_1=110, A_1=170 pm, f_3=136.5 kHz, Q_3=280, A_3=650 pm.

Fig. 7.4 g shows Δf_3-z curves. Δf_3 was below the detection limit at two or more PDMS layers and increased at the PDMS layer adjacent to mica and graphite surfaces. This indicated that the shear responses of the PDMS layer adjacent to mica and graphite have elastic components, and that of two or more PDMS layers is liquid-like without elastic components. Although the shear stiffness of liquids near solid surfaces has been reported by using a piezoquartz resonator[96,131,132] and dynamic LFM[37,38,41], the theoretical background is still lacking and intensively discussed. Assuming the liquid in the gap between the tip and surface as a Maxwell body, which is a spring and a dashpot connected in series, the elastic response is detected when the relaxation time of the liquid molecules is in the comparable order as the experimental shear rate or more. Therefore, these results suggested that the mobility of the PDMS molecules adjacent to both surfaces is dramatically slowed down by solid-liquid interactions.

Fig. 7.4 e and i show γ_1-z curves and γ_3-z curves, increasing monotonically as the tip approaches both surfaces. γ_1 and γ_3 detected on mica are greater than on graphite. The energy dissipation of the tip oscillation on the solid-liquid interface seems to originate from hydrodynamic forces and local tip-liquid molecules interactions[133,134]. The hydrodynamic forces acting on the tip near the solid-liquid interfaces are dominated by the viscosity of the liquid η, tip-surface distance z, the radius of the tip R_{tip}, and the slip length at solid-liquid interfaces b. A previous colloidal probe AFM study reported that no interfacial slip occurs on PDMS/graphite[135]. Assuming no boundary slip condition, the hydrodynamic force caused by the vertical tip oscillation is given by[67] $F_v = (6\pi R_{tip}^2 \eta / z) \cdot dz/dt$, and that caused by the lateral tip oscillation is given by[68] $F_l = (16\pi R_{tip} \eta / 5) \ln (R_{tip}/z) \cdot dx/dt$. The damping coefficients are the coefficients of the right-side term in these equations. In this experiment, the data was obtained on mica and graphite using the same tip, which means R_{tip} was the same value on both surfaces. Therefore, the difference at the same z position is considered to originate from the viscosity of the liquid η. From the γ_1-z curves, γ_3-z

curves, and the above discussion, it was found that the PDMS melt on mica surface shows higher viscosity than on graphite.

7.4 Discussions

Interfacial Structure

The PDMS-graphite interaction is dominated by CH-π interactions[136] between PDMS methyl groups and π-electron-rich graphite surface. CH-π interactions are largely contributed by dispersion forces and partly to charge-transfer and electrostatic forces. The PDMS-mica interaction is dominated by charge-dipole interactions between negatively-charged Al atoms and dipoles in PDMS molecules, which is stronger than dominated by CH-π interactions dominating the PDMS-graphite interaction. In the case of low-molecular-weight liquids, the stronger solid-liquid interactions lead to larger density oscillation, which is indicated by molecular dynamics (MD) simulations[137]. However, Δf_1-z curves indicated that the PDMS molecules are more highly ordered in layers on graphite than on mica. There may be factors that affect the molecular ordering of liquids other than the magnitude of the surface-liquid interactions.

It was indicated by a previous report[138] using X-ray absorption near fine structure spectroscopy study that poly(dimethylsilane) ($(CH_3)_3Si$-$[Si(CH_3)_2]_n$- $Si(CH_3)_3$)) formed layered structures on a graphite surface. In a previous report[139], MD simulations of the composite of PDMS and carbon nanotubes showed that the PDMS molecules wrap around the carbon nanotubes. These results were explained by the formation of more CH-π bondings as the polymers lie along the π-electron-rich surfaces. Probably for the same reason, the highly oriented layered structure of the PDMS molecules on graphite (Fig. 7.5 b) was observed in this experiment. This mechanism is similar to the well-known layered structure of alkyl chains on graphite[26,140,141].

On the other hand, the PDMS-mica interaction is dominated by charge-dipole interactions between dipoles in PDMS and negatively charged Al atom sites on the

mica surface. The negatively-charged Al atoms on mica surfaces randomly exist at one-quarter of hexagonal-arranged Si atom sites. Although the attraction interaction is stronger, the mica surface has fewer adsorption sites (Al atom sites: 2.1 nm^{-2}) than the graphite surface (C six-membered rings: 19 nm^{-2}), which seems to lead to the less ordered layered structure of PDMS molecules (Fig. 7.5 a).

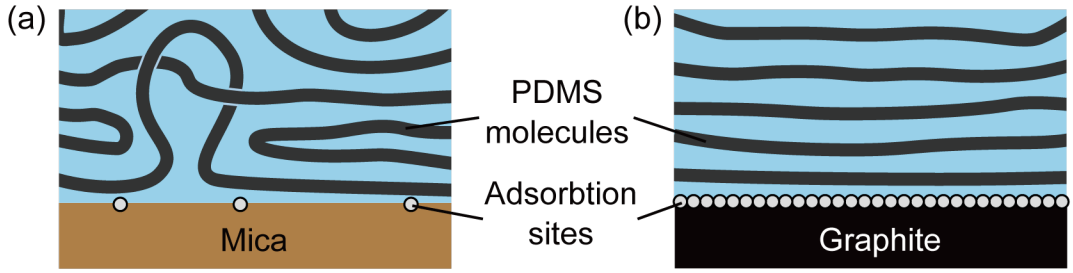

Figure 7.5: Schematic illustration of the layered ordering mechanisms of PDMS molecules on solid surfaces (a) mica (b) graphite.

Viscosity

It was reported by dynamic AFM[142] and dynamic LFM[35] that the apparent viscosity of water near solid surfaces is dramatically affected by its wettability, which was explained as originating from differences in slip length[35]. In this experiment, however, PDMS melt has good wettability on both mica and graphite surfaces, and no-slip condition was reported at PDMS/graphite interfaces[135]. Therefore, the viscosity of PDMS melt was assumed to be different on these surfaces.

The interaction between PDMS and mica, which is stronger than that between PDMS and graphite, would enhance the viscosity of the PDMS melt near solid surfaces. The intermolecular interactions of PDMS molecules are weak because there are mainly consist of van der Waals interactions. Since the molecular chain is large ($>$ 100 nm) and PDMS molecules adsorb on the mica surface partially, however, the non-adsorbing parts of adsorbed PDMS have less mobility than molecules that are not adsorbed at all. Therefore, even the viscosity of the second or more layers increased. On the other hand, experiments using SFA[83] have also reported that

the frictional force is lower for PDMS melts well-ordered parallel to the surface. The highly oriented layered structure of the PDMS molecules on graphite would decrease its viscosity.

7.5 Summary

In this chapter, the developed bimodal AFM was applied to the analysis of polymer melt/solid interfaces. The PDMS melt on mica and graphite was investigated by bimodal AFM utilizing a qPlus sensor with a long probe.

1. The shear response of the PDMS melt was analyzed simultaneously with subnanometer-resolution imaging of the density distribution of PDMS molecules near the mica and graphite surfaces.

2. It was indicated that solid-liquid interactions dramatically affect the density distribution, shear response, and viscosity of the polymer melt near solid surfaces.

Chapter 8

Conclusion and Future Prospects

8.1 Conclusions

Subnanometer-scale Imaging in Polymer Melt

In Chapter 3, FM-AFM utilizing qPlus sensors was applied to the analysis of polymer melt/solid interfaces.

1. Subnanometer-resolution imaging of the solid surface and density distribution of polymer melt near the solid surface was successfully achieved, which indicated that FM-AFM utilizing qPlus sensors is useful for high-resolution structural analysis of polymer melt/solid interfaces.

2. It was indicated that distance-dependent energy dissipation measurement is useful for analysis of the dynamics of polymer melt near solid surfaces.

Development of Vertical-Lateral Bimodal AFM utilizing qPlus Sensors

In Chapters 4, 5, and 6, the method to detect vertical and lateral forces by a single qPlus sensor was developed.

1. First three eigenmodes of the qPlus sensor with a long probe were successfully described by the constructed model, which revealed the probe length depen-

dence of the sensor characteristics, such as eigenfrequency, eigenmode shape, tip oscillation angle, effective spring constant, and piezoelectric sensitivity.

2. The lateral tip oscillation in the higher modes of the qPlus sensor with a long probe was confirmed by theory, simulation, and experiment.

3. It was experimentally confirmed that vertical and lateral forces can be detected simultaneously by the bimodal AFM utilizing the first and third modes of the qPlus sensor with a long probe.

Effects of Liquid-Solid Interactions on Polymer Melt near Solid Surfaces

In Chapter 7, the developed bimodal AFM was applied to the analysis of polymer melt/solid interfaces.

1. The shear response of a polymer melt on solid surfaces was analyzed simultaneously with subnanometer-resolution imaging of the density distribution of polymer melt near the solid surface by bimodal AFM utilizing the qPlus sensor with a long probe.

2. It was indicated that solid-liquid interactions dramatically affect the density distribution, shear response, and viscosity of the polymer melt near solid surfaces.

8.2 Future Prospects

Further Applications to Investigation of Lubricant/Solid Interfaces

In this thesis, the bimodal AFM investigation was applied to the investigation of the polymer melt/solid interfaces, namely, base oil/solid interfaces. In the practical lubrication conditions, the additives are added to base oils, which greatly affects the interfacial structure and lubrication performance due to adsorption and reaction on the solid surface. The bimodal AFM developed in this work can be applied to the

lubricated interfaces with additives and would reveal the interfacial structure and the dynamic properties at the molecular scale.

Applications to Other Environments

In this thesis, polymer lubricant/solid interfaces were focused on. On the other hand, the bimodal AFM using qPlus sensors can be applied to other environments, such as UHV, ambient conditions, and other liquid environments. In particular, the qPlus sensor with a long probe has already been applied to chemical bond imaging in UHV[56]. The vertical and lateral forces detection at solid surfaces or solid/liquid interfaces would reveal the mechanisms of various phenomena at the atomic or molecular scale.

Further Improvement of Force Sensors

In this thesis, the probe-length dependence of sensor characteristics was theoretically analyzed, and the probe length was optimized for the simultaneous detection of vertical and lateral forces. However, the eigenmodes of qPlus sensors are also affected by the shape of the QTF and the diameter and material of the probe. Optimization of these characteristics would improve the force sensitivity and spatial resolution.

The minimum detectable force gradient is inversely proportional to the effective spring constant of the eigenmodes. The second mode, whose spring constant is much lower than the third mode, wasn't used because of its low piezoelectric sensitivity in this work. The piezoelectric sensitivity is affected by the eigenmode shape and the design of the electrode on the QTF. It is expected that the force sensitivity would be improved if the second mode becomes useful through the improvement of its piezoelectric sensitivity by optimizing the electrode design.

Appendix A

Details of Theoretical Analysis of Eigenmodes

A.1 Equations of Motion

The total kinetic energy T and potential energy U of a qPlus sensor are given by Eq. 5.1. Using Eq. 5.1 along with Hamilton's principle, the equations of motion for free undamped oscillations are obtained as below,

$$E_q I_q \frac{\partial^4 w}{\partial x_1^4}(x_1,t) + \rho_q A_q \ddot{w}(x_1,t) = 0, \tag{A.1a}$$

$$E_w I_w \frac{\partial^4 u}{\partial x_2^4}(x_2,t) + \rho_w A_w \left(\ddot{u}(x_2,t) + \left(x_2 + \frac{h}{2} \right) \frac{\partial \ddot{w}}{\partial x_1}(L,t) \right) = 0, \tag{A.1b}$$

and the boundary conditions for the QTF prong,

$$w(0,t) = 0, \tag{A.2a}$$

$$\frac{\partial w}{\partial x_1}(0,t) = 0, \tag{A.2b}$$

$$E_q I_q \frac{\partial^3 w}{\partial x_1^3}(L,t) - M_{probe} \left(\ddot{w}(L,t) + \frac{d}{2} \frac{\partial \ddot{w}}{\partial x_1}(L,t) \right) = 0, \tag{A.2c}$$

$$
\begin{aligned}
&-E_q I_q \frac{\partial^2 w}{\partial x_1^2}(L,t) - \frac{d}{2} M_{probe}\left(\ddot{w}(L,t) + \frac{d}{2}\frac{\partial \ddot{w}}{\partial x_1}(L,t)\right) - I_a \frac{\partial \ddot{w}}{\partial x_1}(L,t) \\
&-I_c\left(\frac{\partial \ddot{w}}{\partial x_1}(L,t) + \frac{\partial \ddot{u}}{\partial x_2}(l_b,t)\right) + \int_0^{l_b} -\rho_w A_w \left(x_2 + \frac{h}{2}\right)\left(\ddot{u}(x_2,t) + \left(x_2 + \frac{h}{2}\right)\frac{\partial \ddot{w}}{\partial x_1}(L,t)\right) dx_2 \\
&-\left(l_b + \frac{h}{2} + \frac{1}{4}l_c\right) M_c\left(\ddot{u}(l_b,t) + \frac{1}{4}l_c \frac{\partial \ddot{u}}{\partial x_2}(l_b,t) + \left(l_b + \frac{h}{2} + \frac{1}{4}l_c\right)\frac{\partial \ddot{w}}{\partial x_1}(L,t)\right) = 0,
\end{aligned}
\tag{A.2d}
$$

and the boundary conditions for the tungsten needle,

$$u(0,t) = 0, \tag{A.3a}$$

$$\frac{\partial u}{\partial x_2}(0,t) = 0, \tag{A.3b}$$

$$E_w I_w \frac{\partial^3 u}{\partial x_2^3}(l_b,t) - M_c\left(\ddot{u}(l_b,t) + \frac{1}{4}l_c\frac{\partial \ddot{u}}{\partial x_2}(l_b,t) + \left(l_b + \frac{h}{2} + \frac{1}{4}l_c\right)\frac{\partial \ddot{w}}{\partial x_1}(L,t)\right) = 0, \tag{A.3c}$$

$$
\begin{aligned}
&-E_w I_w \frac{\partial^2 u}{\partial x_2^2}(l_b,t) - I_c\left(\frac{\partial \ddot{w}}{\partial x_1}(L,t) + \frac{\partial \ddot{u}}{\partial x_2}(l_b,t)\right) \\
&-\frac{1}{4}M_c\left(\ddot{u}(l_b,t) + \frac{1}{4}l_c\frac{\partial \ddot{u}}{\partial x_2}(l_b,t) + \left(l_b + \frac{h}{2} + \frac{1}{4}l_c\right)\frac{\partial \ddot{w}}{\partial x_1}(L,t)\right) = 0,
\end{aligned}
\tag{A.3d}
$$

A.2 The Elements of Matrix $\boldsymbol{M}$

The elements of the matrix $[M]$ in Eq. 5.7 are given by,

$$M_{11} = -\alpha\frac{h}{2}\left(\cos(\alpha L) - \cosh(\alpha L)\right),$$

$$M_{12} = -\alpha\frac{h}{2}\left(-\sin(\alpha L) - \sinh(\alpha L)\right),$$

$$M_{13} = M_{15} = M_{24} = M_{26} = M_{33} = M_{34} = M_{35} = M_{36} = M_{51} = M_{52} = M_{61} = M_{62} = 0,$$

$$M_{14} = M_{16} = 1,$$

$$M_{21} = -\alpha\left(\cos(\alpha L) - \cosh(\alpha L)\right),$$

$$M_{22} = -\alpha\left(-\sin\left(\alpha L\right) - \sinh\left(\alpha L\right)\right),$$

$$M_{23} = M_{25} = \beta,$$

$$\begin{aligned} M_{31} = {} & E_q I_q \alpha^3 \left(-\cos\left(\alpha L\right) - \cosh\left(\alpha L\right)\right) + M_{tip}\omega^2 \left(\sin\left(\alpha L\right) - \sinh\left(\alpha L\right)\right) \\ & + M_{tip}\omega^2 \frac{d}{2}\alpha\left(\cos\left(\alpha L\right) - \cosh\left(\alpha L\right)\right), \end{aligned}$$

$$\begin{aligned} M_{32} = {} & E_q I_q \alpha^3 \left(\sin\left(\alpha L\right) - \sinh\left(\alpha L\right)\right) + M_{tip}\omega^2 \left(\cos\left(\alpha L\right) - \cosh\left(\alpha L\right)\right) \\ & + M_{tip}\omega^2 \frac{d}{2}\alpha\left(-\sin\left(\alpha L\right) - \sinh\left(\alpha L\right)\right), \end{aligned}$$

$$\begin{aligned} M_{41} = {} & -E_q I_q \alpha^2 \left(-\sin\left(\alpha L\right) - \sinh\left(\alpha L\right)\right) + \frac{d}{2} M_{tip}\omega^2 \left(\sin\left(\alpha L\right) - \sinh\left(\alpha L\right)\right) \\ & + \left(\left(\frac{d}{2}\right)^2 M_{tip} + I_a\right)\omega^2 \alpha\left(\cos\left(\alpha L\right) - \cosh\left(\alpha L\right)\right), \end{aligned}$$

$$\begin{aligned} M_{42} = {} & -E_q I_q \alpha^2 \left(-\cos\left(\alpha L\right) - \cosh\left(\alpha L\right)\right) + \frac{d}{2} M_{tip}\omega^2 \left(\cos\left(\alpha L\right) - \cosh\left(\alpha L\right)\right) \\ & + \left(\left(\frac{d}{2}\right)^2 M_{tip} + I_a\right)\omega^2 \alpha\left(-\sin\left(\alpha L\right) - \sinh\left(\alpha L\right)\right), \end{aligned}$$

$$\begin{aligned} M_{43} = {} & \left(I_c + \frac{1}{4} l_c M_c \left(l_b + \frac{h}{2} + \frac{1}{4} l_c\right)\right)\omega^2 \beta \cos\left(\beta l_b\right) + \left(l_b + \frac{h}{2} + \frac{1}{4} l_c\right) M_c \omega^2 \sin\left(\beta l_b\right) \\ & + \rho_w A_w \omega^2 \left(-\frac{1}{\beta}\left(l_b + \frac{h}{2}\right)\cos\left(\beta l_b\right) + \frac{1}{\beta^2}\sin\left(\beta l_b\right) + \frac{h}{2\beta}\right), \end{aligned}$$

$$\begin{aligned} M_{44} = {} & -\left(I_c + \frac{1}{4} l_c M_c \left(l_b + \frac{h}{2} + \frac{1}{4} l_c\right)\right)\omega^2 \beta \sin\left(\beta l_b\right) + \left(l_b + \frac{h}{2} + \frac{1}{4} l_c\right) M_c \omega^2 \cos\left(\beta l_b\right) \\ & + \rho_w A_w \omega^2 \left(\frac{1}{\beta}\left(l_b + \frac{h}{2}\right)\sin\left(\beta l_b\right) + \frac{1}{\beta^2}\cos\left(\beta l_b\right) - \frac{1}{\beta^2}\right), \end{aligned}$$

$$\begin{aligned} M_{45} = {} & \left(I_c + \frac{1}{4} l_c M_c \left(l_b + \frac{h}{2} + \frac{1}{4} l_c\right)\right)\omega^2 \beta \cosh\left(\beta l_b\right) + \left(l_b + \frac{h}{2} + \frac{1}{4} l_c\right) M_c \omega^2 \sinh\left(\beta l_b\right) \\ & + \rho_w A_w \omega^2 \left(\frac{1}{\beta}\left(l_b + \frac{h}{2}\right)\cosh\left(\beta l_b\right) - \frac{1}{\beta^2}\sinh\left(\beta l_b\right) - \frac{h}{2\beta}\right), \end{aligned}$$

$$\begin{aligned} M_{46} = {} & \left(I_c + \frac{1}{4} l_c M_c \left(l_b + \frac{h}{2} + \frac{1}{4} l_c\right)\right)\omega^2 \beta \sinh\left(\beta l_b\right) + \left(l_b + \frac{h}{2} + \frac{1}{4} l_c\right) M_c \omega^2 \cosh\left(\beta l_b\right) \\ & + \rho_w A_w \omega^2 \left(\frac{1}{\beta}\left(l_b + \frac{h}{2}\right)\sinh\left(\beta l_b\right) - \frac{1}{\beta^2}\cosh\left(\beta l_b\right) + \frac{1}{\beta^2}\right), \end{aligned}$$

$$M_{53} = \left(-E_w I_w \beta^3 + \frac{1}{4} l_c M_c \omega\ 2\beta\right)\cos\left(\beta l_b\right) + M_c \omega^2 \sin\left(\beta l_b\right),$$

$$M_{54} = \left(E_w I_w \beta^3 - \frac{1}{4} l_c M_c \omega \; 2\beta \right) \sin(\beta l_b) + M_c \omega^2 \cos(\beta l_b),$$

$$M_{55} = \left(E_w I_w \beta^3 + \frac{1}{4} l_c M_c \omega \; 2\beta \right) \cosh(\beta l_b) + M_c \omega^2 \sinh(\beta l_b),$$

$$M_{56} = \left(E_w I_w \beta^3 + \frac{1}{4} l_c M_c \omega \; 2\beta \right) \sinh(\beta l_b) + M_c \omega^2 \cosh(\beta l_b),$$

$$M_{63} = \left(E_w I_w \beta^2 + \frac{1}{4} l_c M_c \omega^2 \right) \sin(\beta l_b) + \left(\left(\frac{1}{4} l_c \right)^2 M_c + I_c \right) \omega^2 \cos(\beta l_b),$$

$$M_{64} = \left(E_w I_w \beta^2 + \frac{1}{4} l_c M_c \omega^2 \right) \cos(\beta l_b) - \left(\left(\frac{1}{4} l_c \right)^2 M_c + I_c \right) \omega^2 \sin(\beta l_b),$$

$$M_{65} = \left(-E_w I_w \beta^2 + \frac{1}{4} l_c M_c \omega^2 \right) \sinh(\beta l_b) + \left(\left(\frac{1}{4} l_c \right)^2 M_c + I_c \right) \omega^2 \cosh(\beta l_b),$$

$$M_{66} = \left(-E_w I_w \beta^2 + \frac{1}{4} l_c M_c \omega^2 \right) \cosh(\beta l_b) + \left(\left(\frac{1}{4} l_c \right)^2 M_c + I_c \right) \omega^2 \sinh(\beta l_b).$$

All elements of the matrix M_{ij} shown here are functions of α and β. According to Eq. 5.6, they can be represented only by functions of the angular frequency ω.

Bibliography

[1] C. M. Mate, *Tribology on the Small Scale*, Oxford University Press, 2007.

[2] R. Stribeck, *Zeitschrift des Vereines Deutscher Ingenieure*, 1902, **46**, 1342–1348.

[3] J. V. Alsten and S. Granick, *Macromolecules*, 1990, **23**, 4856–4862.

[4] H.-W. Hu and S. Granick, *Science*, 1992, **258**, 1339–1342.

[5] G. Binnig, C. F. Quate and C. Gerber, *Physical Review Letters*, 1986, **56**, 930.

[6] C. M. Mate, G. M. McClelland, R. Erlandsson and S. Chiang, *Physical Review Letters*, 1987, **59**, 1942–1945.

[7] P. A. Thompson, G. S. Grest and M. O. Robbins, *Physical Review Letters*, 1992, **68**, 3448–3451.

[8] J. Gao, W. D. Luedtke and U. Landman, *The Journal of Physical Chemistry B*, 1997, **101**, 4013–4023.

[9] B. Bhushan, J. N. Israelachvili and U. Landman, *Nature*, 1995, **374**, 607–616.

[10] G. Dedkov, *Uspekhi Fizicheskih Nauk*, 2000, **170**, 585.

[11] G. Binnig, H. Rohrer, C. Gerber and E. Weibel, *Physical Review Letters*, 1982, **49**, 57–61.

[12] Y. Martin, C. C. Williams and H. K. Wickramasinghe, *Journal of Applied Physics*, 1987, **61**, 4723–4729.

[13] T. R. Albrecht, P. Grütter, D. Horne and D. Rugar, *Journal of Applied Physics*, 1991, **69**, 668–673.

[14] F. J. Giessibl, *Science*, 1995, **267**, 68.

[15] S.-i. Kitamura and M. I. Masashi Iwatsuki, *Japanese Journal of Applied Physics*, 1995, **34**, L145.

[16] O. Pfeiffer, R. Bennewitz, A. Baratoff, E. Meyer and P. Grütter, *Physical Review B*, 2002, **65**, 161403.

[17] F. J. Giessibl, M. Herz and J. Mannhart, *Proceedings of the National Academy of Sciences*, 2002, **99**, 12006–12010.

[18] S. Kawai, S.-i. Kitamura, D. Kobayashi and H. Kawakatsu, *Applied Physics Letters*, 2005, **87**, 173105.

[19] T. R. Rodriguez and R. Garcia, *Applied Physics Letters*, 2004, **84**, 449–451.

[20] S. Kawai, T. Glatzel, S. Koch, B. Such, A. Baratoff and E. Meyer, *Physical Review B*, 2010, **81**, 085420.

[21] S. Kawai, F. F. Canova, T. Glatzel, T. Hynninen, E. Meyer and A. S. Foster, *Physical Review Letters*, 2012, **109**, 146101.

[22] F. Federici Canova, S. Kawai, C. de Capitani, K.-i. Kan'no, T. Glatzel, B. Such, A. S. Foster and E. Meyer, *Physical Review Letters*, 2013, **110**, 203203.

[23] Y. Naitoh, R. Turanský, J. Brndiar, Y. J. Li, I. Štich and Y. Sugawara, *Nature Physics*, 2017, **13**, 663–667.

[24] T. Fukuma, K. Kobayashi, K. Matsushige and H. Yamada, *Applied Physics Letters*, 2005, **87**, 034101.

[25] T. Hiasa, T. Sugihara, K. Kimura and H. Onishi, *Journal of Physics: Condensed Matter*, 2012, **24**, 084011.

[26] T. Hiasa, K. Kimura and H. Onishi, *The Journal of Physical Chemistry C*, 2012, **116**, 26475–26479.

[27] Y. Yokota, H. Hara, T. Harada, A. Imanishi, T. Uemura, J. Takeya and K.-i. Fukui, *Chemical Communications*, 2013, **49**, 10596.

[28] T. Fukuma, Y. Ueda, S. Yoshioka and H. Asakawa, *Physical Review Letters*, 2010, **104**, 016101.

[29] K. Kimura, S. Ido, N. Oyabu, K. Kobayashi, Y. Hirata, T. Imai and H. Yamada, *The Journal of Chemical Physics*, 2010, **132**, 194705.

[30] T. Hirayama, R. Kawamura, K. Fujino, T. Matsuoka, H. Komiya and H. Onishi, *Langmuir*, 2017, **33**, 10492–10500.

[31] H. Okubo and S. Sasaki, *Tribology Letters*, 2019, **67**, 3.

[32] S. Moriguchi, T. Tsujimoto, A. Sasahara, R. Kokawa and H. Onishi, *ACS Omega*, 2019, **4**, 17593–17599.

[33] T.-D. Li, J. Gao, R. Szoszkiewicz, U. Landman and E. Riedo, *Physical Review B*, 2007, **75**, 115415.

[34] T.-D. Li and E. Riedo, *Physical Review Letters*, 2008, **100**, 106102.

[35] D. Ortiz-Young, H.-C. Chiu, S. Kim, K. Voïtchovsky and E. Riedo, *Nature Communications*, 2013, **4**, 2482.

[36] T.-D. Li, H.-C. Chiu, D. Ortiz-Young and E. Riedo, *Review of Scientific Instruments*, 2014, **85**, 123707.

[37] M. Kageshima, *EPL (Europhysics Letters)*, 2014, **107**, 66001.

[38] M.-D. Krass, N. N. Gosvami, R. W. Carpick, M. H. Müser and R. Bennewitz, *Journal of Physics: Condensed Matter*, 2016, **28**, 134004.

[39] G. Krämer, F. Hausen and R. Bennewitz, *Faraday Discussions*, 2017, **199**, 299–309.

[40] C. Cafolla and K. Voïtchovsky, *Nanoscale*, 2018, **10**, 11831–11840.

[41] G. Krämer and R. Bennewitz, *The Journal of Physical Chemistry C*, 2019, **123**, 28284–28290.

[42] C. Cafolla, W. Foster and K. Voïtchovsky, *Science Advances*, 2020, **6**, 1–9.

[43] F. J. Giessibl, *Applied Physics Letters*, 1998, **73**, 3956–3958.

[44] T. Ichii, M. Fujimura, M. Negami, K. Murase and H. Sugimura, *Japanese Journal of Applied Physics*, 2012, **51**, 08KB08.

[45] T. Ichii, M. Negami and H. Sugimura, *The Journal of Physical Chemistry C*, 2014, **118**, 26803–26807.

[46] F. J. Giessibl, *Applied Physics Letters*, 2000, **76**, 1470–1472.

[47] D. S. Wastl, A. J. Weymouth and F. J. Giessibl, *Physical Review B*, 2013, **87**, 245415.

[48] D. S. Wastl, A. J. Weymouth and F. J. Giessibl, *ACS Nano*, 2014, **8**, 5233–5239.

[49] A. J. Weymouth, D. Meuer, P. Mutombo, T. Wutscher, M. Ondracek, P. Jelinek and F. J. Giessibl, *Physical Review Letters*, 2013, **111**, 126103.

[50] A. J. Weymouth, E. Riegel, O. Gretz and F. J. Giessibl, *Physical Review Letters*, 2020, **124**, 196101.

[51] R. C. Tung, T. Wutscher, D. Martinez-Martin, R. G. Reifenberger, F. Giessibl and A. Raman, *Journal of Applied Physics*, 2010, **107**, 104508.

[52] S. Higuchi, H. Kuramochi, O. Kubo, S. Masuda, Y. Shingaya, M. Aono and T. Nakayama, *Review of Scientific Instruments*, 2011, **82**, 043701.

[53] K. Chen, Z. Liu, Y. Xie, C. Zhang, G. Xu, W. Song and K. Xu, *Beilstein Journal of Nanotechnology*, 2021, **12**, 82–92.

[54] D. Kirpal, J. Qiu, K. Pürckhauer, A. J. Weymouth, M. Metz and F. J. Giessibl, *Review of Scientific Instruments*, 2021, **92**, 043703.

[55] M. G. Ruppert, D. Martin-Jimenez, Y. K. Yong, A. Ihle, A. Schirmeisen, A. J. Fleming and D. Ebeling, *Nanotechnology*, 2022, **33**, 185503.

[56] D. Martin-Jimenez, M. G. Ruppert, A. Ihle, S. Ahles, H. A. Wegner, A. Schirmeisen and D. Ebeling, *Nanoscale*, 2022, **14**, 5329–5339.

[57] G. Meyer and N. M. Amer, *Applied Physics Letters*, 1990, **57**, 2089–2091.

[58] R. Erlandsson, G. Hadziioannou, C. M. Mate, G. M. McClelland and S. Chiang, *The Journal of Chemical Physics*, 1988, **89**, 5190–5193.

[59] S. Kawai, N. Sasaki and H. Kawakatsu, *Physical Review B*, 2009, **79**, 195412.

[60] N. Sasaki, S. Kawai and H. Kawakatsu, *Physical Review B*, 2009, **80**, 193402.

[61] J. Israelachvili, *Intermolecular and Surface Forces, 3rd ed.*, Academic, London, 1991.

[62] H. K. Christenson, D. W. R. Gruen, R. G. Horn and J. N. Israelachvili, *The Journal of Chemical Physics*, 1987, **87**, 1834–1841.

[63] T. Hiasa, K. Kimura and H. Onishi, *Colloids and Surfaces A: Physicochemical and Engineering Aspects*, 2012, **396**, 203–207.

[64] T. Fukuma, B. Reischl, N. Kobayashi, P. Spijker, F. F. Canova, K. Miyazawa and A. S. Foster, *Physical Review B*, 2015, **92**, 155412.

[65] M. Watkins and B. Reischl, *The Journal of Chemical Physics*, 2013, **138**, 154703.

[66] K.-i. Amano, K. Suzuki, T. Fukuma, O. Takahashi and H. Onishi, *The Journal of Chemical Physics*, 2013, **139**, 224710.

[67] S. J. O'Shea and M. E. Welland, *Langmuir*, 1998, **14**, 4186–4197.

[68] J. Klein and E. Kumacheva, *The Journal of Chemical Physics*, 1998, **108**, 6996–7009.

[69] F. Huber and F. J. Giessibl, *Review of Scientific Instruments*, 2017, **88**, 073702.

[70] R. Pallás-Areny and J. G. Webster, *Analog Signal Processing*, Wiley-Interscience, 1999.

[71] F. J. Giessibl, *Physical Review B*, 1997, **56**, 16010–16015.

[72] J. E. Sader and S. P. Jarvis, *Applied Physics Letters*, 2004, **84**, 1801–1803.

[73] S. Kawai, T. Glatzel, S. Koch, B. Such, A. Baratoff and E. Meyer, *Physical Review Letters*, 2009, **103**, 220801.

[74] A. J. Katan, M. H. van Es and T. H. Oosterkamp, *Nanotechnology*, 2009, **20**, 165703.

[75] K. Kobayashi, H. Yamada and K. Matsushige, *Review of Scientific Instruments*, 2009, **80**, 043708.

[76] G. Evmenenko, S. W. Dugan, J. Kmetko and P. Dutta, *Langmuir*, 2001, **17**, 4021–4024.

[77] G. Evmenenko, H. Mo, S. Kewalramani and P. Dutta, *Polymer*, 2006, **47**, 878–882.

[78] R. G. Horn and J. N. Israelachvili, *Macromolecules*, 1988, **21**, 2836–2841.

[79] S. Yamada, *Langmuir*, 2003, **19**, 7399–7405.

[80] C. M. Mate, M. R. Lorenz and V. J. Novotny, *The Journal of Chemical Physics*, 1989, **90**, 7550–7555.

[81] G. Sun and H.-J. Butt, *Macromolecules*, 2004, **37**, 6086–6089.

[82] G. Sun, M. Kappl, T. Pakula, K. Kremer and H.-J. Butt, *Langmuir*, 2004, **20**, 8030–8034.

[83] S. Yamada, *Tribology Online*, 2006, **1**, 29–33.

[84] P. M. McGuiggan, M. L. Gee, H. Yoshizawa, S. J. Hirz and J. N. Israelachvili, *Macromolecules*, 2007, **40**, 2126–2133.

[85] C. M. Mate, *Physical Review Letters*, 1992, **68**, 3323–3326.

[86] M. Negami, T. Ichii, K. Murase and H. Sugimura, *ECS Transactions*, 2013, **50**, 349–355.

[87] M. C. Friedenberg and C. M. Mate, *Langmuir*, 1996, **12**, 6138–6142.

[88] Shin-Etsu Chemical Co. Ltd., *Silicone Fluid KF-96*.

[89] A. J. Barry, *Journal of Applied Physics*, 1946, **17**, 1020–1024.

[90] H. K. Christenson and N. H. Thomson, *Surface Science Reports*, 2016, **71**, 367–390.

[91] C. Jai, J. P. Aimé and R. Boisgard, *EPL (Europhysics Letters)*, 2008, **81**, 34003.

[92] M. Delmas, M. Monthioux and T. Ondarçuhu, *Physical Review Letters*, 2011, **106**, 136102.

[93] J. Dupré de Baubigny, M. Benzaquen, L. Fabié, M. Delmas, J.-P. Aimé, M. Legros and T. Ondarçuhu, *Langmuir*, 2015, **31**, 9790–9798.

[94] A. J. Barlow, G. Harrison and J. Lamb, *Proceedings of the Royal Society of London. Series A. Mathematical and Physical Sciences*, 1964, **282**, 228–251.

[95] J. Lamb and P. Lindon, *The Journal of the Acoustical Society of America*, 1967, **41**, 1032–1042.

[96] B. Badmaev, U. Bazaron, B. Derjaguin and O. Budaev, *Physica B+C*, 1983, **122**, 241–245.

[97] U. Bazaron, B. Deryagin and A. Bulgadaev, *Progress in Surface Science*, 1992, **40**, 316–321.

[98] A. Maali, T. Cohen-Bouhacina, G. Couturier and J.-P. Aimé, *Physical Review Letters*, 2006, **96**, 086105.

[99] S. de Beer, D. van den Ende and F. Mugele, *Nanotechnology*, 2010, **21**, 325703.

[100] W. Hofbauer, R. J. Ho, H. R., N. N. Gosvami and S. J. O'Shea, *Physical Review B*, 2009, **80**, 134104.

[101] J. E. Mark, in *Silicones and Silicone-Modified Materials*, American Chemical Society, 2000, vol. 729 of ACS Symposium Series, p. 1.

[102] M. Umemoto, R. Kawamura, H. Y. Yoshikawa, S. Nakabayashi and N. Kobayashi, *Japanese Journal of Applied Physics*, 2020, **59**, SIII01.

[103] A. J. Weymouth, T. Hofmann and F. J. Giessibl, *Science*, 2014, **343**, 1120–1122.

[104] H. Ooe, D. Kirpal, D. S. Wastl, A. J. Weymouth, T. Arai and F. J. Giessibl, *Applied Physics Letters*, 2016, **109**, 141603.

[105] M. Hirata, T. Gotou, S. Horiuchi, M. Fujiwara and M. Ohba, *Carbon*, 2004, **42**, 2929–2937.

[106] S. Katano, T. Wei, T. Sasajima, R. Kasama and Y. Uehara, *Physical Chemistry Chemical Physics*, 2018, **20**, 17977–17982.

[107] D. Berman, A. Erdemir, A. V. Zinovev and A. V. Sumant, *Diamond and Related Materials*, 2015, **54**, 91–96.

[108] S. Wang, Y. Zhang, N. Abidi and L. Cabrales, *Langmuir*, 2009, **25**, 11078–11081.

[109] J. W. Suk, R. D. Piner, J. An and R. S. Ruoff, *ACS Nano*, 2010, **4**, 6557–6564.

[110] F. J. Giessibl, F. Pielmeier, T. Eguchi, T. An and Y. Hasegawa, *Physical Review B*, 2011, **84**, 125409.

[111] J. Stirling and G. A. Shaw, *Beilstein Journal of Nanotechnology*, 2013, **4**, 10–19.

[112] J. Melcher, J. Stirling and G. A. Shaw, *Beilstein Journal of Nanotechnology*, 2015, **6**, 1733–1742.

[113] S. Rast, C. Wattinger, U. Gysin and E. Meyer, *Review of Scientific Instruments*, 2000, **71**, 2772–2775.

[114] T. R. Rodriguez and R. Garcia, *Applied Physics Letters*, 2002, **80**, 1646–1648.

[115] J. Melcher, S. Hu and A. Raman, *Applied Physics Letters*, 2007, **91**, 053101.

[116] F. J. Giessibl, *U.S. patent*, 2013.

[117] H. Schönherr and G. J. Vancso, *Macromolecules*, 1997, **30**, 6391–6394.

[118] Y. Ryousho, S. Sasaki, T. Nagamura, A. Takahara and T. Kajiyama, *Macromolecules*, 2004, **37**, 5115–5117.

[119] K. Kimura, K. Kobayashi, H. Yamada and K. Matsushige, *Langmuir*, 2007, **23**, 4740–4745.

[120] L. Huang and C. Su, *Ultramicroscopy*, 2004, **100**, 277–285.

[121] K. Koga and H. Ohigashi, *Journal of Applied Physics*, 1986, **59**, 2142–2150.

[122] H. Ohigashi, S. Akama and K. Koga, *Japanese Journal of Applied Physics*, 1988, **27**, 2144.

[123] K. Kimura, K. Kobayashi, H. Yamada, T. Horiuchi, K. Ishida and K. Matsushige, *Applied Surface Science*, 2006, **252**, 5489–5494.

[124] E. Momosaki, Proceedings of International Frequency Control Symposium, 1997, pp. 552–565.

[125] F. J. Giessibl, *Review of Scientific Instruments*, 2019, **90**, 011101.

[126] G. Luengo, F.-J. Schmitt, R. Hill and J. Israelachvili, *Macromolecules*, 1997, **30**, 2482–2494.

[127] P. M. McGuiggan, J. Zhang and S. M. Hsu, *Tribology Letters*, 2001, **10**, 217–223.

[128] C.-W. Yang, K. Miyazawa, T. Fukuma, K. Miyata and I.-S. Hwang, *Physical Chemistry Chemical Physics*, 2018, **20**, 23522–23527.

[129] T. Sumomogi, K. Hieda, T. Endo and K. Kuwahara, *Applied Physics A: Materials Science & Processing*, 1998, **66**, S299–S303.

[130] G. Sun, M. Kappl and H.-J. Butt, *Colloids and Surfaces A: Physicochemical and Engineering Aspects*, 2004, **250**, 203–209.

[131] B. V. Derjaguin, U. B. Bazaron, K. T. Zandanova and O. R. Budaev, *Progress in Surface Science*, 1992, **40**, 455–461.

[132] B. V. Derjaguin, U. B. Bazaron, K. D. Lamazhapova and B. D. Tsidypov, *Progress in Surface Science*, 1992, **40**, 462–465.

[133] A. Labuda, K. Kobayashi, K. Suzuki, H. Yamada and P. Grütter, *Physical Review Letters*, 2013, **110**, 066102.

[134] K. Umeda, K. Kobayashi, T. Minato and H. Yamada, *Physical Review Letters*, 2019, **122**, 116001.

[135] C. D. F. Honig and W. A. Ducker, *The Journal of Physical Chemistry C*, 2008, **112**, 17324–17330.

[136] M. Nishio, M. Hirota and Y. Umezawa, *The CH/π interaction*, Wiley-VCH, Inc., New York, 1998.

[137] S. Gupta, D. C. Koopman, G. B. Westermann-Clark and I. A. Bitsanis, *The Journal of Chemical Physics*, 1994, **100**, 8444–8453.

[138] I. Shimoyama, Y. Baba and N. Hirao, *Applied Surface Science*, 2017, **405**, 255–266.

[139] A. Beigbeder, M. Linares, M. Devalckenaere, P. Degée, M. Claes, D. Beljonne, R. Lazzaroni and P. Dubois, *Advanced Materials*, 2008, **20**, 1003–1007.

[140] D. L. Klein and P. L. McEuen, *Applied Physics Letters*, 1995, **66**, 2478–2480.

[141] L. P. Van, V. Kyrylyuk, J. Polesel-Maris, F. Thoyer, C. Lubin and J. Cousty, *Langmuir*, 2009, **25**, 639–642.

[142] K. Voïtchovsky, J. J. Kuna, S. A. Contera, E. Tosatti and F. Stellacci, *Nature Nanotechnology*, 2010, **5**, 401–405.

List of Pubrication

1. Yuya Yamada, Takashi Ichii, Toru Utsunomiya, Hiroyuki Sugimura, "Simultaneous detection of vertical and lateral forces by bimodal AFM utilizing a quartz tuning fork sensor with a long tip", *Japanese Journal of Applied Physics*, **58**, 095003 (2019)

2. Takashi Ichii, Satoshi Ichikawa, Yuya Yamada, Makoto Murata, Toru Utsunomiya, Hiroyuki Sugimura, "Solvation structure on water-in-salt/mica interfaces and its molality dependence investigated by atomic force microscopy", *Japanese Journal of Applied Physics*, **59**, SN1003 (2020)

3. Yuya Yamada, Takashi Ichii, Toru Utsunomiya, Hiroyuki Sugimura, "Visualizing of polymeric liquid/solid interfaces by atomic force microscopy utilizing a quartz tuning fork sensor", *Japanese Journal of Applied Physics*, **59**, SN1009 (2020)

4. Yuya Yamada, Takashi Ichii, Toru Utsunomiya, Kuniko Kimura, Kei Kobayashi, Hirofumi Yamada, Hiroyuki Sugimura, "Fundamental and higher eigenmodes of qPlus sensor with a long probe for vertical-lateral bimodal atomic force microscopy", *Nanoscale Advances*, *In Press* (2023)

5. Yuya Yamada, Takashi Ichii, Toru Utsunomiya, Hiroyuki Sugimura, "Poly(dimethyl siloxane) melt on mica and graphite surfaces investigated by bimodal atomic force microscopy utilizing qPlus sensors", *To be submitted*

List of Presentation

1. Yuya Yamada, Takashi Ichii, Toru Utsunomiya, Hiroyuki Sugimura, "Simultaneous detection of vertical and lateral forces by bimodal AFM utilizing qPlus sensor with a long tip", International Conference on Noncontact Atomic Force Microscopy (NCAFM22), July 2019 (Poster)

2. Yuya Yamada, Takashi Ichii, Toru Utsunomiya, Hiroyuki Sugimura, "Atomic resolution imaging in polymeric liquid by qPlus AFM", The 27th International Colloquium on Scanning Probe Microscopy (ICSPM27), Dec 2019 (Oral)

3. Yuya Yamada, Takashi Ichii, Toru Utsunomiya, Hiroyuki Sugimura, "Structure and viscosity of polymeric liquids at the interfaces with solids investigated by bimodal qPlus AFM", The 28th International Colloquium on Scanning Probe Microscopy (ICSPM28), Dec 2020 (Oral)

4. Yuya Yamada, Takashi Ichii, Toru Utsunomiya, Kuniko Kimura, Kei Kobayashi, Hirofumi Yamada, Hiroyuki Sugimura, "Lateral force microscopy utilizing bimodal qPlus AFM with a long probe", The 9th International Symposium on Surface Science (ISSS-9), Nov. 2021 (Poster)

5. Yuya Yamada, Takashi Ichii, Toru Utsunomiya, Kuniko Kimura, Kei Kobayashi, Hirofumi Yamada, Hiroyuki Sugimura, "Dynamic lateral force detection by bimodal AFM utilizing a qPlus sensor with a long probe", The 29th International Colloquium on Scanning Probe Microscopy (ICSPM29), Dec. 2021 (Oral)

6. Yuya Yamada, Takashi Ichii, Toru Utsunomiya, Hiroyuki Sugimura, "A polymer melt on mica and graphite investigated by bimodal AFM with a long probe qPlus sensor", The 22nd International Vacuum Congress (IVC22), Sep. 2022 (Oral)

Acknowledgements

The author would like to express his gratitude to Professor Hiroyuki Sugimura, Department of Materials Science and Engineering, Kyoto University, for his continuous encouragement, patient guidance, and valuable suggestions to accomplish this study.

The author deeply acknowledges Professor Kuniaki Murase, Department of Materials Science and Engineering, Kyoto University, and Professor Tomoko Hirayama, Department of Mechanical Engineering and Science, Kyoto University, for their valuable comments and suggestions, and critical reading of the manuscript.

The author would like to appreciate Associate Professor Takashi Ichii, Department of Materials Science and Engineering, Kyoto University, for his continuous guidance, encouragement, and fruitful discussion throughout this work.

The author would like to thank Assistant Professor Toru Utsunomiya, Department of Materials Science and Engineering, Kyoto University, for their helpful suggestions, valuable support, and encouragement in accomplishing this work.

The author also would like to acknowledge Emeritus Professor Hirofumi Yamada and Associate Professor Kei Kobayashi, Department of Electronic Science and Engineering, Kyoto University, for their valuable comments and suggestions in accomplishing this work.

The author would like to thank Dr. Kuniko Kimura, Department of Electronic Science and Engineering, Kyoto University, for her help in the preparation of the P(VDF-TrFE) thin films and for her valuable comments.

The author would like to appreciate Daikin Industries Ltd. for providing P(VDF-

TrFE).

The author would like to give his special thanks to the Ph.D. graduate students, Mr. Wataru Kubota and Mr. Bao Yifan, Department of Materials Science and Engineering, Kyoto University, for their friendly and valuable assistance throughout this work.

The author would like to thank Mr. Makoto Murata, a Master's degree graduate of Sugimura Laboratory, Department of Materials Science and Engineering, Kyoto University, for his help and valuable advice in the early stage of this study.

The author is much grateful to all the members of Sugimura Laboratory, Department of Materials Science and Engineering, Kyoto University, for their continuous help in both the experiment and the life.

The financial support of the Hoshizaki Shinsei Foundation and Japan Society for the Promotion of Science is greatly acknowledged.

Finally, the author would like to express his special thanks to his wife and parents for their continuous encouragement and support in accomplishing this work.